Bulletin of Romanian Chemical Engineering Society

2 2017

ISSN 2360-4697
Edited by SICR and Matrix Rom

The journal is included in the international database
INDEX COPERNICUS INTERNATIONAL

ISSN 2360-4697

Bulletin of Romanian Chemical Engineering Society

Volume 4 2017 Number 2

Contents

PHASE BEHAVIOR PREDICTIONS FOR CARBON DIOXIDE + ISOPROPANOL BINARY SYSTEM WITH A CUBIC EQUATION OF STATE

Radu C. RACOVIŢĂ[1], Sergiu SIMA[1], Catinca SECUIANU[1,2,*] Viorel FEROIU[1]

[1] Department of Inorganic Chemistry, Physical Chemistry & Electrochemistry, Faculty of Applied Chemistry and Materials Science, University Politehnica of Bucharest, 1-7 Gh. Polizu Street, 011061, Bucharest, Romania
[2] Honorary Research Fellow, Department of Chemical Engineering, Imperial College London, London, United Kingdom

Abstract

*The purpose of this paper is to demonstrate the ability of a cubic equation model to predict the phase behavior of the carbon dioxide (1) + isopropanol (2) binary system. The model selected is the cubic **G**eneral **E**quation **o**f **S**tate – GEOS, coupled with classical van der Waals mixing rules – two-parameter conventional mixing rule, 2PCMR. One unique set of binary interaction parameters is used to predict the phase behavior of the system.*

Key words: Carbon dioxide, isopropanol, high pressures, VLE, GEOS, predictions

1. Introduction

The carbon (as carbon dioxide, CO_2) emissions produced by fossil fuel-powered plants and energy production facilities account for over 80% of greenhouse gases (GHGs) [1]. Among the many options for carbon mitigation, carbon capture and storage (CCS) is an almost essential part and could contribute approximately 20% to CO_2 emission reductions by 2050, as recommended by International Energy Agency (IEA) [1]. CCS holds great potential in industry and petroleum refineries given their large CO_2 emissions. In addition, there are many industrial processes that generate rich CO_2 gas streams, or in some cases pure CO_2, which could reduce the costs of CCS.

At the same time, carbon dioxide is a non-hazardous and safe substance used as working fluid for many green products and processes due to its compatibility with the environment. In particular, the physical properties and

* Corresponding author; Email address: catinca.secuianu@upb.ro; c.secuianu@imperial.ac.uk

phase behavior of complex mixtures containing CO_2 are nowadays associated with a wide range of applications [2-4].

Recently [5,6], we started to investigate experimentally the effect of the functional group of different classes of substances on the ability to dissolve carbon dioxide. We are equally interested in the capability of models to predict the phase behavior of these systems at high pressures.

Among the mixtures of interest, carbon dioxide + alcohol mixtures at high pressures are of particular importance in the design, simulation, and optimization of extraction processes, where alcohols are commonly used as co-solvents [7].

In this study, we focus on the carbon dioxide (1) + isopropanol (2) binary system. In a previous paper [6], we compared the prediction results by two well-known cubic equations of state (EoS), namely Soave-Redlich-Kwong (SRK) and Peng-Robinson (PR), coupled with classical van der Waals mixing rules (2PCMR). A single set of binary interaction parameters for each EoS, determined for the carbon dioxide + 2-butanol binary system, was used to model the global phase behavior of the system.

Here, the global phase behavior of the system was modeled with a general cubic equation of state (GEOS) [8,9] coupled with classical van der Waals mixing rules (2PCMR). This cubic equation is a generalized form with four parameters for all cubic equations of state with two, three, and four parameters. One unique set of binary interaction parameters determined for the carbon dioxide + 1-propanol system was used to calculate the critical curves and vapor-liquid equilibrium diagrams.

2. Modeling

The modeling of phase behavior of this system was made with the GEOS equation [8,9] coupled with classical van der Waals mixing rules (2PCMR). The GEOS [8,9] equation of state is:

$$P = \frac{RT}{V-b} - \frac{a(T)}{(V-d)^2 + c} \tag{1}$$

with the classical van der Waals mixing rules

$$a = \sum_i \sum_j X_i X_j a_{ij} \qquad b = \sum_i X_i b_i \tag{2}$$

$$c = \sum_i \sum_j X_i X_j c_{ij} \qquad d = \sum_i X_i d_i \tag{3}$$

$$a_{ij} = (a_i a_j)^{1/2}(1-k_{ij}) \qquad b_{ij} = \frac{b_i + b_j}{2}(1-l_{ij}) \qquad c_{ij} = \pm(c_i c_j)^{1/2} \tag{4}$$

with "+" for c_i, $c_j > 0$ and "–" for c_i, $c_j < 0$. Generally, negative values are common for the c parameter of pure components.

The four parameters *a*, *b*, *c*, and *d* for a pure component are expressed by:

$$a(T) = \frac{R^2 T_c^2}{P_c}\beta(T_r)\Omega_a \qquad b = \frac{RT_c}{P_c}\Omega_b \tag{5}$$

$$c = \frac{R^2 T_c^2}{P_c^2}\Omega_c \qquad d = \frac{RT_c}{P_c}\Omega_d \tag{6}$$

Setting four critical conditions, with α_c as the Riedel criterion:

$$P_r = 1 \qquad \left(\frac{\partial P_r}{\partial V_r}\right)_{T_r} = 0 \qquad \left(\frac{\partial^2 P_r}{\partial V_r^2}\right)_{T_r} = 0 \qquad \alpha_c = \left(\frac{\partial P_r}{\partial T_r}\right)_{V_r} \tag{7}$$

at $T_r = 1$ and $V_r = 1$, the expressions of the parameters Ω_a, Ω_b, Ω_c, Ω_d are obtained

$$\Omega_a = (1-B)^3 \qquad \Omega_b = Z_c - B \qquad \Omega_c = (1-B)^2(B-0.25) \tag{8}$$

$$\Omega_d = Z_c - \frac{(1-B)}{2} \qquad B = \frac{1+m}{\alpha_c + m} \tag{9}$$

where P_r, T_r, V_r are the reduced variables and Z_c is the critical compressibility factor.

The temperature function used is:

$$\beta(T_r) = T_r^{-m} \tag{10}$$

The GEOS parameters *m* and α_c were estimated by constraining the EoS to reproduce the experimental vapor pressure and liquid volume on the saturation curve between the triple point and the critical point [10].

The calculations were made using the software package *PHEQ*, developed in our laboratory [11]. The critical curves were calculated using the method proposed by Heidemann and Khalil [12], with numerical derivatives given by Stockfleth and Dohrn [13].

Instead of correlating the experimental data, we used a predictive approach. Thus, the GEOS equation was used in a semi-predictive approach to obtain a set of binary parameters yielding good results in the binary system carbon dioxide + 1-propanol (including VLE in the entire temperature range, critical points, global phase behavior) [14]. The set of binary parameters was calculated using the k_{12}–l_{12} method [15] to obtain the experimental value of the vapor–liquid critical pressure maximum (CPM) simultaneously with the temperature of the upper critical endpoint (UCEP). The binary system carbon dioxide + 1-propanol exhibits a type II phase diagram, according to the classification of van Konynenburg and Scott [16]. The parameter set (k_{12} = 0.042; l_{12} = -0.021) obtained for the mixture containing the position isomer was then used to model the carbon dioxide (1) + isopropanol (2) system. To our knowledge, there is no experimental evidence to support the classification into a type of phase diagram,

but it seems that the carbon dioxide + isopropanol (2-propanol) system exhibits type I or type II phase behavior, according to the classification of van Konynenburg and Scott [16] or the more recent one of Privat and Jaubert [17].

The GEOS parameters, critical data, the acentric factors of the pure substances used in the calculations are presented in Table 1 [18].

Table 1.

Critical data, acentric factor [18], and GEOS parameters for pure compounds

Compound	T_c/K	P_c/bar	V_c/cm^3·mol^{-1}	Ω	α_c	M
carbon dioxide	304.21	73.83	93.90	0.2236	7.0517	0.3146
2-propanol (isopropanol)	508.30	47.64	220.0	0.6669	9.3838	0.6695

3. Results and discussions

In Fig. 1, the critical phase behavior of the carbon dioxide + isopropanol system by GEOS/2PCMR is presented. All available critical data in the literature are compared with GEOS predictions. As can be seen, the model predicts type I phase behavior, meaning that there is only vapor-liquid continuous critical curve stretching between the critical points of the pure components.

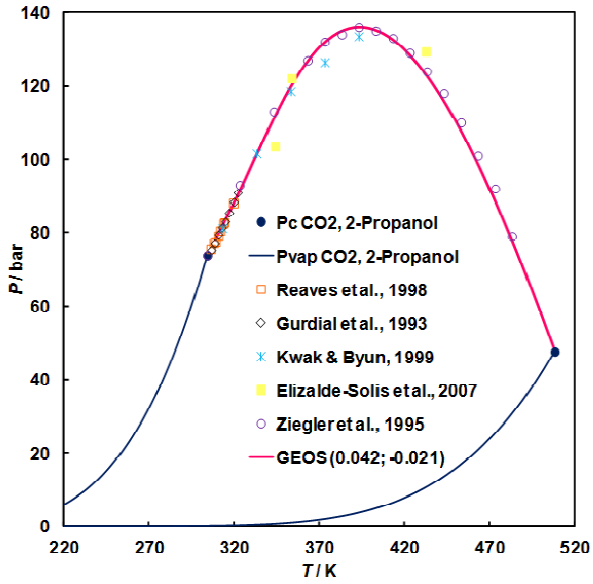

Fig. 1. *P–T* fluid phase diagram for carbon dioxide (1) + isopropanol (2) system: symbols, literature data [19-23]; thick line, predictions by GEOS.

Although the parameters were obtained for mixture with the position isomer, namely the carbon dioxide + 1-propanol binary system, it can be noticed that the critical curve is remarkably well predicted. In Fig. 2, the critical pressures and temperatures are plotted against carbon dioxide compositions. GEOS predictions are in good agreement with the available experimental data.

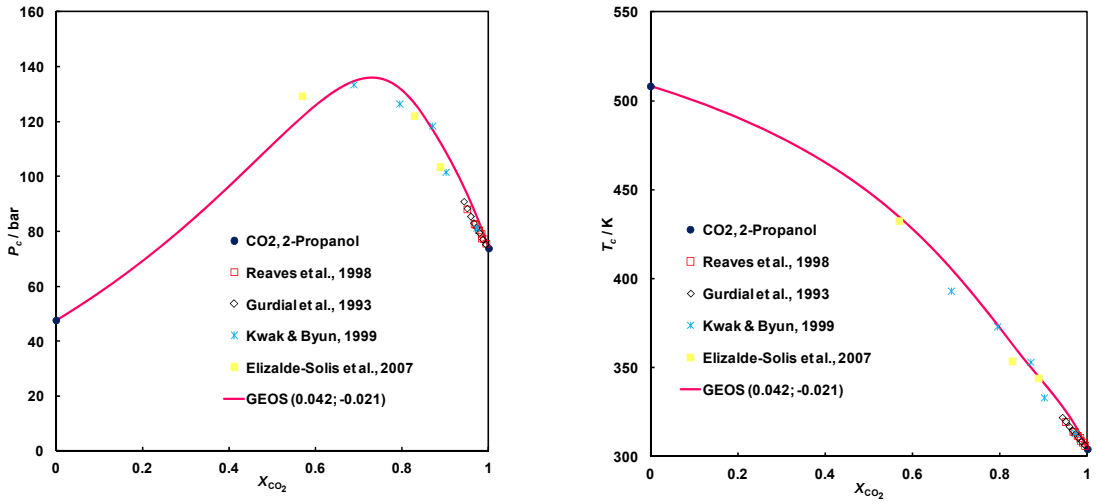

Fig. 2. *P*–*x* and *T*–*x* projections of the phase diagram for carbon dioxide (1) + isopropanol (2) system: symbols, literature data [19-22]; lines, predictions by GEOS.

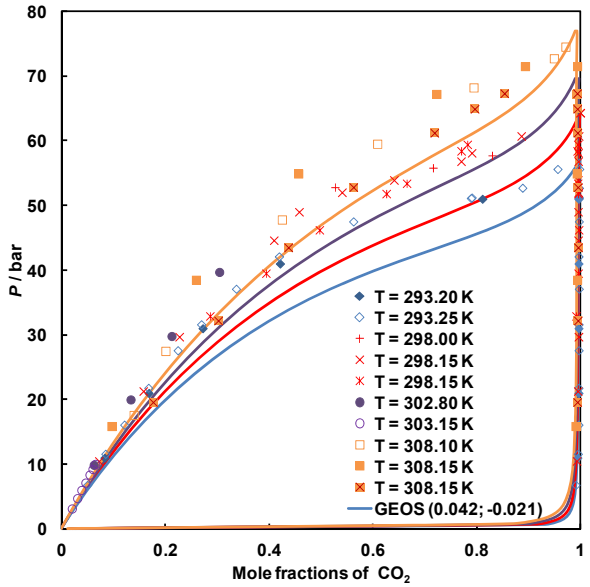

Fig. 3. Comparison of literature VLE data [24,27-31,24] and predictions by GEOS for carbon dioxide (1) + isopropanol (2) system.

The set of binary interaction parameters was also used to predict all available vapor-liquid equilibrium (VLE) data in a wide range of temperatures and pressures. The literature experimental data and GEOS predictions are compared in Figs. 3-10.

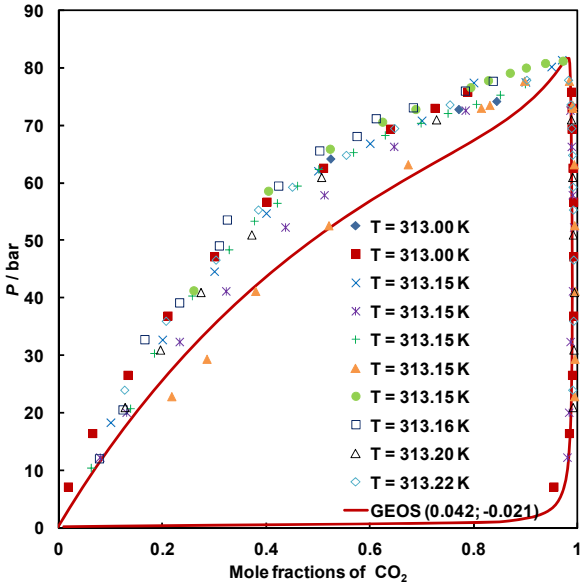

Fig. 4. Comparison of literature VLE data [36,26,30,33,31,21,35,39,35,25,38,32] and predictions by GEOS for carbon dioxide (1) + isopropanol (2) system.

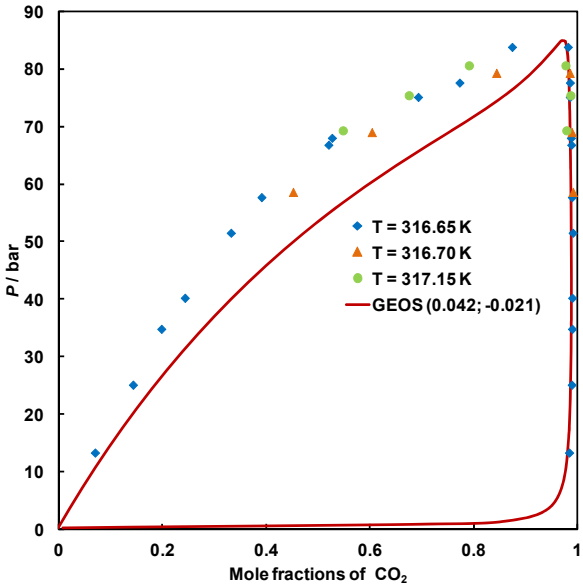

Fig. 5. Comparison of literature VLE data [24,40-41] and predictions by GEOS for carbon dioxide (1) + isopropanol (2) system.

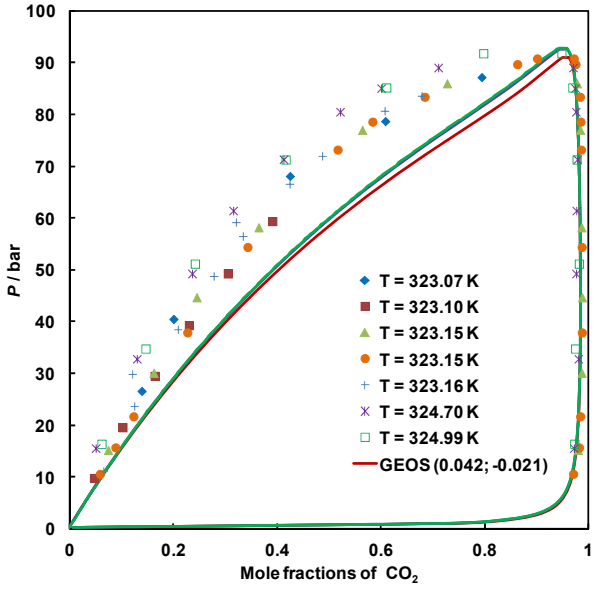

Fig. 6. Comparison of literature VLE data [30,28,24,37,35,34,34] and predictions by GEOS for carbon dioxide (1) + isopropanol (2) system.

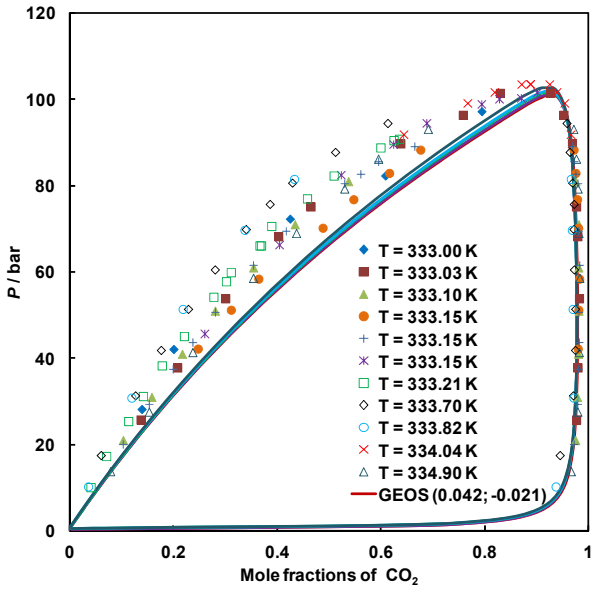

Fig. 7. Comparison of literature VLE data [30,38,21,37,27,35,25,35,32,34,34,22,40] and predictions by GEOS for carbon dioxide (1) + isopropanol (2) system.

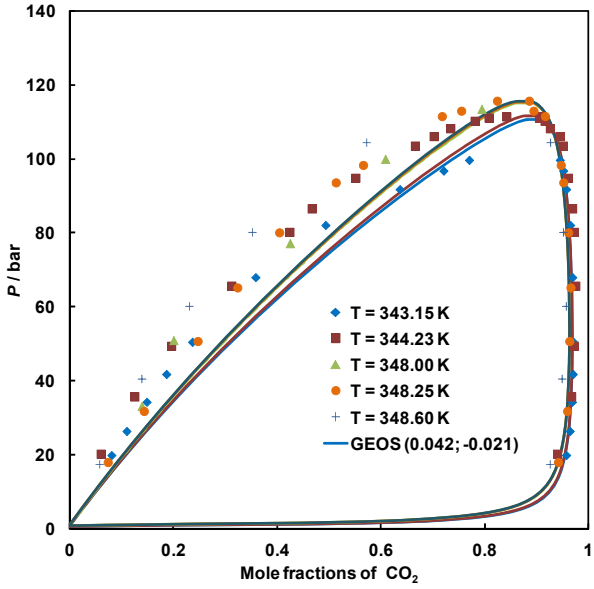

Fig. 8. Comparison of literature VLE data [37,22,30,38,34] and predictions by GEOS for carbon dioxide (1) + isopropanol (2) system.

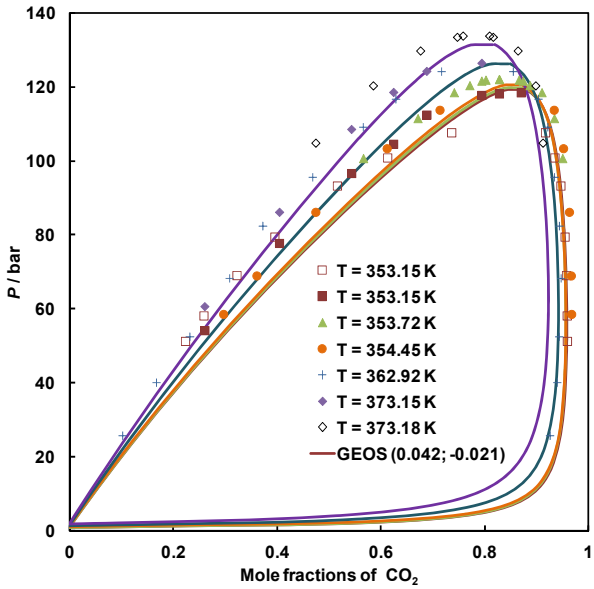

Fig. 9. Comparison of literature VLE data [21,37,22,40,38,21,22] and predictions by GEOS for carbon dioxide (1) + isopropanol (2) system.

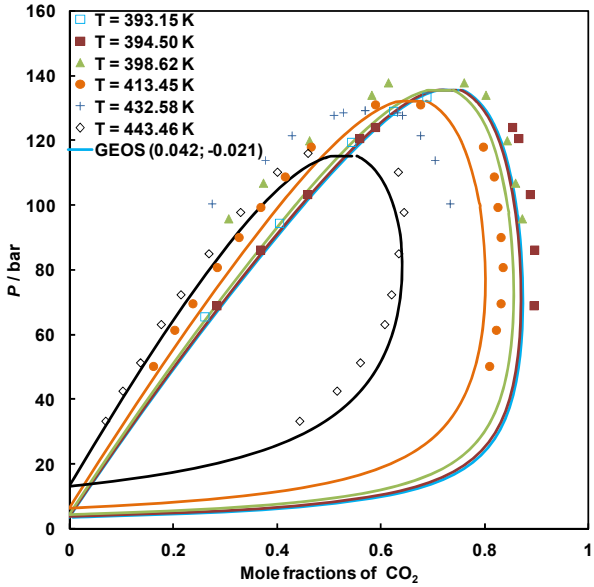

Fig. 10. Comparison of literature VLE data [21,40,22,22,22,22] and predictions by GEOS for carbon dioxide (1) + isopropanol (2) system.

Although more than 500 equilibrium experimental points were collected for the carbon dioxide + isopropanol system in the PHEQ database, it can be easily noticed that there is a high degree of scatter among them. Figs. 4, 6, and 7 are very good examples of scattered experimental data, as several data sets are available at these temperatures (313.15, 323.15, and 333.15 K), from different research groups all over the world.

In all figures it can be observed that GEOS predictions are reasonably good. As expected, the critical points are very well predicted at each temperature. The general trend is that the liquid curve is underestimated, but as temperature increases, the predictions improve. The vapor phase is very well predicted over the entire range, except at very high temperatures (Fig. 10).

6. Conclusions

The cubic GEOS was used to predict the phase behavior of the carbon dioxide + isopropanol system. One unique set of binary interaction parameters obtained using the k_{12}–l_{12} method for the carbon dioxide + 1-propanol system was applied to model the carbon dioxide + isopropanol mixture in a wide range of temperatures and pressures. The predicted results were compared with the available literature data for carbon dioxide + isopropanol binary system. The topology of phase behavior is very well predicted, taking into account the relatively simple model and the modeling procedure used.

Acknowledgements
„This work was supported by a grant of Ministry of Research and Innovation, CNCS - UEFISCDI, project number PN-III-P4-ID-PCE-2016-0629, within PNCDI III".

Dr. Sima acknowledges the partial financial support of the Romanian Chemical Engineering Society for presenting this work at the 20th Romanian International Conference on Chemistry and Chemical Engineering – RICCCE 20, September 6-9, 2017, Poiana Brasov, Romania.

REFERENCES

[1] Wu, X., Yu, Y.S., Qin, Z., Zhang, Z.X., The Advances of Post-Combustion CO_2 Capture with Chemical Solvents: Review and Guidelines, *Energy Procedia*, 63, (2014), 1339–1346.
[2] Zhao, Q., Mecheri, M., Neveux, T., Privat, R., Jaubert, J.-N., Selection of a Proper Equation of State for the Modeling of a Supercritical CO_2 Brayton Cycle: Consequences on the Process Design, *Industrial & Engineering Chemistry Research,* 56, (2017), 6841–6853.
[3] Fonseca, J.M.S., Liborio, B., Dohrn, R., Wolf, A., Phase equilibria in process design for the production of polymers derived from carbon dioxide, *Fluid Phase Equilibria*, 409, (2016), 369–376.
[4] Hendriks, E., Kontogeorgis, G.M., Dohrn, R., de Hemptinne, J.C., Economou, I.G., Zilnik, L.F., Vesovic, V., Industrial Requirements for Thermodynamics and Transport Properties, *Industrial & Engineering Chemistry Research*, 49, (2010), 11131–11141.
[5] Sima, S., Secuianu, C., Feroiu, V., Phase equilibria of CO_2 + 1,2-dimethoxyethane at high-pressures, *Fluid Phase Equilibria*, 458, (2018), 47–57.
[6] Sima, S., Racovita, R.C., Dinca, C., Secuianu, C., Feroiu, V., Phase equilibrium calculations for carbon dioxide + 2-propanol system, *University Politehnica of Bucharest Scientific Bulletin Series B: Chemistry & Materials Science*, (2017), (accepted manuscript)
[7] Gauter, K., Peters, C.J., Scheidgen, A.L., Schneider, G.M., Cosolvency effects, miscibility windows and two-phase lg holes in three-phase llg surfaces in ternary systems: a status report, *Fluid Phase Equilibria*, 171, (2000), 127–149.
[8] Geană, D., A new equation of state for fluids. I. Applications to PVT calculations for pure fluids, *Revista de Chimie*, 37, (1986), 303–309.
[9] Geană, D., A new equation of state for fluids. II. Applications to phase equilibria, *Revista de Chimie,* 37, (1986), 951–959.
[10] Geană, D., Feroiu, V., Thermodynamic properties of pure fluids using the GEOS3C equation of state, *Fluid Phase Equilibria*, 174, (2000), 51–68.
[11] Geană, D., Rus, L., Phase equilibria database and calculation program for pure components systems and mixtures, *Proc. Romanian Int. Conf. Chem. Chem. Eng.* (RICCCE XIV), Bucharest, Romania, 2*,* (2005), 170–178.
[12] Heidemann, R.A., Khalil, A.M., The calculation of critical points, *AIChE Journal,* 26, (1980), 769–779.
[13] Stockfleth, R., Dohrn, R., An algorithm for calculating critical points in multicomponent mixtures which can easily be implemented in existing programs to calculate phase equilibria, *Fluid Phase Equilibria,* 145, (1998), 43–52.
[14] Secuianu, C., Feroiu, V., Geană, D., High-Pressure Phase Equilibria for the Carbon Dioxide+1-Propanol System, *Journal of Chemical & Engineering Data,* 53, (2008), 2444–2448.

[15] Polishuk, I., Wisniak, J., Segura, H., Simultaneous prediction of the critical and sub-critical phase behavior in mixtures using equation of state I. Carbon dioxide-alkanols, *Chemical Engineering Science,* 56, (2001), 6485–6510.
[16] van Konynenburg, P.H, Scott, R.L., Critical lines and phase equilibria in binary van der Waals mixtures, *Philosophical Transactions of the Royal Society London, Series A*, 298, (1980), 495–540.
[17] Privat, R.; Jaubert, J.N., Classification of global fluid-phase equilibrium behaviors in binary systems, *Chemical Engineering Research Design*, 91, 1807–1839, 2013.
[18] Evaluated Standard Thermophysical Property Values, DIPPR Project 801 full version, Brigham Young University, Provo Utah, 2005.
[19] Reaves, J.T., Griffith, A.T., Roberts, C.B., Critical properties of dilute carbon dioxide + entrainer and ethane + entrainer mixture, *Journal of Chemical & Engineering Data*, 43 (4), (1998), 683–686.
[20] Gurdial, G.S., Foster, N.R., Yun, S.L.J., Tilly, K.D., Phase behavior of supercritical fluid – entrainer systems, in Supercritical fluid engineering science: fundamentals and applications, *ACS Symposium Series*, 514, (1993), 34–45.
[21] Kwak, C., Byun, H.S., Carbon dioxide – isopropyl alcohol system: high pressure phase behavior and application with SAFT equation of state, *Kongop Hwahak*, 10 (2), (1999), 324–329.
[22] Elizalde-Solis, O., Galicia-Luna, L.A., Camacho-Camacho, L.E., High-pressure vapor-liquid equilibria for CO2 + alkanol systems and densities of n-dodecane and n-tridecane, *Fluid Phase Equilibria*, 259 (1), (2007), 23–32.
[23] Ziegler, J.W., Chester, T.L., Innis, D.P., Page, S.H., Dorsey, J.G., Chapter 6: Supercritical Fluid Flow Injection Method for Mapping Liquid-Vapor Critical Loci of Binary Mixtures Containing CO_2 in Innovations in Supercritical Fluids. Science and technology, *ACS Symposium Series*, 608, (1995), 93–110.
[24] Secuianu, C., Feroiu, V., Geană, D., High-Pressure Vapor-Liquid Equilibria in the System Carbon Dioxide and 2-Propanol at Temperatures from 293.25 K to 323.15 K, *Journal of Chemical & Engineering Data*, 48, (2003), 1384–1386.
[25] Bamberger, A., Maurer, G., High-pressure (vapor + liquid) equilibria in (carbon dioxide + acetone or 2-propanol) at temperatures from 293 K to 333 K, *Journal of Chemical Thermodynamics*, 32, (2000), 685–700.
[26] Zevnik, L., Levec, J., Hydrogen solubility in CO2-expanded 2-propanol and in propane-expanded 2-propanol determined by an acoustic sensor, *Journal of Supercritical Fluids*, 41 (3), (2007), 335–342.
[27] Luo, Z., Wei, Y., Hu, Y., Phase Equilibria Study for Isopropanol Extraction from Aqueous Solution by Using Supercritical Carbon Dioxide, *Huagong Xuebao*, 41 (4), (1990), 395–402.
[28] Nourozieh, H., Kariznovi, M., Abedi, J., Experimental and modeling investigations of solubility and saturated liquid densities and viscosities for binary systems methane +, ethane +, and carbon dioxide + 2-propanol, *Journal of Chemical Thermodynamics*, 65, (2013), 191–197.
[29] Li, T.Z., Tang, Z.G., Hu, H., Guo, D., Measurement of the Solubility for CO2 in Alcohols and its Correlation with the Molecular Connectivity Index, *Gaoxiao Huaxue Gongcheng Xuebao*, 26 (1), (2012), 1–6.
[30] Khalil, W., Coquelet, C., Richon, D., High-Pressure Vapor-Liquid Equilibria, Liquid Densities, and Excess Molar Volumes for the Carbon Dioxide + 2-Propanol System from 308.10 to 348.00 K, *Journal of Chemical & Engineering Data*, 52 (5), (2007), 2032–2040.

[31] Yao, S., Liu, F., Han, Z., Zhu, Z., Vapor-Liquid Equilibria of Binary Systems of Alcohols, Water - Carbon Dioxide at Supercritical or Near Critical Condition, *Gaoxiao Huaxue Gongcheng Xuebao*, 3 (3), (1989), 9–15.
[32] Suzuki, T., Tsuge, N., Nagahama, K., Solubilities of Ethanol, 1-Propanol, 2-Propanol and 1-Butanol in Supercritical Carbon Dioxide at 313 K and 333 K, *Fluid Phase Equilibria*, 67, (1991), 213–226.
[33] Yaginuma, R., Nakajima, T., Tanaka, H., Kato, M., Densities of carbon dioxide + 2-propanol at 313.15 K and pressures to 9.8 MPa, *Journal of Chemical & Engineering Data*, 42 (4), (1997), 814–816.
[34] Galicia-Luna, L.A., Ortega-Rodriguez, A., Richon, D., New Apparatus for the Fast Determination of High-Pressure Vapor-Liquid Equilibria of Mixtures and of Accurate Critical Pressures, *Journal of Chemical & Engineering Data,* 45 (2), (2000), 265–271.
[35] Stratmann, A., In-situ Raman-spectroscopy of evaporation equilibria. Measurement of two component systems under elevated pressure and elevated temperature, Ph.D. Thesis 2 Ruhr University Bochum, Germany, 2003.
[36] Lazzaroni, M.J., Bush, D., Brown, J.S., Eckert, C.A., High-Pressure Vapor-Liquid Equilibria of Some Carbon Dioxide + Organic Binary Systems, *Journal of Chemical & Engineering Data,* 50 (1), (2005), 60–65.
[37] Lim, J.S., Jung, Y.G., Yoo, K.P., High-Pressure Vapor-Liquid Equilibria for the Binary Mixtures of Carbon Dioxide + Isopropanol (IPA, *Journal of Chemical & Engineering Data,* 52 (6), (2007), 2405–2408.
[38] Galicia-Luna, L.A., Elizalde-Solis, O., New analytic apparatus for experimental determination of vapor-liquid equilibria and saturation densities, *Fluid Phase Equilibria*, 296 (1), (2010), 46–52.
[39] Aida, T., Aizawa, T., Kanakubo, M., Nanjo, H., Relation between Volume Expansion and Hydrogen Bond Networks for CO2−Alcohol Mixtures at 40 °C, *Journal of Physical Chemistry B*, 114 (43), (2010), 13628–13636.
[40] Radosz, M., Vapor-liquid equilibrium for 2-propanol and carbon dioxide, *Journal of Chemical & Engineering Data,* 31 (1), (1986), 43–45.
[41] Secuianu, C., Feroiu, V., Geană, D., High-Pressure Phase Equilibria for the Carbon Dioxide + Methanol and Carbon Dioxide + Isopropanol Systems, *Revista de Chimie*, 54 (11), (2003), 874–879.

MLR MODELS USED TO PREDICT EXCESS THERMODYNAMIC PROPERTIES

Cătălin LISA[1]

Department of Chemical Engineering, Faculty of Chemical Engineering and Environmental Protection, "Gheorghe Asachi" Technical University of Iasi, 73 Prof. dr. docent Dimitrie Mangeron Street, Iasi, 700050, Romania

Abstract

This paper describes the determination of the refractive index (n) and of the density (ρ) of the following two ternary systems: water-methyl ethyl ketone-isopropyl alcohol and water-methyl ethyl ketone-acetone, in a composition range specific to diluted solutions, at various temperatures and atmospheric pressure. Based on these experimental data, it was calculated the excess refractive indices and the excess molar volumes, and it was established the type of deviation from ideal behavior. The refractive index may be experimentally determined rather easily, with good measuring accuracy and low substance consumption. The development of theoretical or empirical correlations between this parameter and other properties that are more difficult to measure, like density, is of interest for researchers. Therefore, in this paper it was employed the multiple linear regression (MLR) method to predict the excess molar volumes and implicitly the density of ternary mixtures, based on experimental determinations of the refraction index.

Key words: Density, Refractive index, Excess molar volumes, MLR model

1. Introduction

Methyl ethyl ketone, acetone, isopropyl alcohol are solvents commonly used in chemical industry, and, when released in the atmosphere, their emissions may be extremely dangerous for human health [1, 2]. Methyl ethyl ketone may cause digestive tract irritations, and the ingestion of considerable amounts may cause headache, nausea, vomiting, dizziness, and it may also have a narcotic effect. Acetone and isopropyl alcohol have adverse effects on the liver, kidney and respiratory system. In practice, the removal of these volatile organic compounds (VOCs) is achieved by means of scrubbers, which, by absorption in water, lead to the release of minimal amounts of pollutants in the atmosphere. The design of efficient facilities or the improvement of the performance of existing

[1] Corresponding author: Email address: clisa@ch.tuiasi.ro

ones require the development of databases of properties for the pollutant and water mixtures. There are in literature studies on the density and refractive index only for a series of binary systems [3-6] containing one or two components of the ones tackled in this research; nevertheless, many of them are quite old [7, 8] and were carried out using equipment the accuracy of which was rather poor as compared to the accuracy of the devices that are currently used to measure density and refractive index.

In this paper it was report the findings of the experiments conducted to determine the refractive index and the density of the following ternary mixtures: water-methyl ethyl ketone-isopropyl alcohol and water-methyl ethyl ketone-acetone, at very small pollutant concentrations in water and temperatures of 293.15, 300.15, and 307.15 K. The excess refractive index n_{exc} and excess molar volumes were also determined, the findings indicating the type of deviation from the ideal value of these ternary systems. Considering that the refractive index may be determined by experiments rather easily, with quite good measuring accuracy and low substance consumption, by means of the multiple linear regression (MLR) method, it was were able to predict the excess molar volumes and implicitly the density of the ternary mixtures based on the experimental determinations of the refractive index.

2. Experimental

The purity of the fluids involved in the experiments, methyl ethyl ketone, isopropyl alcohol and acetone, was p.a., and the solutions were prepared by weighing, which enabled us to estimate molar fractions with ±0.0001 accuracy.
The experimental determination of the refractive index was done using a Kruss refractometer (digital Abbe refractometer) with wavelength corresponding to Na (589.3 nm) and a Lauda E100 thermostat for maintaining a constant temperature with 0.1 °C accuracy. The equipment was calibrated using bidistilled water. This type of refractometer has a standard uncertainty of reading the refractive index of ±0.0002 [9].

An Anton Paar type DMA 4500 densitometer was used to measure the density of the ternary fluid mixtures prepared by my. Equipment calibration was checked using air (ρ=0.001085 g/cm^3, at 20°C temperature) and bidistilled water (ρ=0.998203 g/cm^3, at 20°C temperature). The density of the ternary mixtures was measured with a standard uncertainty of ±0.001 g/cm^3 [9].

Thermodynamic excess properties were modelled by means of statistical experimental data processing based on the multiple linear regression (MLR) method. Sigmaplot 11.0 is the software used for experimental data processing.

3. Results and discussions

Tables 1 and 2 show the values of the refractive index and of the density, determined by means of experiments on pure fluids, whereas tables 3, 4, 5 and 6 show the same values, but for ternary mixtures. Both the refractive index values and the density values decrease with temperature increase.

Table 1

Refractive index for pure fluids

Temperature K	Water	Methyl ethyl ketone	Isopropyl alcohol	Acetone
293.15	1.3337	1.3800	1.3780	1.3597
300.15	1.3320	1.3762	1.3744	1.3555
307.15	1.3312	1.3733	1.3719	1.3527

Table 2

Density of pure fluids [g/cm^3]

Temperature K	Water	Methyl ethyl ketone	Isopropyl alcohol	Acetone
293.15	0.9982	0.8080	0.7874	0.7907
300.15	0.9955	0.8005	0.7829	0.7833
307.15	0.9944	0.7796	0.7750	0.7765

Table 3

Refractive index of ternary water (1)-methyl ethyl ketone (2)-isopropyl alcohol (3) mixtures

X_2	X_3	293.15	300.15	307.15
0.0097	0.0099	1.3394	1.3375	1.3372
0.0997	0.0298	1.3451	1.3427	1.3417
0.0099	0.0503	1.3502	1.3473	1.3461
0.0095	0.0689	1.3540	1.3516	1.3505
0.0293	0.0292	1.3506	1.3475	1.3468
0.0293	0.0500	1.3547	1.3518	1.3499
0.0288	0.0667	1.3747	1.3541	1.3528
0.0490	0.0480	1.3575	1.3556	1.3541
0.0496	0.0315	1.3552	1.3525	1.3522
0.0497	0.0684	1.3603	1.3576	1.3563

Table 4

Refractive index of ternary water (1)-methyl ethyl ketone (2)-acetone (3) mixtures

X_2	X_3	293.15	300.15	307.15
0.0101	0.0098	1.3392	1.3371	1.3361
0.0098	0.0294	1.3432	1.3410	1.3386
0.0100	0.0441	1.3446	1.3438	1.3426
0.0097	0.0648	1.3491	1.3473	1.3465
0.0278	0.0350	1.3489	1.3472	1.3458
0.0309	0.0505	1.3523	1.3492	1.3479
0.0296	0.0695	1.3536	1.3519	1.3498
0.0325	0.0497	1.3626	1.3496	1.3483
0.0492	0.0295	1.3646	1.3505	1.3496
0.0495	0.0662	1.3578	1.3542	1.3532

Table 5

Density of ternary water (1)-methyl ethyl ketone (2)-isopropyl alcohol (3) mixtures [g/cm^3]

X_2	X_3	293.15	300.15	307.15
0.0097	0.0099	0.9885	0.9866	0.9841
0.0997	0.0298	0.9802	0.9777	0.9746
0.0099	0.0503	0.9729	0.9696	0.9662
0.0095	0.0689	0.9663	0.9622	0.9580
0.0293	0.0292	0.9735	0.9702	0.9665
0.0293	0.0500	0.9656	0.9618	0.9577
0.0288	0.0667	0.9574	0.9565	0.9516
0.0490	0.0480	0.9582	0.9538	0.9493
0.0496	0.0315	0.9650	0.9607	0.9567
0.0497	0.0684	0.9498	0.9456	0.9404

Table 6.

Density of ternary water (1)-methyl ethyl ketone (2)-acetone (3) mixtures [g/cm^3]

X_2	X_3	293.15	300.15	307.15
0.0101	0.0098	0.9895	0.9873	0.9845
0.0098	0.0294	0.9827	0.9799	0.9767
0.0100	0.0441	0.9776	0.9745	0.9710
0.0097	0.0648	0.9698	0.9676	0.9637
0.0278	0.0350	0.9738	0.9705	0.9568
0.0309	0.0505	0.9679	0.9640	0.9595
0.0296	0.0695	0.9622	0.9579	0.9541
0.0325	0.0497	0.9673	0.9636	0.9590
0.0492	0.0295	0.9679	0.9640	0.9596
0.0495	0.0662	0.9531	0.9511	0.9457

The deviations from ideal behaviour may be accounted for by the quantity variation occurring during the mixing and may be determined by the excess molar volumes (1) and by the notion of excess refractive index (n_{exc}), defined by the

following ratio (2):

$$V_{exc} = X_1 M_1 \left(\frac{1}{\rho} - \frac{1}{\rho_1} \right) + X_2 M_2 \left(\frac{1}{\rho} - \frac{1}{\rho_2} \right) + X_3 M_3 \left(\frac{1}{\rho} - \frac{1}{\rho_3} \right) \quad (1)$$

$$n_{exc} = n - X_1 \cdot n_1 - X_2 \cdot n_2 - X_3 \cdot n_3 \quad (2)$$

where M_i is the molar mass of each solution component, ρ is the density of ternary mixtures, ρ_i is the density of components in pure state, n is the refractive index of ternary solutions, and n_i is the refractive index of pure compounds and X_i the molar fractions.

The values of the excess values calculated for the two ternary systems at 293.15, 300.15 and 307.15 K temperatures are shown in tables 7, 8, 9 and 10.

Table 7

Excess refractive index of ternary water (1)-methyl ethyl ketone (2)-isopropyl alcohol (3) mixtures

X_2	X_3	293.15	300.15	307.15
0.0097	0.0099	0.00481	0.00465	0.00519
0.0997	0.0298	0.00546	0.00503	0.00509
0.0099	0.0503	0.01381	0.01273	0.01244
0.0095	0.0689	0.01681	0.01626	0.01610
0.0293	0.0292	0.01425	0.01297	0.01318
0.0293	0.0500	0.01743	0.01638	0.01543
0.0288	0.0667	0.03671	0.01800	0.01767
0.0490	0.0480	0.01940	0.01940	0.01888
0.0496	0.0315	0.01781	0.01697	0.01763
0.0497	0.0684	0.02127	0.02050	0.02022

Table 8

Excess refractive index of ternary water (1)-methyl ethyl ketone (2)-acetone (3) mixtures

X_2	X_3	293.15	300.15	307.15
0.0101	0.0098	0.00477	0.00442	0.00426
0.0098	0.0294	0.00828	0.00787	0.00636
0.0100	0.0441	0.00929	0.01032	0.01003
0.0097	0.0648	0.01326	0.01335	0.01350
0.0278	0.0350	0.01299	0.01314	0.01268
0.0309	0.0505	0.01585	0.01464	0.01431
0.0296	0.0695	0.01671	0.01695	0.01586
0.0325	0.0497	0.02609	0.01499	0.01466
0.0492	0.0295	0.02784	0.01562	0.01569
0.0495	0.0662	0.02007	0.01844	0.01849

Table 9

Excess molar volumes of ternary water (1)-methyl ethyl ketone (2)-isopropyl alcohol (3) [cm^3/mol]

X_2	X_3	293.15	300.15	307.15
0.0097	0.0099	-0.13809	-0.16160	-0.16358
0.0997	0.0298	-1.72169	-1.79639	-1.99763
0.0099	0.0503	-0.44049	-0.44453	-0.45159
0.0095	0.0689	-0.56318	-0.55196	-0.54960
0.0293	0.0292	-0.43926	-0.44987	-0.48012
0.0293	0.0500	-0.56981	-0.57250	-0.60418
0.0288	0.0667	-0.60907	-0.68470	-0.70404
0.0490	0.0480	-0.65788	-0.65488	-0.71606
0.0496	0.0315	-0.59181	-0.58992	-0.65686
0.0497	0.0684	-0.74340	-0.74784	-0.80110

Table 10

Excess molar volumes of ternary water (1)-methyl ethyl ketone (2)-acetone (3) mixtures [cm^3/mol]

X_2	X_3	293.15	300.15	307.15
0.0101	0.0098	-0.15437	-0.17491	-0.17067
0.0098	0.0294	-0.30382	-0.32209	-0.31812
0.0100	0.0441	-0.41428	-0.43341	-0.42995
0.0097	0.0648	-0.53417	-0.58299	-0.57861
0.0278	0.0350	-0.48183	-0.50218	-0.30207
0.0309	0.0505	-0.61549	-0.63058	-0.65074
0.0296	0.0695	-0.72471	-0.73727	-0.77875
0.0325	0.0497	-0.61482	-0.63501	-0.65577
0.0492	0.0295	-0.60133	-0.61667	-0.66908
0.0495	0.0662	-0.78890	-0.82471	-0.86475

The experimental findings reveal that the ternary mixtures under survey show negative deviations from the ideal value and generally increase with temperature increase. Probably, the main effects are the breakage of the dipole-dipole interactions.

The dependence between the refractive index and the density of binary and ternary fluid mixtures is calculated by means of empirical equations of the type $f(n) = k \cdot \rho$, where the k parameter depends on the type of fluids and wavelength used to measure the refractive index [10]. There are numerous equations of this type, the most common of which are: Lorentz–Lorenz ($f(n) = (n^2 - 1)/(n^2 + 2)$), Dale–Gladstone ($f(n) = n - 1$), Eykman ($f(n) = (n^2 - 1)/(n + 0.4)$), Oster ($f(n) = (n^2 - 1) \cdot (2n^2 + 1)/n^2$), Arago–Biot ($f(n) = n$) and New-ton ($f(n) = n^2 - 1$) [9]. These functions may be used to calculate the excess molar volumes according to the ratio suggested by Angel Pineiro et al. [11], which may also be extended to ternary systems:

$$Vm_{exc} = \sum_i Vm_i \cdot X_i \left(f_i / f - 1 \right) \quad (3)$$

where $f = f(n)$ for ternary fluid mixtures; $f_i = f(n_i)$ for pure compounds and X_i is the molar fraction. The writing of these equations is rather difficult and the resulting mathematical expressions are sometimes rather complex. A previous research suggested an modify Eykman equation to correlate the excess molar volumes with the refractive index for the binary water-propionic acid system [12]. For the ternary system: ethylbenzene–octane–propylbenzene it was preferred an MLR model that correlated the excess molar volumes with molar fractions, normalized temperature and refractive index and the findings were better, more precisely the standard deviation was only 0.03 [9].

In this paper, for the two ternary systems under survey, it was built mathematical MLR models by statistical processing of experimental data by using the Sigma Plot 11.0 software. It was achieved multi-linear regressions between the excess molar volumes and molar fractions, i.e. temperature and refractive index.

For the ternary water (1)-methyl ethyl ketone (2)-isopropyl alcohol (3) system, the MLR model has the following expression:

$$Vm_{exc} = -26.141 - (15.637 \cdot X_2) - (8.889 \cdot X_3) + (0.00290 \cdot T) + (19.525 \cdot n) \quad (4)$$

and the mean percentage deviation it was determined was 15.38%.

For the ternary water (1)- methyl ethyl ketone (2)-acetone (3) system, the MLR model has the following expression:

$$Vm_{exc} = 1.200 - (6.956 \cdot X2) - (6.975 \cdot X3) - (0.00169 \cdot T) - (0.889 \cdot n) \quad (5)$$

and the mean percentage deviation it was determined was 4.09%.

The results are shown in Figures 1 and 2. As one may notice, the correlation coefficients are superior to 0.9.

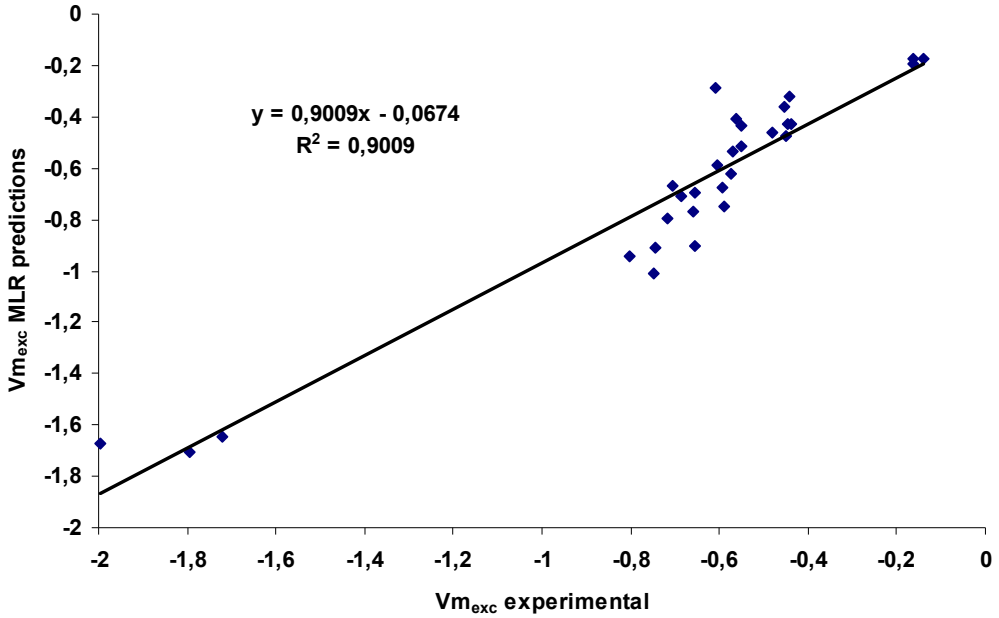

Fig. 1. Comparison of the experimental results to the ones calculated using the MLR model shown in equation 4 for: water - methyl ethyl ketone - isopropyl alcohol system

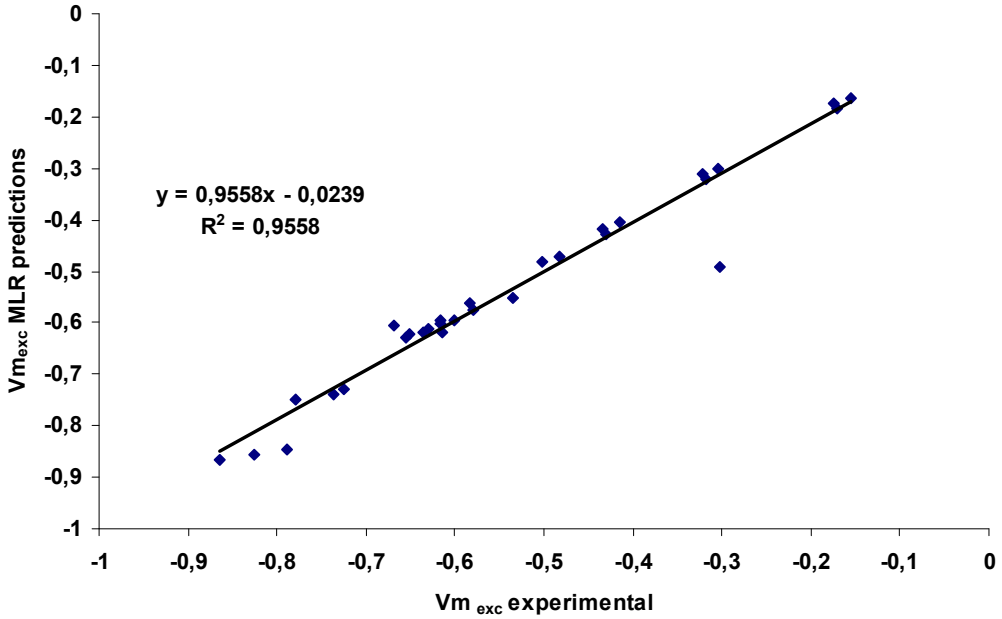

Fig. 2. Comparison of the experimental results to the ones calculated using the MLR model shown in equation 5 for: water- methyl ethyl ketone- acetone system

6. Conclusions

It was determined the refractive index (n) and the density (ρ) of the following ternary systems: water-methyl ethyl ketone-isopropyl alcohol and water-methyl ethyl ketone-acetone, in a composition range specific to diluted solutions, at the following temperatures: 293.15, 300.15 and 307.15 K, and atmospheric pressure. Based on these experimental data, it was calculated the excess refractive indices and the excess molar volumes, and it was established the type of deviation from ideal behavior. Bearing in mind that the refractive index may be experimentally determined much more easily, by means of the multiple linear regression (MLR) method it was were able to predict the excess molar volumes and implicitly the density of the ternary mixtures based on experimental determinations of the refractive index. The following models were suggested: $Vm_{exc} = a + b \cdot X_2 + c \cdot X_3 + d \cdot T + e \cdot n$. The correlation coefficients it was calculated were higher than 0.9.

Acknowledgment:
This work was supported by the "Program 4, Fundamental and Border Research, Exploratory Research Projects" financed by UEFISCDI, project No. 51/2017.

REFERENCES

[1] Rich J., Scheife R.T., Katz N., Caplan L.R., Isopropyl alcohol intoxication, *Archives of Neurology*, 47, (1990), 322-324.
[2] Mitran E., Callender T., Orha B., Dragnea P., Botezatu G., Neurotoxicity associated with occupational exposure to acetone, methyl ethyl ketone, and cyclohexanone., *Environmental Research*, 73, (1997), 181-188.
[3] Lisa G., Huhurez C., Matran R-M., Lisa C., Refractive indices of binary systems iso-propanol – water and iso-propanol – toluene, *Environmental Engineering and Management Journal*, 7, (2008), 309-312.
[4] Kyeong-Ho L., So-Jin P., Young-Yoon C., Density, refractive index and kinematic viscosity of MIPK, MEK and phosphonium-based ionic liquids and the excess and deviation properties of their binary systems, *Korean Journal of Chemical Engineering*, 34, (2017), 214-224.
[5] Almasi M., Iloukhani H., Densities, viscosities, and refractive indices of binary mixtures of methyl ethyl ketone + pentanol isomers at different temperatures, *Journal of Chemical & Engineering Data*, 55, (2010), 3918–3922.
[6] Mouli, J.C., Naidu, P.R., Choudary, N.V., Excess volumes, ultrasonic sound velocities, and isentropic compressibility's of 1-chlorobutane with isopropyl, isobutyl, and isopentyl alcohols, *Journal of Chemical & Engineering Data*, 31, (1986), 493-496.
[7] Kurtz Jr. S.S., Wikingsson A.E., Camin C.L., Thompson A.R., Refractive index and density of acetone-water solutions, *Journal of Chemical & Engineering Data*, 10, (1965), 330–334.
[8] Langdon W. M., Keyes D. B., Isopropyl alcohol-water system: density -composition data and pycnometric technique; plate factors in fractional distillation of isopropyl alcohol-water system, *Industrial and Engineering Chemistry*, 35, (1943), 459-469.
[9] Lisa C., Ungureanu M., Cosmatchi P.C., Bolat G., The density, the refractive index and the adjustment of the excess thermodynamic properties by means of the multiple linear

regression method for the ternary system ethylbenzene–octane–propylbenzene, *Thermochimica Acta*, 617, (2015), 76–82.
[10] Vuksanovic J.M., D.M. Bajic, G.R. Ivanis, Zivkovic E.M., Radovic I.R., Serbanovic S.P., Kijevcanin M.L.J, Prediction of excess molar volumes of selected binary mixtures from refractive index data, *Journal of the Serbian Chemical Society,* 79, (2014), 707–718.
[11] Pineiro A., Brocos P., Amigo A., Pintos M., Bravo R., Surface tensions and refractive indices of (tetrahydrofuran + n-alkanes) at T = 298.15 K, *The Journal of Chemical Thermodynamics*, 31, (1999), 931–942.
[12] Lisa G., Lisa C., Prediction of excess thermodynamic properties from experimental refractive index of binary mixtures 1. Water–propionic acid mixtures at 290.15, 300.15 and 310.15 K, *Revue Roumaine de Chimie*, 52, (2007), 647–653.

THE EFFECT OF ULTRASONIC CLEANING ON MEDICAL GRADE ANODIZED TITANIUM USED FOR DENTAL IMPLANTS

Dragos Vladimir BUDEI, Danut-Ionel VAIREANU*, Eliza BUZAMET, Emanuel AXENTE, Felix SIMA

Department of Inorganic Chemistry, Physical Chemistry & Electrochemistry, Faculty of Applied Chemistry and Materials Science, University Politehnica of Bucharest, 1-7 Gh. Polizu Street, 011061, Bucharest, Romania

Abstract

Titanium and titanium alloys of medical grade are preferred for dental implants for their excellent biocompatibility. In order to decrease the rejection percentage of such implants, it was found that electrochemically pretreating the surface by anodization producing self-organized titanium oxide nanotubes arrays will enhance the osteointegration chances of titanium implants. Although ultrasonic cleaning, as part of post-cleaning procedure, is used to get rid of the adsorbed traces of electrolyte, one noticed that, if used in excess, this may also fracture the obtained titanium oxide nanotube arrays. This paper attempts to compare a normal chemical cleaning procedure versus a chemical cleaning procedure used in connection with ultrasonic cleaning, in order to remove the electrolyte traces trapped at the implant surface, after the anodization, to decide whether or not the ultrasonic cleaning is a must and has to be included in the post-anodization procedure.

Key words: surface properties, anodized titanium, titanium oxide nanotubes, ultrasonic cleaning of dental implants

1. Introduction

Titanium and titanium alloys are some of the most used metals in the field of medical implants due to their inherent excellent biocompatibility (increased chemical stability, mechanical resistance, absence of toxicity) and some research concerning this field paid increased attention to find out the most suitable treatments to improve the osteointegration of such implants, particularly in restoring the missing dentition [1-6]. One key factor in this direction is the surface modification of implants, either by modifying the roughness of the implant

* Corresponding author. Email address: di_vaireanu@yahoo.co.uk (D.I. Vaireanu)

surface or by functionalizing the surface with various chemical, biochemical or biologically active materials [1], [4-5] [7-9].

The implant surface may be modified by grit-blasting, acid-etching or by a particular electrochemical treatment, namely anodization [7-8], [10]. It was found, however, that the best chances for the attached proteins to interact with cells, may occur when the implant surface was functionalized in the nanometer range, the nanostructured surface improving significantly the osteointegration of titanium implants [11]. Self-organized titanium oxide nanotubes arrays, particularly suitable as basic support for implant fictionalizations may be easily formed, under perfectly controllable conditions, by electrochemical anodization [10-16].

The formation of titanium oxide nanotube arrays by anodization in electrolytes containing fluoride ions may be best described by two competitive processes [12-16], the first one being the anodic formation of TiO_2 (equation 1 and 2), the second one being the chemical dissolution of titanium oxide in the presence of fluoride ions, at the titanium oxide/electrolyte interface (equation 3):

$$Ti + 2H_2O \rightarrow TiO_2 + 4H^+ + 4e^- \ (anodic\ reaction) \quad (1)$$

$$4H^+ + 4e^- \rightarrow 2H_2 \ (cathodic\ reaction) \quad (2)$$

$$TiO_2 + 6F^- \xrightarrow{4H^+} [TiF_6]^{2-} + 2H_2O \quad (3)$$

The actual mechanism of titanium oxide nanotube arrays formation and growth by electrochemical anodization can be simplified by dividing it into three stages [12-16]:

I. The formation of an initial barrier layer – a rapid oxide growth takes place on the surfaces of the anodized titanium due to the interaction of the metal (in fact metal ions obtained by anodization) with water. One may notice here a very sharp decrease in current density due to an increased in the total ohmic resistance, as a result of the formation of a compact film of oxide;

II. The formation of uniformly distributed pores - small pits, similar to those produced by pitting corrosion, but at a nanometer level scale, are formed in the oxide film produced by anodization, due to a localized chemical dissolution process, depicted by equation 3, forming a barrier layer at the bottom of the pits, which will lead to an increase in the electrical field intensity across the remaining barrier layer, increasing the current density and resulting in further pore growth;

III. Separation of interconnected pores into nanotubes – a separate region between the formed pores will appear, so that the resulting nanotube formation is a direct consequence of simultaneous formation of oxide due to field assisted oxidation and the process of chemical dissolution in the presence of fluoride ions.

The anodization process is strongly influenced by the proper cleaning (before and after anodization), in the absence of this or in the case of poor cleaning there is a danger that the implants may be rejected for not fulfilling the medical standards, a very costly outcome [17-19]. The explanation for this is that tiny screws, with tight threads, may adsorb and trap reagents used during the anodization process, these reagents becoming unwanted contaminants from the medical point of view, and in the case of fluoride ions being particularly toxic, and such contaminants are difficult to remove using a classical normal cleaning by washing and rinsing.

The use of ultrasonic cleaning was used extensively to get rid of the unwanted residues of electrolyte. If high frequency sound waves are passed through liquids, a cavitation process takes place, tiny bubbles being created on all surfaces, and, at the same time, being rapidly destroyed by implosion, due to the oscillating zones of high and low pressure, transferring the energy to the washed parts and contaminants, which are dislocated from the implants and relocated into the washing liquid.

Although ultrasonic cleaning may offer a real and affordable cleaning solution as part of the titanium anodizing procedure, it was noted that, in some circumstances, ultrasonic cleaning tends to fracture the obtained titanium oxide nanotube arrays.

The aim of this study is to verify if normal chemical cleaning is enough to remove the electrolyte traces trapped at the implant surface after the anodization, and to compare this with a normal ultrasonic cleaning, to decide whether or not the ultrasonic cleaning is a must and has to be included in the post-anodization procedure.

2. Experimental

Reagents

All the reagents used in this study were *p.a*. from Sigma-Aldrich, Merck, and Chimopar. The electrolyte used during the anodization procedure was prepared using distilled water. Titanium used for anodization is 99.9% Ti Grade 4 of medical grade produced by Dynamet USA.

Apparatus and procedure

The equipment used for the titanium implants anodization, the electrolyte composition of the anodization bath and the anodization procedure are subjected to a patent pending procedure. The actual implants were obtained from medical grade 4 titanium produced by Dynamet USA, using a 9-axis Citizen Cincom L20 CNC Swiss Type lathe produced in Japan.

The milled implants were sandblasted using Al_2O_3 (corundum), 70 μm in size, for 30 seconds. The ultrasonic bath used for the ultrasonic cleaning was

Condel 3106, Germany, with an active power of 50 W, operated at a fixed frequency of 35 kHz, and it was provided with an automatic switch off programmable timer. Prior to anodization the implants were cleaned in the ultrasonic bath for 8 minutes @ 40 ^{o}C for each stage: twice in distilled water with liquid soap 1%, twice in distilled water, twice in acetone, twice in isopropyl alcohol in order to get rid of the grease (lubricating mineral oil from the milling stage) and any other contaminants which may impurify the anodization bath. A ten times more powerful cleaner, an Elmasonic X-tra 30H Ultrasonic Cleaner Bath, Germany, 35 kHz, 480 W, was used to investigate the effect of excessive ultrasonication. One has collected samples cleaned ultrasonically before the anodization and samples after the anodization cleaned chemically only and cleaned chemically in the ultrasonic bath. Scanning Electron Microscopy (SEM) was used to investigate the surface morphology of the anodized Titanium implants with a FEI Inspect S electron microscope. The measurements were performed at 30 kV acceleration voltages, in high vacuum.

3. Results and discussions

The shape and dimensions of an implant are presented in Figure 1 (one may also see the rod system used for suspending these implant in the anodization bath to avoid a possible anodic dissolution as one has to fully immerse the implant in the bath and at the same time to avoid any anodic dissolution should the contacting rod be made of a different metal). After the anodization, the contacting rod is detached by breaking it from the main body of the implant and the implant is sent for post-anodization cleaning.

Scanning electron microscopy (SEM) was used to characterize the anodized titanium. One has measured the inner diameters and the wall thickness of titanium oxide nanotubes arrays produced by anodization (see Table 1), and it was found that their dimensions are well within the results reported in the literature [7], [10-11] [13-17].

Fig. 1. Samples of the mechanically milled titanium implants with **a)** (before) anodization) and without **b)** the suspending rod (after anodization) (2 mm diameter, 4 mm length)

Table 1

Dimensional characteristics of titanium oxide nanotubes produced by anodization

No.		Inner diameter, nm	Wall thickness, nm
1	Min	25	7
2	Max	104	8

In Figure 2 is presented a sandblasted implant before the anodization procedure, chemically cleaned @ 40 ºC in conjunction with ultrasonic cleaning. The surface morphology is a smooth one, corresponding to that of an object produced by milling.

In the absence of ultrasonication, one may see crystals of fluoride salts and other solid contaminants trapped within the titanium oxide nanostructures (Figure 3) showing that a classical chemical cleaning with distilled water and alcohol is not enough for a thorough cleaning. In contrast with this, ultrasonically assisted chemical cleaning managed to get rid of these unwanted contaminants (Figure 4).

The use of excessive ultrasonic cleaning tends to fracture and level the titanium oxide nanostructure, leading to a rather planar honeycomb based nanostructure (Figure 5 versus Figure 6).

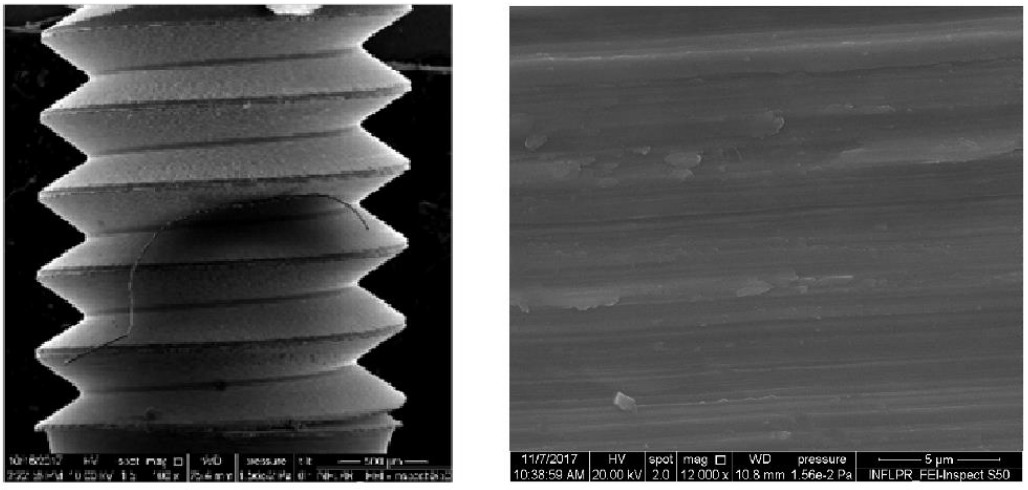

a) **b)**

Fig. 2. a) Low (200x maginification) and **b)** high (12000x) magnification SEM picture of the implant before anodization, chemically cleaned @ 40 ºC in conjunction with ultrasonic cleaning (2 times in distilled water with liquid soap 1%, 2 times in distilled water, 2 times in acetone, 2 times in isopropyl alcohol), 8 minutes/stage, the ultrasonic bath characteristics: 50 W, 35kHz

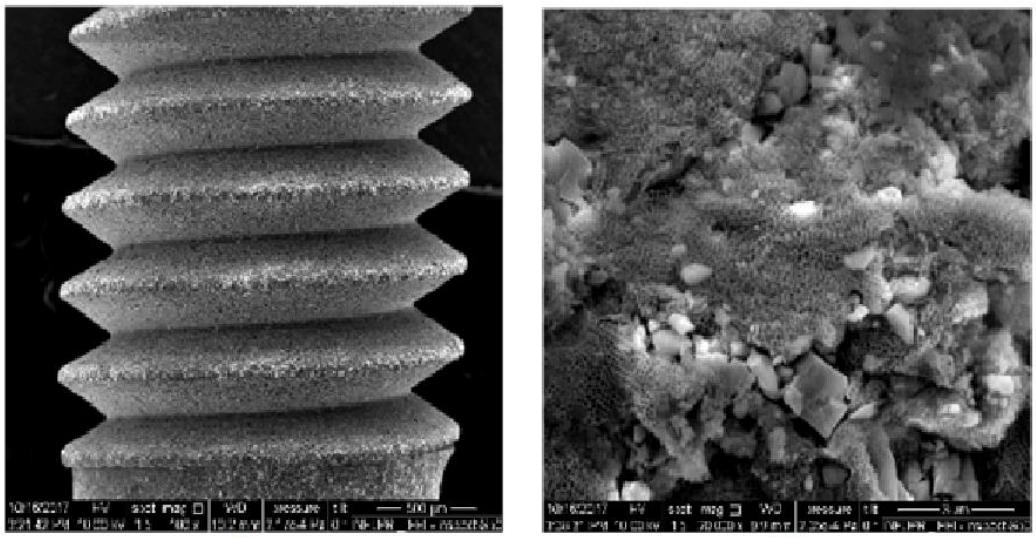

a) b)

Fig. 3. Chemical cleaning. Low **a)** 200x magnification and high **b)** 20000x magnification SEM picture of anodized titanium surface, chemically cleaned only @ 40ºC (twice in distilled water, once in isopropyl alcohol)

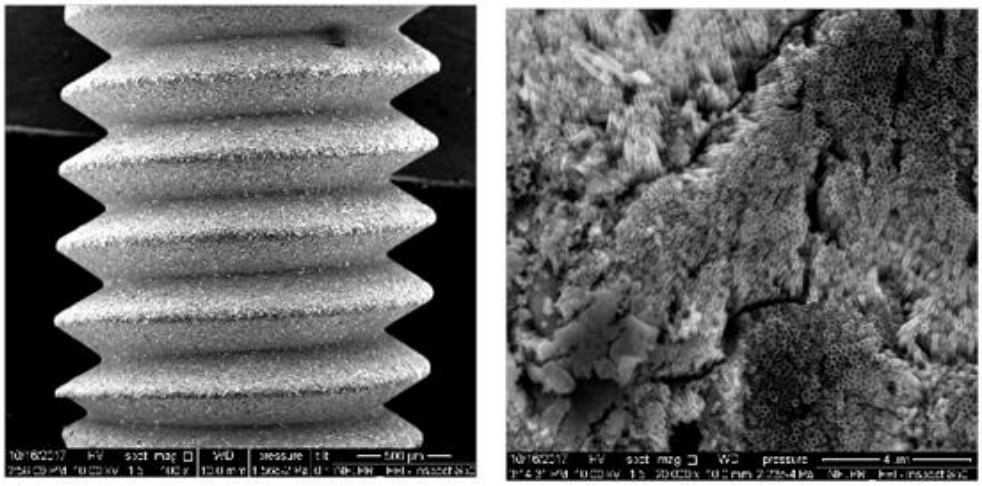

a) b)

Fig. 4. Chemical cleaning used in conjunction with ultrasonic cleaning Low **a)**200x magnification and high **b)**20000x magnification SEM picture of anodized titanium surface, chemically cleaned @ 40 ºC in conjunction with ultrasonic cleaning (2 times in distilled water, 1 time in isopropyl alcohol). Each stage lasted 3 minutes, the ultrasonic bath characteristics: 50 W, 35kHz

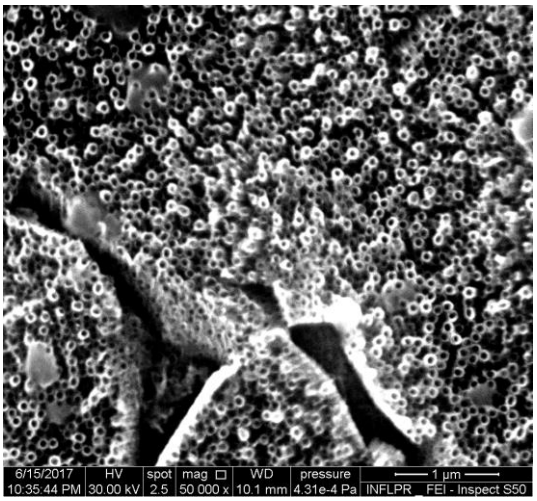

Fig. 5. SEM image of an anodized implant subjected to a chemical cleaning @40 ºC used in connection with a soft ultrasonic cleaning procedure (3 minutes, 50 W, 35kHz, and: twice in distilled water and once in isopropyl alcohol)

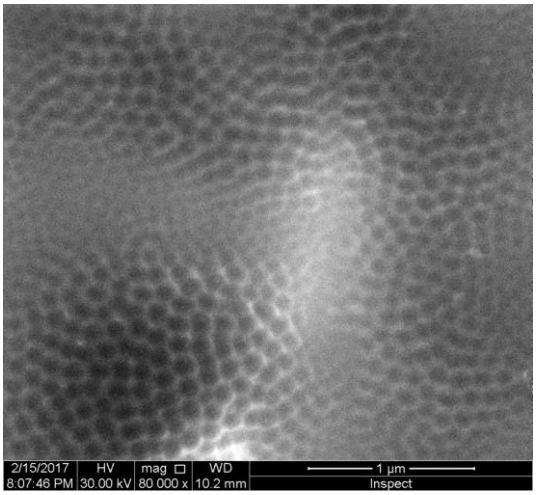

Fig. 6. The effect of extensive ultrasonication
SEM image of an anodized implant, 80000x magnification, subjected to an increased power (9.6 times) excessive ultrasonic cleaning procedure (2 minutes, 480 W, 35kHz, and 40 C: twice in distilled water and once in isopropyl alcohol)

4. Conclusions

The use of ultrasonication chemical cleaning, as a post-anodization cleaning phase, is a very useful *sine qua non* stage during the production of the anodized dental implants, obtained in fluoride based electrolytes, as chemical cleaning by itself is not enough to remove the electrolyte traces and other contaminant trapped at the implant surface.

One should however use it carefully, and initial verifications are compulsory, as an excessive ultrasonic cleaning tends tend to destroy and level the fragile titanium oxide nanostructure.

This disadvantage may be used as a control lever should one desire to obtain a more planar titanium oxide nanostructure required in some instances for particular fictionalizations with biological active materials.

Acknowledgements

This research was supported by Dentix Millennium SRL through the project "Dental implants surface functonalization for improved osseointegration – an innovative method" ("Metodă inovativă pentru funcţionalizarea suprafeţelor implanturilor dentare cu scopul îmbunătăţirii osteointegrării") code MySMIS 104809, contract no. ANCSI 73/8.09.2016.

REFERENCES

[1]. Yanko, V. M., Surface treatment of titanium components with the aim of improving operating properties, *Chem. Pet. Eng.* 49, 7, (2013), 44 – 45.

[2]. Geetha, M., Singh, A.K., Asokamani, R.A. Gogia, K., Ti based biomaterials, the ultimate choice for orthopaedic implants–a review, *Prog. Mater Sci.*, 54, 3, (2009), 397-425.

[3]. Alhag, M., Renvert, S., Polyzois, I., Claffey, N., Re-osseointegration on rough implant surfaces previously coated with bacterial biofilm: an experimental study in the dog. *Clin Oral Implants Res*. 19, (2008), 182-187.

[4]. Schwarz, F., Sahm, N., Iglhaut, G., Becker, J., Impact of the method of surface debridement and decontamination on the clinical outcome following combined surgical therapy of peri-implantitis: a randomized controlled clinical study, *J. Clin. Periodontol.* 38, 3 (2011), 276-284.

[5]. Ungvari, K., Pelsoczi, I.K., Kormos, B., Oszko, A., Rakonczay, Z., Kemeny, L., Radnai, M., Nagy, K., Fazekas, A., Turzo, K., Effects on titanium implant surfaces of chemical agents used for the treatment of peri-implantitis. *J. Biomed. Mater Res. B Appl. Biomater.*, 94, (2010), 222-229.

[6]. Elias, C.N., Meirelles, L., Improving osseointegration of dental implants, *Expert Rev Med Devices*, 7, (2010), 241-256.

[7]. Nishimoto, S.K., Nishimoto, M., Park, S.W., Lee, K.M., Kim, H.S., Koh, J.T., Ong, J.L., Liu, Y., Yang, Y., The effect of titanium surface roughening on protein absorption, cell attachment, and cell spreading, *Int. J. Oral. Maxillofac. Implants*, 23, (2008), 675-680.

[8]. Pae, A., Kim, S.S., Kim, H.S., Woo, Y.H., Osteoblast-like cell attachment and proliferation on turned, blasted, and anodized titanium surfaces, *Int. J. Oral Maxillofac. Implants*, 26, (2011), 475-481.

[9]. Piattelli, M., Scarano, A., Paolantonio, M., Iezzi, G., Petrone, G., Piattelli, A., Bone response to machined and resorbable blast material titanium implants: an experimental study in rabbits, *J. Oral Implantol.*, 28, (2002), 2-8.

[10]. van Vuuren, D., Laubscher, R., Surface friction behaviour of anodized commercially pure titanium screw assemblies, *Procedia CIRP* 45, (2016), 251-254.

[11]. Salou, L., Hoornaert, A., Louarn, G., Layrolle, P., Enhanced osseointegration of titanium implants with nanostructured surfaces: An experimental study in rabbits, *Acta Biomaterialia*, 11, (2015), 494-502.

[12]. Mor, G. K., Varghese, O. K., Paulose, M., Shankar, K., Grimes, C. A. A review on highly ordered, vertically oriented TiO2 nanotube arrays: fabrication, material properties, and solar energy applications, *Solar Energy Materials and Solar Cells*, 90, (2006), 2011-2075.
[13]. Crawford, G. A., Chawla, N., Das, K., Bose, S., Bandyopadhyay, A. Microstructure and deformation behavior of biocompatible TiO2 nanotubes on titanium substrate, *Acta Biomaterialia* 3, (2007), 359-367.
[14]. Sobieszczyk, S. Self-organized nanotubular oxide layers on Ti and Ti alloys, *Advances in Materials Sciences*, 9, (2009), 25-41.
[15]. Macak, J. M., Tsuchiya, H., Ghicov, A., Yasuda, K., Hahn, R., Bauer, S., Schmuki, P., TiO2 nanotubes: self - organized electrochemical formation, properties and Applications, *Current Opinion in Solid State & Materials Science*, 11, (2007), 3-18.
[16]. Macak, J. M., Sirotna, K., Schmuki, P., Self-organized porous titanium oxide prepared in Na_2SO_4/NaF electrolytes, *Electrochimica Acta*, 50, (2005), 3679-3684.
[17]. Lee, T. C., Mazlan, M. H. H., Abbas, M. I., Abdullah, H., Idris, M.I., Effect of Ultrasonic Amplitude on Surface Properties of Anodized Titanium for Biomedical Application, *Materials Science Forum*, 840, (2016), 160-164.
[18]. Kawashima, H., Sato, S., Kishida, M., Yagi, H., Matsumoto, K., Ito, K,. Treatment of titanium dental implants with three piezoelectric ultrasonic scalers: an in vivo study, *J. Periodontol.*, 78, (2007), 1689-1694.
[19]. Sato, S, Kishida, M., Ito, K., The comparative effect of ultrasonic scalers on titanium surfaces: an in vitro study, *J. Periodontol*., 75, (2004), 1269-1273.

PALLADIUM AND COPPER CATALYST FOR FURFURAL HYDROGENATION

Andreea A ŢURCANU[1,*] , Rami DOCKEH[1], Sanda VELEA[2], Mihaela BOMBOŞ[2], Gabriel VASILIEVICI[2], Paul ROŞCA[3]

[1] SC Research Institute for Auxiliary Organics Products SA, ICPAO Mediaş, 8 Carpaţi Str., 551022, Mediaş, Romania

[2] Department of Bioresources, National Research and Development Institute for Chemistry and Petrochemistry- ICECHIM-Spl. Independenţei 202, 060021, Bucharest, Romania

[3] Department of Petroleum Processing and Environmental Protection, Petroleum and Gas University of Ploieşti, 39 Bucureşti Str., 100680 Ploieşti, Romania

Abstract

The hydrogenation reaction of furfural was studied in a fixed bed catalytic reactor, operated in continuous flow, in isothermal conditions using a copper-palladium catalyst on a γ alumina support. The catalyst was characterized by determining its acid strength distribution using the diethyl amine thermodesorption method and textural characteristics. The Cu-Pd catalyst presented high efficiency in the furfural hydrogenation process giving a furfural conversion of ~ 98% and yielding in furfuryl alcohol (72.06%) and tetrahydrofurfuryl alcohol (25.78%).

Key words: Furfural, hydrogenation, acidity, catalysts

1. Introduction

Recently, furfural has recaptured attention as a potential source for biofuel and biochemicals. Bozell et al. considered it to be one of the most promising substances for sustainable production of fuels and chemicals in the 21st century [1]. Furfural, having a very flexible production, is the most commonly obtained industrial product. Furfural and its derivatives have been widely used in the plastics, pharmaceutical and agrochemical industries, as fungicides and insecticides, transport fuels, gasoline additives, aviation fuel, lubricants, resins, bleaching agents, drugs, flavor enhancers for food and beverages, and also for wood modification and book preservation [2,3].

Because of its high reactivity in condensation-polymerization reactions that can occur, furfural must be subjected to a hydrogenation process to improve its stability and reduce the number of reactive functional groups, like the carbonyl group. The hydrogenation process is complex, due to the series of parallel reactions, such as furan ring hydrogenation, the carbonyl group hydrogenation and also hydrogenolysis. This kind of reactions is favored by the acidic centers in the catalysts, leading to a decrease in the selectivity of furfural transformation. To improve the life of the catalyst used, the acidic characteristics must be kept in

* Corresponding author: Email address: andreea.turcanu90@yahoo.com

mind, because the selectivity of furfural hydrogenation process is influenced by the strength of the acidic centers of the catalyst [4].
As reported in literature, the main products obtained in the hydrogenation process of furfural are furfuryl alcohol (FA), tetrahydrofurfuryl alcohol (THFA), 2-methylfuran (MF), tetrahydro-2-methylfuran (THMF) as presented in Figure 1. It also shows the continuing of the hydrogenation process for the product earlier obtained, using different metal catalysts and in specific conditions for each product.

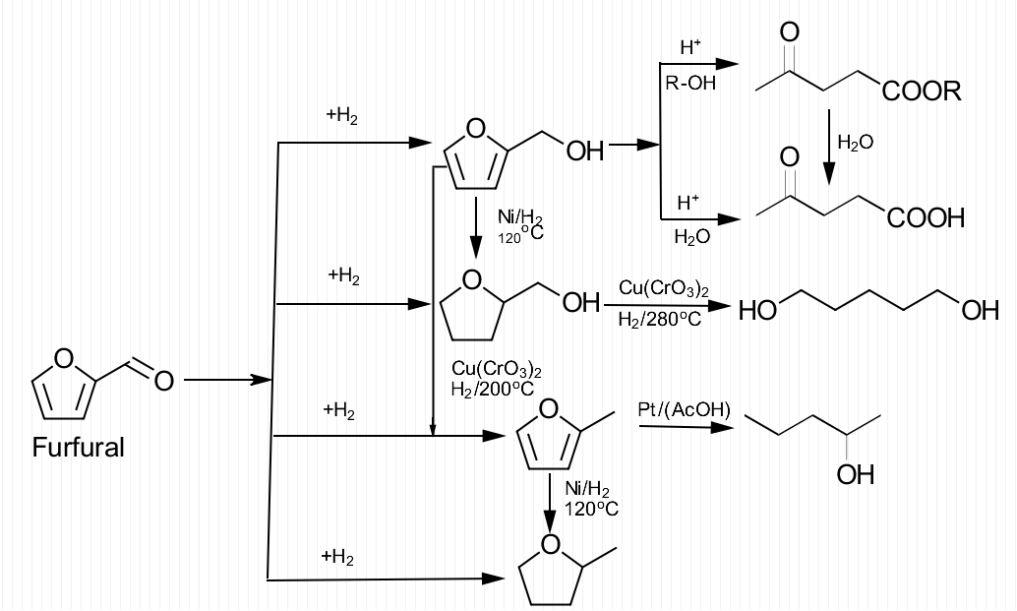

Fig 1. Possible reactions in the furfural hydrogenation process

Liquid-phase transfer hydrogenation of furfural using Cu based catalyst was performed by María M. Villaverde et al. [5]. The experiments were carried out using different Cu loadings (20%w, 30%w, 40%w), in a temperature range 110°C-150°C, using as H donor 2-propanol. They found that the Cu-Mg-Al catalyst containing 40%w Cu presented the best results, with a 100% conversion of furfural to FA at 150˚C, after 8 hours of reaction, thus showing that the rate of transfer hydrogenation increases with the Cu amount.
In their research, Á. O'Driscoll et al. [6] studied the influence of different metals and supports on monometallic and bimetallic catalysts activity for the liquid phase hydrogenation of furfural to FA. Metals like copper, palladium, nickel and platinum were used to prepare 1%w and 2%w monometallic catalysts by wet impregnation method, on supports like SiO_2, β zeolite, TiO_2, active carbon, Al-SBA-15. They found that out of all the metals and supports tested, Pt and SiO_2 gave the best conversion of furfural and the best FA selectivity, thus selecting Pt to be further tested in bimetallic catalysts. The bimetallic catalysts were prepared

by surface reaction and the second metals used were selected by their electronegativity because if the second metal (the promoter) is more electropositive then the first metal the interactions with the carbonyl group in furfural increases [7]. The 0.6%Pt0.4%Sn/SiO_2 catalyst presented a 47% furfural conversion and almost 100% selectivity to FA at 100˚C and 20 bar hydrogen pressure, using toluene as solvent.

The influence of Sn was also studied on a R-Ni/AlOH catalyst by Rosiansono et al. [8]. The catalyst was prepared by a simple method at low temperature. The Ni-Sn(3.0)/AlOH presented the best results at 453 K temperature for one hour, and a hydrogen pressure of 3MPa, using methanol as solvent, obtaining a >99% furfural conversion and a 98% yield in FA.

Jiménez-Gómez et al. [9] studied a series of Cu/CeO_2 catalysts for the gas phase hydrogenation of furfural. The catalysts were prepared using a co-precipitation method and had Cu/Ce molar ratios between 0.2 and 6. Because of the strong metal-cerium interaction the catalysts presented high stability and great catalytic behavior, the most efficient proving to be Cu-CeO_2-6 catalyst, where a furfural conversion of 83% was achieved after 5 hours of time on stream (TOS) at a temperature of 190ºC. The only products obtained were MF and FA, the majority product being influenced by the TOS, thus MF was the majority product at shorter reaction times, while the yield in FA increases at higher reaction times due to formation of carbonaceous deposits which determine the hydrogenolysis of the alcohol to MF.

Noble metals like Pd and Pt have also captured the attention of researchers, being used to obtain catalysts for furfural hydrogenation. S. Bhogeswararao and D. Srinivas [10] tested a series of Pt and Pd based catalysts on a γAl_2O_3 support for furfural hydrogenation. The Pd based catalysts favored the hydrogenation of the furan ring, yielding in THFA, while the Pt catalyst favored the C=O group hydrogenation, yielding in FA. The reactions were carried out at 25ºC. With temperature increase the Pd catalyst enabled the decarbonylation of furfural, resulting in a yield in furan of 82%.

The main objective of this research was to design an efficient catalyst for selective hydrogenation of furfural to oxygenated furan derivatives having a low oxygen content and good stability. Copper and palladium based catalysts supported on $\gamma Al_2O_3$with controlled acidity were synthesized. Addition of copper aimed to improve the hydrogenation of the furfural carbonyl group, while the palladium was employed for the furan ring saturation.

2. Materials and methods

Materials

The raw materials used in the experiments were furfural p.a (Sigma-Aldrich), $Cu(NO_3)_2 \cdot 3H_2O$ p.a (Sigma-Aldrich), $PdCl_2$ p.a (Sigma-Aldrich), granulated γ alumina and electrolytic hydrogen purity from Linde Company.

Catalyst preparation

The Cu-Pd/γAl_2O_3 catalyst was prepared by successively impregnating the γAl_2O_3 support with aqueous solutions of the Cu and Pd precursors, applying the pore-filling method. The aqueous solutions were prepared at the desired concentration according to the desired metal content (3%Cu and 0.5%Pd/ γAl_2O_3). The first metal to be deposited on the γAl_2O_3 support was Pd, then Cu. Between the impregnations, the catalyst was dried at 160˚C for 4 hours and at the end dried at 160˚C for 6 hours and calcinated at 450˚C for 6 hours. The catalyst reduction was done using an aqueous solution containing the equivalent amount of sodium borohydride.

Catalyst characterization

The catalyst characterization was performed by determining the textural properties (such as surface area, pore volume, average pore diameter, pore size distribution) using an Autosorb 1 Quantacrome Nova 2200 Analyzer and determining the acid strength distribution by applying the diethyl amine thermodesorption method using a DuPont Instruments Thermal Analyst 2000/2100&951TGA coupled with a Thermogravimetric Analizer module 951.

The porous structure of the γAl_2O_3 support and catalyst was characterized by N_2 adsorption-desorption. The BET equation was used to determine the surface area while the pore distribution and size were determined by applying the BJH method.

Furfural hydrogenation

The furfural hydrogenation process was carried out in a fixed bed catalytic reactor, operated in continuous flow, in isothermal conditions. The temperature was controlled using an automatic system coupled with two fixed thermocouples, situated in the reactor jacket. In order to measure the reaction temperature, on the reactor's axis was placed a metallic jacket for the mobile thermocouple.

The reaction conditions were as follows: the reaction was carried out at various temperatures in the range of 135-220ºC, pressures between 20 and 60 bar, a hydrogen/furfural molar ratio of 10:1 and a $0.15h^{-1}$ liquid hourly space velocity (LHSV).

The reaction products were characterized by GC-MS (Varian -3800). Operational parameters for the GC method were: column VF-5ms 30m X 0.25mm, ID DF=0.25; the oven program was set at 175°C with a temperature gradient of 16°C/min, the carrier gas used was He and the injector temperature was 155ºC.

For the MS method the parameters were: collision cell QQQ: Flow Quench Gas (He) 2.2 mL/min with collision gas flow of 1.5 mL/min, a 70eV electron energy and the source temperature was 230ºC.

3. Results and discussions

To determine the acid strength distribution of the materials, the diethyl amine thermodesorption method was applied in the temperature range 20-600°C. The diethyl amine thermodesorption curves for the γAl_2O_3 support, 0.5%Pd/ γAl_2O_3 and for the catalyst 3%Cu-0.5%Pd/ γAl_2O_3 are presented in Figure 2 a, b and c.

The mass losses recorded on the thermodesorption curves at temperatures between 150-300ºC (zone A) are attributed to the diethyl amine desorption from the weak acidic centers, between 300-440ºC (zone B) the desorption of diethyl amine from the acidic centers with medium acidity and between 440-580ºC (zone C) are attributed to the thermodesorption from strong acidic centers. Total acidity is defined as the mass of desorbed amine from acidic centers, expressed as mEg/gram of catalyst (mEg/g_{cat}).

Based on the diethyl amine thermodesorption curves, the acid strength distribution of the materials was determined and presented in Table 1. As observed from the values obtained, for the γAl_2O_3 support the strong acidic centers are found at the lowest concentration, with the weak acidic centers having a higher concentration than the ones for medium and strong acidic centers. After impregnating the support with the Pd precursor, as expected, the concentration of medium and strong acidic centers raises slightly compared with the γAl_2O_3 support, but the total acidity has a lower value compared with the one of the support. After adding the Cu precursor, the medium acidic centers are found at the lowest concentration while the weak acid centers concentration raises considerably, with its value being higher than the concentration of the strong acidic centers and much higher than the one of the medium acidic centers.

Figure 3 presents the pore size distribution of the materials. As observed from the BJH desorption method, the materials present big, well defined pores with a maximum distribution for the 3%Cu-0.5%Pd/γAl_2O_3 catalyst centered at about 95 Å. The specific surface area of the catalyst is typical for γAl_2O_3 supported catalysts with values higher than $200 m^2/g$. With the precursors addition to the support the value of the surface area decreases from $232.34 m^2/g$ to $224.01 m^2/g$ for the 3%Cu-0.5%Pd/γAl_2O_3. Also the pore volume decreases from 0.530 cm^3/g to 0.486 cm^3/g. The medium pore diameter of the 3%Cu-0.5%Pd/γAl_2O_3 catalyst is 9.58 nm which puts the catalyst in the mesoporous category. The textural characteristics of the materials are presented in Table 1.

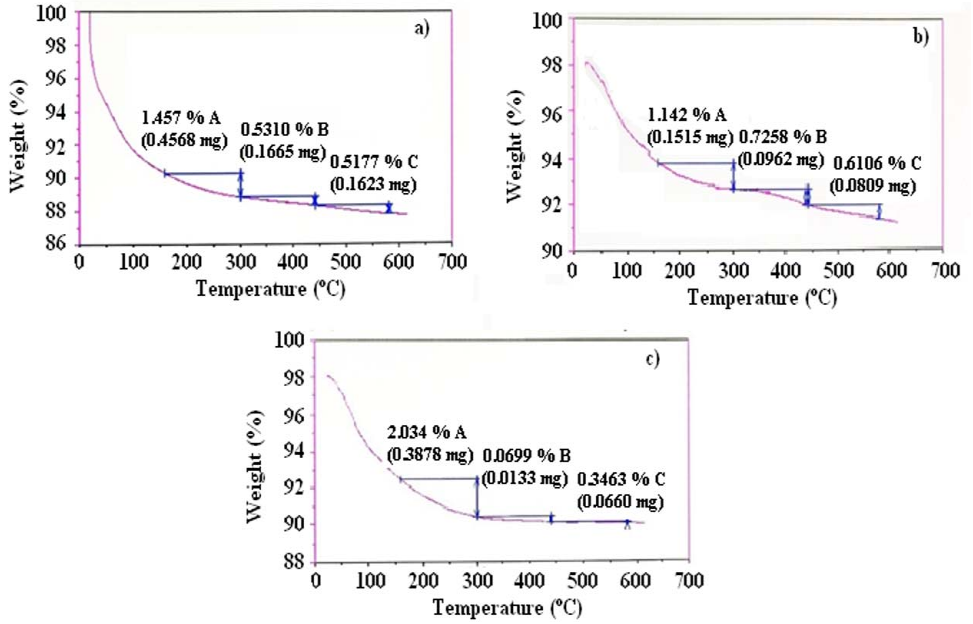

Fig. 2. Diethyl amine thermodesorption curves for: a) γAl_2O_3 support, b) 0.5%Pd/γAl_2O_3 and c) 3%Cu-0.5%Pd/γAl_2O_3

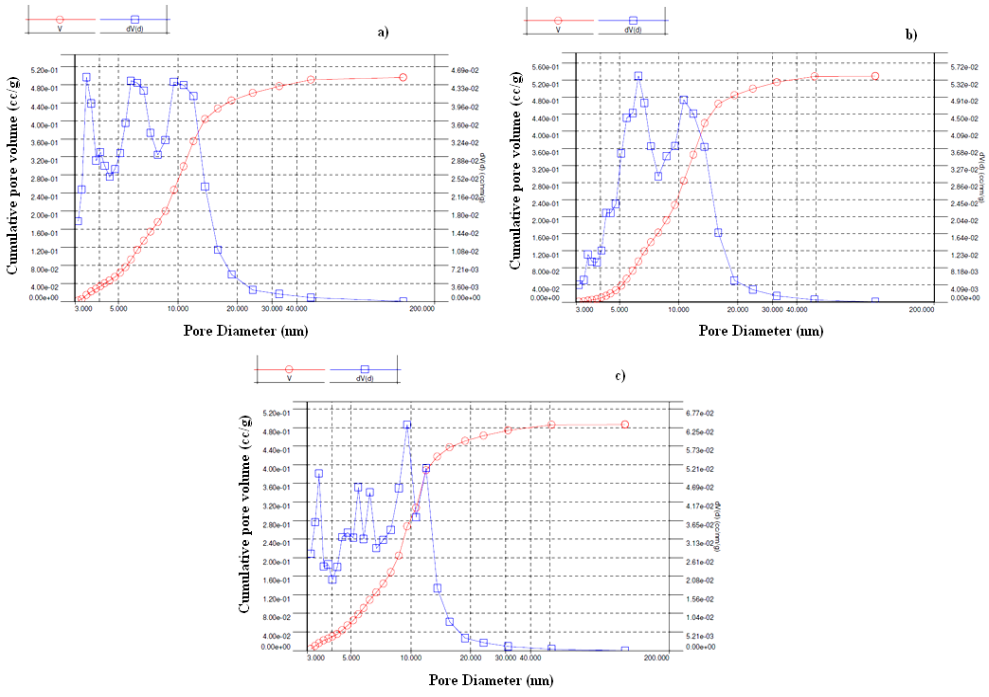

Fig. 3. Pore size distribution for: a) γAl_2O_3 support, b) 0.5%Pd/γAl_2O_3 and c) 3%Cu-0.5%Pd/γAl_2O_3 by BJH desorption method

Table 1.

Acid strength distribution and textural characteristics for γAl_2O_3 support, 0.5%Pd/ γAl_2O_3 and 3%Cu-0.5%Pd/ γAl_2O_3

Materials	S_{BET} (m2/g	Pore volume (cm3/g)	Medium pore diameter (nm)	Acid strength distribution (mEg/g_{cat})			
				Weak	Medium	Strong	Total
γAl_2O_3	232.34	0.530	3.44	0.199	0.072	0.070	0.341
0.5%Pd/ γAl_2O_3	230.11	0.496	6.24	0.156	0.099	0.083	0.338
3%Cu-0.5%Pd/γAl_2O_3	224.01	0.489	9.58	0.278	0.009	0.047	0.334

For furfural hydrogenation the 3%Cu-0.5%Pd/γAl_2O_3catalyst presented a high activity in the parameters ranges that were studied. As can be seen from figure 4, furfural conversion varies according to a parabolic curve with a maximum of 97.84% at 180˚C, for a pressure of 40 bar and a 0.15 h^{-1}LHSV. At temperatures higher than 180˚C the conversion starts to decrease, possibly due to the formation of gums that block the pores of the catalyst, deactivating it. The presence of strong acidic centers at relatively high concentrations (0.334 mEg/g) favors the condensation reactions with the formation of gums, mostly at temperatures higher than 180˚C.

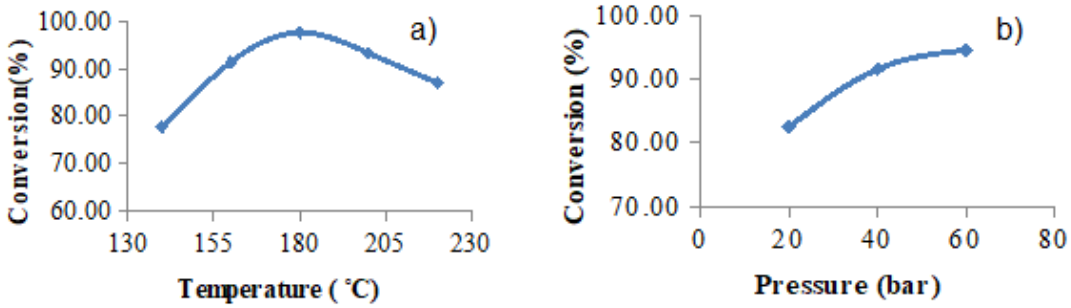

Fig. 4. Temperature and pressure influence on the furfural conversion: a) influence of temperature at 40 bar; b) influence of pressure at 160 °C.

Also, at a temperature of 160˚C and 0.15 h^{-1} LHSV, with the increase in pressure the furfural conversion increases, reaching a maximum value of ~94.5% at 60 bar. It can be noted a diminution of the curve slope variation which represents the furfural conversion with the pressure at values higher than 40 bar.

The products obtained from the furfural hydrogenation with 3%Cu-0.5%Pd/γAl_2O_3 catalyst were FA and THFA, with FA as the majority component obtained. Figures 5 and 6 show the temperature and pressure influence on the yield in FA and THFA.

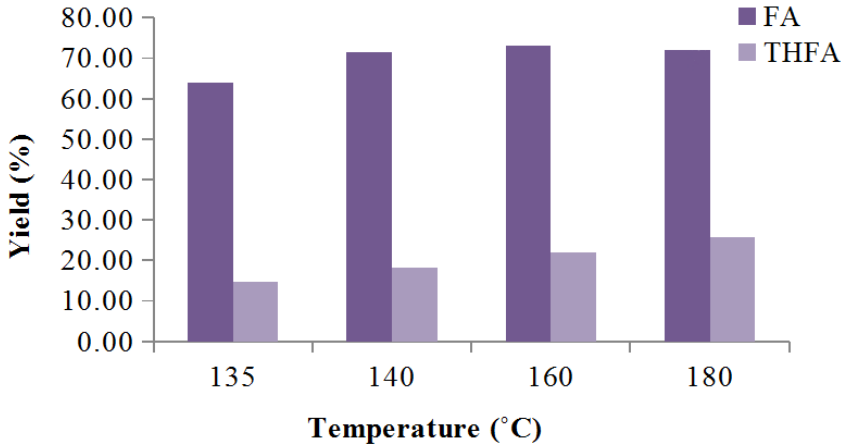

Fig. 5. Temperature influence on the yield in FA and THFA, at 40 bar pressure and 0.15h^{-1} LHSV

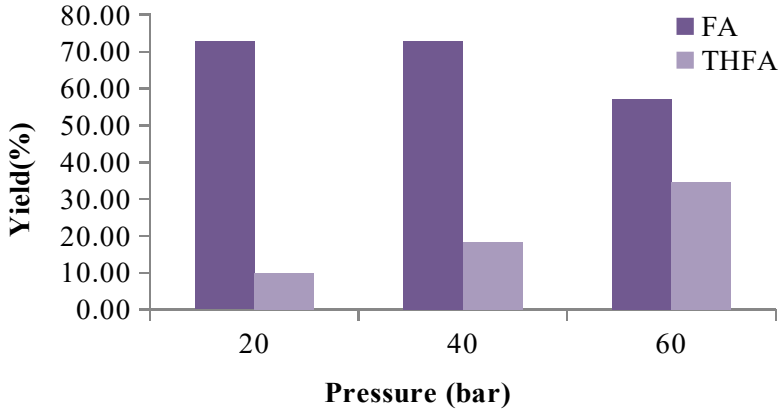

Fig. 6. Pressure influence on the yield in FA and THFA, at 160˚C and 0.15h^{-1} LHSV

The yields in FA and THFA increase with temperature, with a maximum yield in FA of 72.97% at 160˚C and 25.78% maximum yield in THFA at 180˚C. With the pressure increase the yield in FA decreases while the yield in THFA increases with a maximum of 34.54% at 160˚C, 60 bar and 0.15h^{-1} LHSV. The diminishing of the yield in FA at temperatures above 160°C is due both to its hydrogenation to THFA and to the condensation reactions of FA to resins, reactions favored by the presence of strong acid centers.

Pressure growth favors hydrogenation of FA to THFA, relatively low values of yield to THFA are due to a relatively high concentration of acid centers and especially of strong acid centers.

4. Conclusions

The 3%Cu-0.5%Pd/γ-Al2O3 catalyst presents a specific high surface area and pore diameters specific to mesoporous catalysts. The furfural hydrogenation process was carried out in a fixed bed catalytic reactor, operated in continuous flow and isothermal conditions, temperature 135-220˚C, pressure 20-60 bar and a 0.15 h^{-1} LHSV. The main products obtained were furfuryl alcohol and tetrahydrofurfuryl alcohol. The catalyst was most efficient at 180˚C, 40 bar pressure giving a maximum furfural conversion of 97.84% with a 72.06% yield in furfuryl alcohol and 25.78% yield in tetrahydrofurfuryl alcohol. The yield in tetrahydrofurfuryl alcohol increases with pressure, reaching a maximum value of 35.57% at 160˚C and a 60 bar pressure.

A lower yield in THFA than in FA is due to an inappropriate ratio between Cu and Pd metal centers but also to an inadequate acid strength distribution.

Acknowledgement

Anca Andreea Ţurcanu acknowledges the financial support received as doctoral scholarship from Petroleum and Gas University of Ploieşti and the scholarship from the Society of Chemical Engineering to attend at RICCCE 20 Conference.

REFERENCES

[1] Bozell J.J., Petersen G.R., Technology development for the production of biobased products from biorefinery carbohydrates—the US Department of Energy's "Top 10" revisited, *Green Chemistry*, 12, (2010), 539–554.

[2] Yan K., Wu G., Lafleur T., Jarvis C., Production, properties and catalytic hydrogenation of furfural to fuel additives and value-added chemicals, *Renewable and Sustainable Energy Reviews*, 38, (2014), 663–676.

[3] Eseyin A.E., Steele P.H., An overview of the applications of furfural and its derivatives, *International Journal of Advanced Chemistry*, 3, (2015), 42-47.

[4] Bomboş D., Velea S., Bomboş M., Vasilievici G., Roşca P., Hydroconversion of Furfural Derivates on Ni-Co-Mo Catalysts, *Revista de Chimie*, 10, (2016), 67-71.

[5] Villaverde M.M., Garetto T.F., Marchi A.J., Liquid-phase transfer hydrogenation of furfural to furfuryl alcohol on Cu–Mg–Al catalysts, *Catalysis Communications,* 58, (2015), 6–10.

[6] O'Driscoll Á., Leahy J.J., Curtin T., The influence of metal selection on catalyst activity for the liquid phase hydrogenation of furfural to furfuryl alcohol, *Catalisys Today*, 279(2), (2017), 194-201.

[7] Merlo A.B., Vetere V., Ramallo-Lopez J.M., Requejo F.G., Casella M.L., Liquid-phase furfural hydrogenation employing silica-supported PtSn and PtGe catalysts prepared using surface organometallic chemistry on metals techniques, *Reaction Kinetics, Mechanisms and Catalysis*, 104(2), (2011), 467-482.

[8] Rodiansono, Astuti M.D., Santos U.T., Shimazu S., Hydrogenation of biomass-derived furfural over highly dispersed-aluminium hydroxide supported Ni-Sn (3.0) alloy catalysts, *Procedia Chemistry*, 16, (2015), 531 – 539.

[9] Jiménez-Gómez C.P., Juan A.C., Márquez-Rodríguez I., Moreno-Tost R., Santamaría-González J., Mérida-Robles J., Maireles-Torre P., Gas-phase hydrogenation of furfural over Cu/CeO2catalysts, *Catalysis Today*, 279(2), (2017), 327-338.
[10] Bhogeswararao S., Srinivas D., Catalytic conversion of furfural to industrial chemicals over supported Pt and Pd catalysts, *Journal of Catalysis*, 327, (2015), 65-77.

TRANSESTERIFICATION OF VEGETABLE OILS TO BIODIESEL IN A FIXED BED CATALYST REACTOR: EXPERIMENTAL AND MODELLING

Cristian Eugen RĂDUCANU, Oana Cristina PÂRVULESCU*, Tănase DOBRE

Department of Chemical and Biochemical Engineering, Faculty of Applied Chemistry and Materials Science, University Politehnica of Bucharest, 1-7 Gh. Polizu Street, 011061, Bucharest, Romania

Abstract

Continuous transesterification of fresh sunflower oil with methanol (1/6 molar ratio) to fatty acid methyl esters (FAME) and glycerol was conducted for 1 h in a fixed-bed catalyst reactor (1.6 cm internal diameter and 55 cm height). A base catalyst was prepared by impregnation of activated carbon with a KOH solution followed by thermo-chemical activation (at 750 °C under CO_2 atmosphere) of impregnated precursor.

Fixed bed catalyst height (20, 40 cm), operating temperature (55, 65 °C), and reactant superficial velocity (0.14, 0.28 cm/s) were selected as transesterification process factors. 8 experiments were performed according to a 2^3 factorial plan. The effects of process factors on FAME yield (91.60-95.74%), glycerol yield (73.31-90.48%), and time of glycerol forming (6-23 min) were predicted. Regression equations obtained in this study could be used to evaluate the transesterification performances for factor levels within the ranges considered in the experimental runs.

Key words: biodiesel, factorial experiment, fixed bed reactor, heterogeneous catalyst, transesterification, vegetable oil

1. Introduction

Transesterification of vegetable oils or animal fats with short chain alcohol (*e.g.*, methanol, ethanol) in the presence of a catalyst (homogeneous or heterogeneous, acid, base or enzyme) leads to fatty acid alkyl esters (biodiesel) and glycerol [1-10]. Biodiesel is a clean, non-toxic, renewable, and biodegradable fuel as compared to petroleum diesel [5-9,11].

Vegetable (edible and non-edible) oils are extensively used for developing alternative fuels including biodiesel [7]. Its yield depends on various transesterification parameters, *e.g.*, catalyst type, preparation method, and quantity, reactor type, contacting mode between reactants and catalyst, oil type as

* Corresponding author; E-mail: oana.parvulescu@yahoo.com

well as its content of free fatty acids (FFA) and water, oil/methanol ratio, reaction time and temperature [1-13].

At present, most of the biodiesel is produced from edible oils and methanol in the presence of base catalysts in batch reactors [1,7,8,13].

Heterogeneous catalysts are widely used due to their advantages over homogeneous ones, *e.g.*, they can be easily separated by filtration of the reaction mixture, do not involve a neutralization step, are reusable, non-corrosive, environmentally friendly, and less sensitive to the presence of water in the oil, which can lead to a significant decrease in the process cost [1-3,5,6,9-14]. Solid catalysts involve a suitable catalytic support that can "host" chemical compounds characterized by acid or base properties needed to catalyze the conversion of oil or fat to biodiesel.

This paper aims at studying the biodiesel production from fresh sunflower oil and methanol in a fixed-bed catalyst reactor with product recirculating. A supported catalyst was prepared by impregnation of activated carbon with a KOH solution followed by thermo-chemical activation of impregnated precursor. The effects of transesterification factors (fixed-bed catalyst height, operating temperature, and reactant superficial velocity) on process responses (biodiesel yield, glycerol yield, and time of glycerol forming) were evaluated.

2. Experimental

2.1. Materials

Refined sunflower oil (ARGUS SA, Constanta) and methanol (99%, Merck, Germany) were used as reactants for biodiesel production. KOH pellets (99%, Merck, Germany) and granular activated carbon (Chemviron Carbon Corporation, Belgium) were employed for heterogeneous catalyst preparation.

2.2. Procedure

2.2.1. Catalyst preparation

Heterogeneous catalyst preparation consisted of two main stages, *i.e.*, impregnation of catalyst support and thermo-chemical activation of catalyst precursor obtained by impregnation. Activated carbon (AC) was firstly sieved, keeping only particles with a size larger than 1 mm for avoiding fine carbon powder to contaminate reaction products and thus eliminating ultrafiltration as a supplementary process stage.

Sieved AC was further impregnated with KOH as follows: it was heated at 130 ºC in a drying stove, then immersed in 2M KOH solution, kept under stirring for 2 h at 80 ºC, left for 24 h, filtered, and dried at 130 ºC.

Thermo-chemical activation of dried impregnated AC (KOH/AC) was conducted in an experimental set-up presented in Fig. 1. KOH/AC granules were packed into a ceramic furnace (1) heated by an electric resistance fed by an autotransformer (2). The heating was performed up to 750 °C at a heating rate of 15 K/min. The temperature was measured by a K thermocouple (3) connected to a voltmeter (4). CO_2 from a tank (5), whose flow rate (5 L/h) was controlled by a valve (6) and measured by a flow-meter (7), was bubbled into distilled water contained in a flask (8). The mixture of CO_2 and water vapour exiting the bubbler (8) was fed into the furnace (1) and up-flowed through the fixed bed catalyst. KOH/AC supported catalyst was thermo-chemically activated for 1 h at 750 °C.

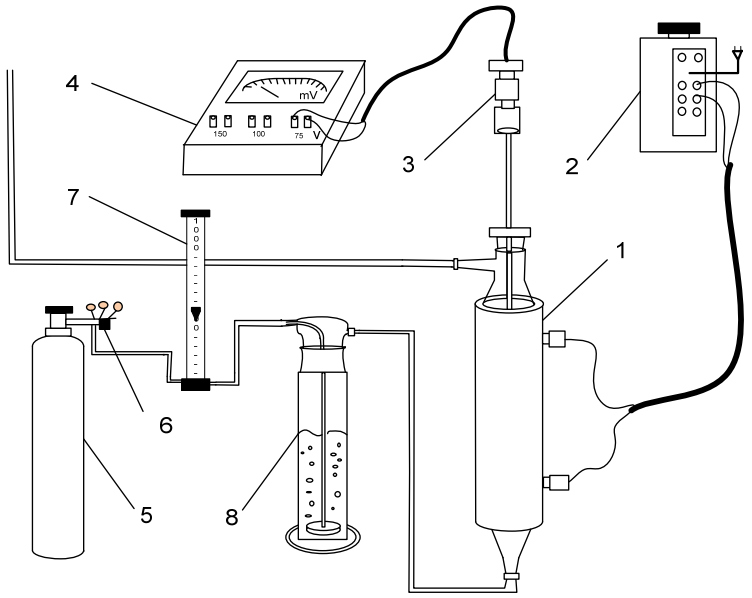

Fig. 1. Catalyst activation experimental set-up:
(1) furnace; (2) autotransformer; (3) thermocouple; (4) voltmeter; (5) CO_2 tank; (6) valve; (7) flow-meter; (8) bubbler.

2.2.2. Biodiesel synthesis

Catalytic synthesis of biodiesel from fresh sunflower oil was conducted in an experimental set-up shown in Fig. 2. Activated catalyst granules (1) were packed in a reactor (2) consisting in a water-jacketed glass column (1.6 cm internal diameter and 55 cm height). The control of reaction temperature was performed by a thermostat water bath (3) with an error of ±0.5 °C.

Fresh oil (200 g) and methanol (43.2 g) at a 1/6 oil to methanol molar ratio were fed into a four-neck round-bottom flask (4) forming two separate layers. A part of upper layer of methanol was pumped for 2 min by a dosing pump (5) into

the reactor (2), down-flowed through the fixed bed catalyst (1) producing potassium methoxide, and further was collected into the funnel (6). After that, the oil and the rest of methanol were stirred and heated using a heating magnetic stirrer (7) fitted with a contact thermometer (8) to control the temperature and a water-cooled condenser to avoid methanol losses (9). Mixed and heated reactants were pumped by the dosing pump (5) for 60 min into the catalytic reactor (2), wherein methyl esters and glycerol were obtained in the presence of potassium methoxide. Reactor effluent entered into the funnel (6) wherein two layers were separated, *i.e.*, a lower layer of glycerol and an upper one consisting mainly of reaction products and methanol. The filling of the funnel (6) determined the mixture recirculation in the mixing flask (4). The process was stopped after 60 min and the reaction mixture was left to separate for 24 h in the funnel (6).

Characteristic factors of transesterification process performed in the catalytic reactor were selected as follows: fixed bed catalyst height (h=20, 40 cm), operating temperature (t=55, 65 °C), and reactant superficial velocity (w=0.14, 0.28 cm/s). According to a 2^3 factorial plan (3 factors and 2 levels of each factors), 8 experimental runs were conducted. The effects of process factors on its responses in terms of fatty acid methyl ester yield (Y_{FAME}), glycerol yield (Y_G), and time of glycerol forming (τ_G) were evaluated. Y_{FAME} and Y_G were determined as percentages depending on theoretical values of product masses.

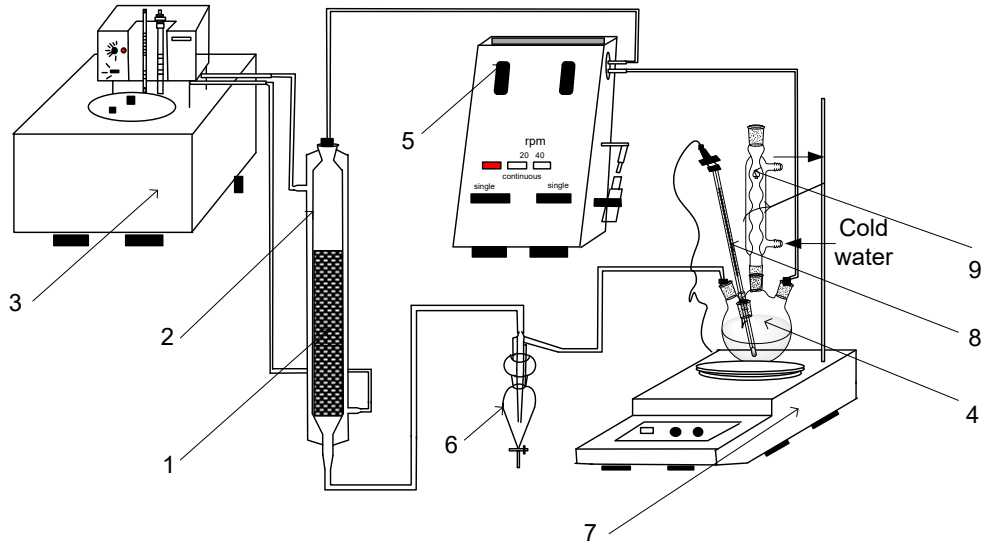

Fig. 2. Biodiesel synthesis experimental set-up:
(1) supported catalyst; (2) fixed-bed catalytic reactor; (3) thermostat water bath; (4) mixing flask; (5) micro-dosing pump; (6) separation and recirculation funnel; (7) heating magnetic stirrer; (8) contact thermometer; (9) water-cooled condenser.

3. Results and discussions

The process performances in terms of methyl ester yield (Y_{FAME}=91.60-95.74%), glycerol yield (Y_G=73.31-90.48%), and time of glycerol forming (τ_G=6-23 min) under different operating conditions are specified in Table 1.

A statistical model based on a 2^3 factorial plan was used to predict the process performances depending on its factors (h=20, 40 cm, t=55, 65 °C, and w=0.14, 0.28 cm/s). Dimensionless values of process factors are given by Eqs. (1)-(3), where h_{cp}=30 cm, t_{cp}=60 °C, and w_{cp}=0.21 cm/s are centre-points. Process factors and responses corresponding to 8 experimental runs are summarized in Table 1 (no. 1-8).

Table 1

Experimentation matrix for 2^3 factorial experiment

No.	h (cm)	t (°C)	w (cm/s)	x_1	x_2	x_3	Y_{FAME} (%)	Y_G (%)	τ_G (min)
1	20	55	0.14	-1	-1	-1	92.40	84.97	21
2	20	55	0.28	-1	-1	1	95.02	78.97	23
3	20	65	0.14	-1	1	-1	93.57	78.73	18
4	20	65	0.28	-1	1	1	91.60	76.36	20
5	40	55	0.14	1	-1	-1	95.41	87.14	9
6	40	55	0.28	1	-1	1	91.88	90.48	6
7	40	65	0.14	1	1	-1	93.56	85.31	10
8	40	65	0.28	1	1	1	95.74	73.31	7
9	30	60	0.21	0	0	0	93.73	82.55	15
10	30	60	0.21	0	0	0	93.68	83.83	14
11	30	60	0.21	0	0	0	93.61	80.84	14
12	30	60	0.21	0	0	0	93.63	81.48	15

$$x_1 = \frac{h-30}{10} \quad (1)$$

$$x_2 = \frac{t-60}{5} \quad (2)$$

$$x_3 = \frac{w-0.21}{0.07} \quad (3)$$

Regression coefficients of statistical model described by Eq. (4), *i.e.*, β_{ij} (i=1..N=8, j=1..3), which are specified in Table 2, were determined by processing the data summarized in Table 1 (no. 1-8) according to characteristic procedure of a 2^3 factorial experiment.

$$y_j = \beta_{1j} + \beta_{2j}x_1 + \beta_{3j}x_2 + \beta_{4j}x_3 + \beta_{5j}x_1x_2 + \beta_{6j}x_1x_3 + \beta_{7j}x_2x_3 + \beta_{8j}x_1x_2x_3 \quad (4)$$

Table 2

Significance of regression coefficients of Eq. (4)

	i	1	2	3	4	5	6	7	8
j=1	β_{i1} (%)	**93.65**	**0.5**	-0.03	**-0.088**	**0.533**	**-0.25**	**0.14**	**1.287**
	$y_{1,mn,cp}$ (%)	93.66							
	$\sigma_{rp,1}$ (%)	0.052							
	$\sigma_{\beta,1}$ (%)	0.018							
	t_{i1}	**5089**	**27.17**	1.630	**4.755**	**28.94**	**13.59**	**7.608**	**69.97**
	t_{i1}-3.176	**>0**	**>0**	<0	**>0**	**>0**	**>0**	**>0**	**>0**
j=2	β_{i2} (%)	**81.91**	**2.151**	**-3.481**	**-2.129**	-1.269	-0.036	-1.464	**-2.371**
	$y_{2,mn,cp}$ (%)	82.18							
	$\sigma_{rp,2}$ (%)	1.31							
	$\sigma_{\beta,2}$ (%)	0.463							
	t_{i2}	**176.8**	**4.643**	**7.514**	**4.595**	2.739	0.078	3.159	**5.118**
	t_{i2}-3.176	**>0**	**>0**	**>0**	**>0**	<0	<0	<0	**>0**
j=3	β_{i3}	**14.25**	**-6.25**	-0.50	-0.25	**1.00**	**-1.25**	0	0
	$y_{3,mn,cp}$ (min)	14.5							
	$\sigma_{rp,3}$ (min)	0.577							
	$\sigma_{\beta,3}$ (min)	0.204							
	t_{i3}	**69.81**	**30.62**	2.45	1.225	**4.899**	**6.124**	0	0
	t_{i3}-3.176	**>0**	**>0**	<0	<0	**>0**	**>0**	=0	=0

In order to determine the significance of regression coefficients using the Student's test [15-17], 4 centre-point runs (N_{cp}=4) were performed (no. 9-12 in Table 1). Characteristic parameters of centre-point runs, *i.e.*, mean value of response ($y_{j,mn,cp}$), reproducibility standard deviation ($\sigma_{rp,j}$), and number of degrees of freedom (υ_1), as well as standard deviation associated to regression coefficients ($\sigma_{\beta,j}$) and values of Student's random variable (t_{ij}), given by Eqs. (5)-(9), are presented in Table 2.

$$y_{j,mn,cp} = \frac{\sum_{k=1}^{N_{cp}} y_{jk,cp}}{N_{cp}} \quad (5)$$

$$\sigma_{rp,j} = \sqrt{\frac{\sum_{k=1}^{N_{cp}} \left(y_{jk,cp} - y_{j,mn,cp}\right)^2}{\upsilon_1}} \quad (6)$$

$$\upsilon_1 = N_{cp} - 1 = 3 \quad (7)$$

$$\sigma_{\beta,j} = \frac{\sigma_{rp,j}}{\sqrt{N}} \quad (8)$$

$$t_{ij} = \frac{|\beta_{ij}|}{\sigma_{\beta,j}} \quad (9)$$

Regression coefficients satisfying the condition $t_{ij} - t_{\alpha,\upsilon_1} > 0$ were considered as significant, where $t_{\alpha,\upsilon_1} = 3.176$ represents the theoretical value of Student's variable corresponding to a significance level (α) of 0.05 and υ_1=3 [15-17]. Considering only significant coefficients (bold characters in Table 2), the statistical model described by Eq. (4) becomes:

$$y_1 = Y_{FAME} = 93.65 + 0.5x_1 - 0.088x_3 + 0.533x_1x_2 - 0.25x_1x_3 + 0.14x_2x_3 + 1.287x_1x_2x_3 \quad (10)$$

$$y_2 = Y_G = 81.91 + 2.151x_1 - 3.481x_2 - 2.129x_3 - 2.371x_1x_2x_3 \quad (11)$$

$$y_3 = \tau_G = 14.25 - 6.25x_1 + x_1x_2 - 1.25x_1x_3 \quad (12)$$

Referring to the effect of process factors, *i.e.*, fixed bed height (x_1), operating temperature (x_2), and reactant superficial velocity (x_3), on the process responses, regression equations (10)-(12) indicate the following issues: (i) Y_{FAME} increases with x_1, x_1x_2, x_2x_3, and $x_1x_2x_3$, as well as it decreases with an increase in x_3 and x_1x_3; (ii) Y_G increases with x_1 and decreases with an increase in x_2, x_3, and $x_1x_2x_3$; (iii) x_1 and x_1x_3 interaction have a negative effect on τ_G, whereas x_1x_2 interaction has a positive effect. Statistical model described by Eqs. (10)-(12) could be applied to estimate the performances of transesterification process for factor levels within the ranges considered in the statistical analysis, *i.e.*, h=20-40 cm, t=55-65 °C, and w=0.14-0.28 cm/s.

4. Conclusions

Transesterification of fresh sunflower oil with methanol to FAME and glycerol was continuously performed in a fixed-bed catalyst reactor. A supported catalyst was prepared by impregnation of activated carbon (AC) with a 2M KOH solution followed by thermo-chemical activation (at 750 °C under CO_2 atmosphere) of impregnated precursor. Activated catalyst (KOH/AC) was packed in a water-jacketed glass column (1.6 cm internal diameter and 55 cm height) and tested in the transesterification.

Fresh oil and methanol (1/6 molar ratio) were mixed, heated, and further passed (for 1 h) through the fixed-bed catalyst. Reactor effluent, consisting mainly of FAME, glycerol, and unreacted methanol, was recirculated in the process.

The effects of process factors, *i.e.*, fixed bed catalyst height (h=20, 40 cm), operating temperature (t=55, 65 °C), and reactant superficial velocity (w=0.14, 0.28 cm/s), on its responses in terms of FAME yield, glycerol yield, and time of

glycerol forming were evaluated using a 2^3 factorial plan. FAME yield (91.60-95.74%) increased with *h*, *ht*, *tw*, and *htw*, whereas it decreased with an increase in *w* and *hw* interaction. Glycerol yield (73.31-90.48%) increased with *h* and decreased with an increase in *t*, *w*, and *htw* interaction. The time of glycerol forming (6-23 min) was negatively influenced by *h* and *hw* interaction, whereas *ht* interaction had a positive effect on it. Regression equations obtained by processing the experimental data could be applied to predict the transesterification performances for factor levels within the ranges considered in the study.

Acknowledgements

Financial support from Romanian Society of Chemical Engineering for attending the 20th RICCCE Conference is gratefully acknowledged by Cristian Eugen Răducanu.

REFERENCES

[1] Aziz M.A.A., Puad K., Triwahyono S., Jalil A.A., Khayoon M.S., Atabani A.E., Ramli Z., Majid Z.A., Prasetyoko D., Hartanto D., Transesterification of croton *megalocarpus* oil to biodiesel over WO_3 supported on silica mesoporous-macroparticles catalyst, *Chemical Engineering Journal*, 316, (2017), 882-892.

[2] Baskar G., Gurugulladevi A., Nishanthini T., Aiswarya R., Tamilarasan K., Optimization and kinetics of biodiesel production from Mahua oil using manganese doped zinc oxide nanocatalyst, *Renewable Energy*, 103, (2017), 641-646.

[3] Fadhil A.B., Aziz A.M., Tamer M.H.A., Biodiesel production from *Silybum marianum* L. seed oil with high FFA content using sulfonated carbon catalyst for esterification and base catalyst for transesterification, *Energy Conversion and Management*, 108, (2016), 255-265.

[4] Ghadge S.V., Raheman H., Process optimization for biodiesel production from mahua (*Madhuca indica*) oil using response surface methodology, *Bioresource Technology*, 97, (2006), 379-384.

[5] Maneerung T., Kawi S., Dai Y., Wang C.H., Sustainable biodiesel production via transesterification of waste cooking oil by using CaO catalysts prepared from chicken manure, *Energy Conversion and Management*, 123, (2016), 487-497.

[6] Martinez S.L., Romero R., Natividad R., Gonzalez J., Optimization of biodiesel production from sunflower oil by transesterification using Na_2O/NaX and methanol, *Catalysis Today*, 220-222, (2014), 12-20.

[7] Meher L.C., Sagar D.V., Naik S.N., Technical aspects of biodiesel production by transesterification-a review, *Renewable and Sustainable Energy Reviews*, 10(3), (2006), 248-268.

[8] Muthukumaran C., Praniesh R., Navamani P., Swathi R., Sharmila G., Kumar N.M., Process optimization and kinetic modeling of biodiesel production using non-edible *Madhuca indica* oil, *Fuel*, 195, (2017), 217-225.

[9] Vicente G., Coteron A., Martinez M., Aracil J., Application of the factorial design of experiments and response surface methodology to optimize biodiesel production, *Industrial Crops and Products*, 8, (1998), 29-35.

[10] Yadav M., Singh V., Sharma Y.C., Methyl transesterification of waste cooking oil using a laboratory synthesized reusable heterogeneous base catalyst: Process optimization and homogeneity study of catalyst, *Energy Conversion and Management*, 148, (2017), 1438-1452.

[11] Lee S.L., Wong Y.C., Tan Y.P., Yew S.Y., Transesterification of palm oil to biodiesel by using waste obtuse horn shell-derived CaO catalyst, *Energy Conversion and Management*, 93, (2015), 282-288.
[12] Feng Y., Zang A., Li J., He L., A continuous process for biodiesel production in a fixed bed reactor packed with cation-exchange resin as heterogeneous catalyst, *Bioresource Technology*, 102, (2011), 3607-3609.
[13] Jamil F., Al-Muhatseb A.H., Myint M.T.Z., Al-Hinai M., Al-Haj L., Baawain M., Al-Abri M., Kumar G., Atabani A.E., Biodiesel production by valorizing waste *Phoenix dactylifera* L. Kernel oil in the presence of synthesized heterogeneous metallic oxide catalyst (Mn/MgO-ZrO_2), *Energy Conversion and Managemen*t, 155, (2018), 128-137.
[14] Mohamad M., Ngadi N., Wong S.L., Jusoh M., Yahya N.Y., Prediction of biodiesel yield during transesterification process using response surface methodology, *Fuel*, 190, (2017), 104-112.
[15] Cioroiu D.R., Pârvulescu O.C., Koncsag C.I., Dobre T., Răducanu C., Rheological characterization of algal suspensions for bioethanol processing, *Rev. Chim. (Bucharest)*, 68(10), (2017), 2311-2316.
[16] Ion V.A., Pârvulescu O.C., Dobre T., Volatile organic compounds adsorption onto neat and hybrid cellulose, *Applied Surface Science*, 335, 137-146, 2015.
[17] Orbeci C., Pârvulescu O.C., Acceleanu E., Dobre T., Effects of process factors on carbon dioxide reforming of methane over Ni/SBA-15 catalyst, *Rev. Chim. (Bucharest)*, 68(10), (2017), 2325-2328.

EXTRACTION OF BIOMOLECULES FROM A BROWN SEAWEED FROM THE ROMANIAN BLACK SEA SHORE (*CYSTOSEIRA BARBATA*)

Bogdan TRICĂ[1, 2,*], Cédric DELATTRE[3], Guillaume PIERRE[3], Alina-Violeta URSU[3], Christine GARDARIN[3], Philippe MICHAUD[3], Gholamreza DJELVEH[3], Tănase DOBRE[1]

[1]Department of Chemical and Biochemical Engineering, Faculty of Applied Chemistry and Materials Science, University Politehnica of Bucharest, 1-7 Gh. Polizu Street, 011061, Bucharest, Romania
[2]National Institute for Research & Development in Chemistry and Petrochemistry (ICECHIM), 202 Splaiul Independentei, 060021, Bucharest, Romania
[3]Université Clermont Auvergne, CNRS, Sigma Clermont, Institut Pascal, BP 10448, F-63000, Clermont-Ferrand, France

Abstract

Cystoseira barbata, the main brown seaweed species at the Romanian Black Sea shore, contains a number of valuable biomolecules. We focus on the extraction of alginate, fucans and phlorotannins. Alginate is already a natural biomolecule with a well-established market,which is supposed to grow in the near future, as a thickening and gelling agent. Furthermore, fucans have recently been shown to be biologically active. Phlorotannins are also worth investigating as they are polymers of phloroglucinol, a phenolic compound which has a good antioxidant activity. In this paper, alginate, fucans and phlorotannins are extracted in a sequential manner from Cystoseira barbata. Identification and quantification of the biomolecules is carried out by specific methods. The purpose of this paper is to prove the concept of biorefinery applied for a brown seaweed species at the Romanian Black Sea shore.

Key words: *CystoseiraBarbata*, alginate, fucans, phlorotannins

1. Introduction

Seaweed is a source of valuable products with unique properties. In Romania it remains untapped as it is removed from beaches as a waste when it

* Corresponding author: Email address:trica.bogdan@gmail.com

accumulates. All three types of seaweed or phyla are represented on the Romanian Black Sea shore: Chlorophyta (green), Rhodophyta (red) and Phaeophyta (brown) [1].Biomass produced at the Romanian Black Sea shore consists mainly of red and green seaweed with values reported between 5 and 25 kg/m^2[2]. The only brown seaweed (kelp) species which still exists is *Cystoseirabarbata*. Even if now biomass is at a low level, values of 4300 t were reported in 1972. Nowadays, the collapse of the *C. barbata* population is largely related to climatic and anthropic factors [1].

Brown seaweed is a well-known source of valuable biomolecules which includes alginate (an acidic polysaccharide), fucoxanthin (a carotenoid pigment) and fucans (sulfated polysaccharides). Apart from these classes, we also find phlorotannins which are polyphenolic compounds with a high solubility in water[3,4]. All of these compounds have been proven to be useful either for their rheological properties (alginate) or for their various biological activities (antioxidant, cytostatic, antiviral etc.) [5-7].

Alginate is one of the most biomaterials with a whole range of applications in food industry and even n textile industry[8]. It is a natural copolymer formed from two uronic acids, β-D-mannuronic acid (M) and α-L-guluronic acid (G) which are linked β-(1,4)[9,10].Together with other water-soluble polysaccharides extracted from seaweed, it formsthe group which is generically called phycocolloids[11]. These biomolecules possess a wide range of possible applications in the food industry and cosmetics, especially as gelling and thickening agents[12].Other important phycocolloids are agar and carrageenan (red algae), fucans (sulfated polysaccharides from brown algae) and ulvans (sulfated polysaccharides from green algae)[11]. Thegross market value for phycocolloids (which also includes alginate) has been estimated at 1 billion US$ per year with an annual global production of 100 thousand tons and it is expected to grow [13].Other uses applied for seaweed include raw material for biofuel production[14-16], polysaccharide based supercapacitors[17] and others.

The main goal of our work is to show that several valuable biomolecules can be extracted in series, following an extraction scheme which resembles that of a biorefinery concept. At this point, we are only focusing on polyphenols, fucans and alginate. Other compounds such as pigments and proteins could also prove interesting of our purpose. Apart from this, we expect that the fibers which are left after the extraction series to be rich in fermentable cellulose which could valorized as biogas or bioethanol [18]. Suchextraction models applied to seaweed have been proposed in literature before[19] and follow a bio-refineryconcept.

2. Materials and Methods

Raw material

C. barbata seaweed were collected from the Black Sea in the city of Mangalia (Latitude: N 43° 49' 9.9048"; Longitude: E 28° 35' 22.5655"). They were then washed with tap water to remove seawater and other impurities and dried in the sun. The resulted dried material was then milled and sieved. *C.barbata*algal powder with particles smaller than 500 µm was used.

Extraction

A purified form of alginate was obtained by following a procedure previously presented in literature [20,21]. This procedure is depicted in Fig. 1.

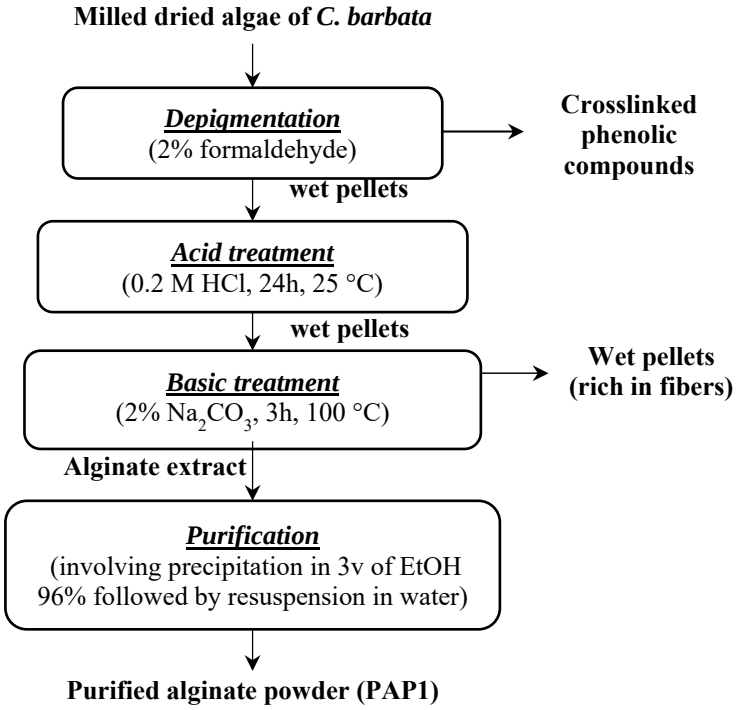

Fig. 1. Alginate extraction (method 1)

25 g of milled dried algae were depigmented with 800 mL of 2% formaldehyde under stirring for 24h at room temperature. The pellets were then removed and washed with distilled water prior to adding them to 800 mL of 0.2 M HCl. This treatment was carried on for 24h, under stirring and at room temperature. The wet pellets were removed and washed with distilled water. Alginate was then extracted by treating the wet pellets with a solution of 2% Na_2CO_3 for 3 hours at 100 °C. The alginate solution was separated from the wet

pellets by filtration (Whitman paper, 25 μm). It was then precipitated with 3 volumes of cooled ethanol (96%). The dried alginate was further purified by dissolution in demineralized water followed by precipitation with another 3 volumes of ethanol. This step was repeated until the pH approached neutral values while the salt equivalent, measured by conductimetry, had a value lower than 1 g/L (Fig. 2). The dried product was further purified by precipitation in cooled acetone followed by dissolution in MilliQ water.

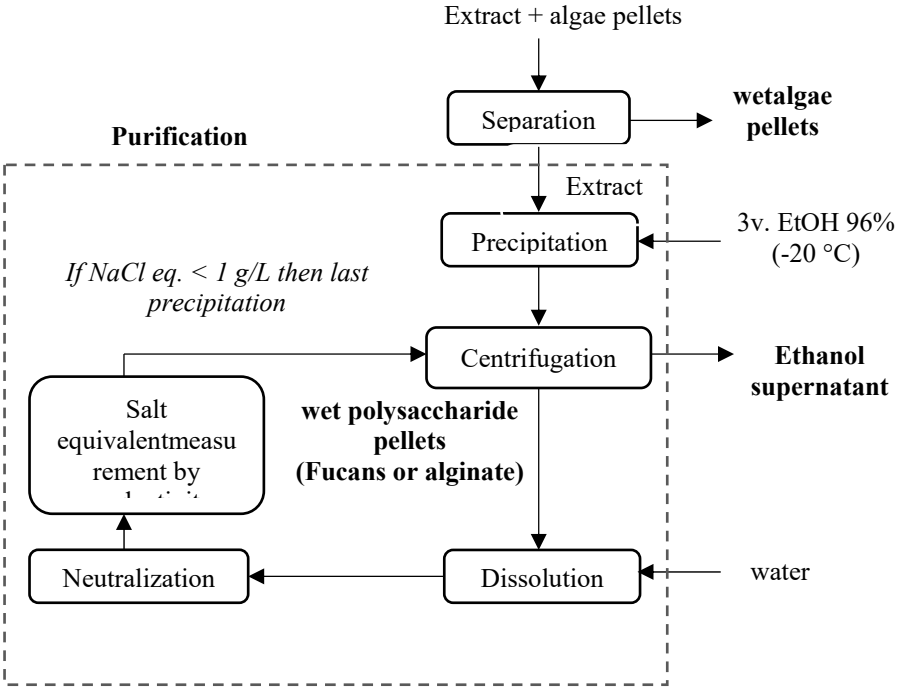

Fig. 2. Purification of polysaccharides

Method 2was adapted from literature [22] and aimed at extracting several groups of biomolecules. Pigments are extracted in 70 % ethanol for 24 h. The pellets are then sequentially extracted under stirring twice in 0.1 M HCl (2 h, 60 °C) to recover the fucans. The pellets are separated by filtration and alginate is extracted with 3 % Na_2CO_3 (2 h, 60 °C) in two steps. Phlorotannins are then removed by washing the wet pellets 4 times with distilled water. The scheme for this extraction scheme is presented in Fig. 3.

In both methods, purification of the polysaccharides followed the scheme presented in Fig. 2 which involves repetitive precipitation in ethanol aimed at removing salt and neutralization. At least after the first precipitation, the solution needs to be neutralized.

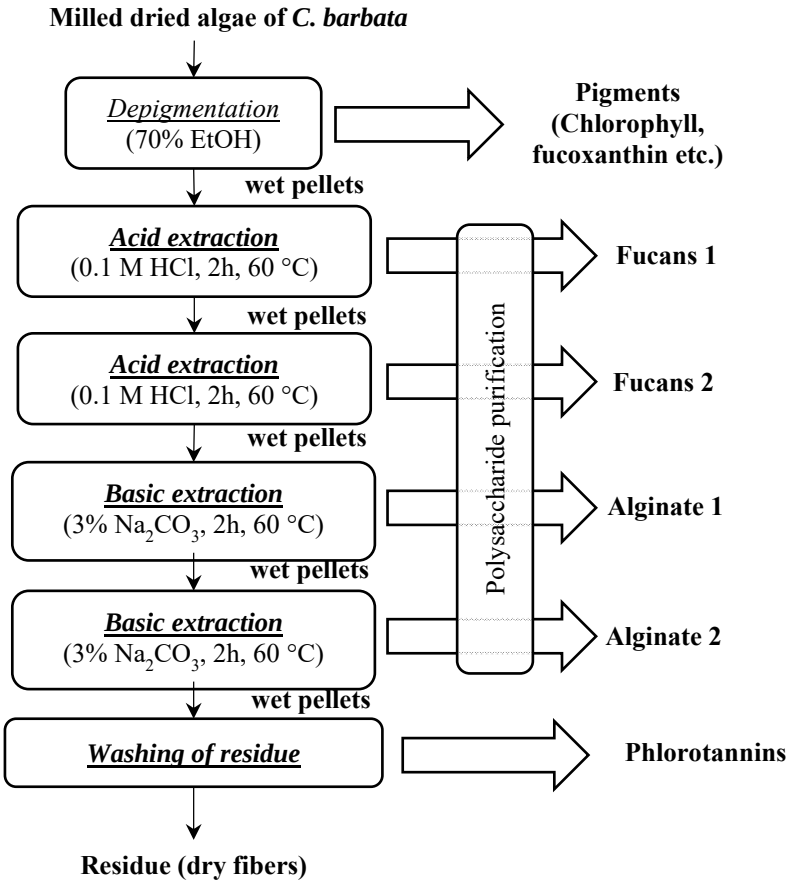

Fig. 3. Sequential extraction scheme (method 2)

Total phenolic content

The method applied for determining the total phenolic content was adapted from literature[23]. 0.5 mL of sample was added to 10 mL of MilliQ water. 0.5 mL of Folin-Ciocalteu reagent is added. 1 mL of Na_2CO_3 (saturated solution) is then added. The sample must be vortexed vigorously. Immediately after, the sample must be placed in the dark and kept there for 1 hour during which it should acquire a blue color. The absorbance at 750 nm is measured. The total phenolic content is expressed as grams of phloroglucinol equivalents (PGE, g/L).

Neutral and Acid Sugars

A colorimetric method is used which also takes into consideration interferences between neutral and acid sugars [24].

Some solutions are prepared beforehand: a resorcinol (6 mg/mL) in MilliQ water, sulfuric acid solution (80%), borax in 97% sulfuric acid (0.12 M) and a

solution of 100 mg of m-HBP (m-hydroxybiphenyl) in 1 mL of DMSO (dimethyl sulfoxide).

Neutral sugars assay involves mixing 200 µL of sample, 200 µL of resorcinol solution and 1 mL of 80% sulfuric acid in a screw-cap test tube which is then placed at 90 °C for 30 min. After this, it is left for 30 min in the dark to cool. The yellowish coloration is measured at 450 nm after diluting with 1.4 mL of MilliQ water. Acid sugars assaystarts by adding 200 µL and 1 mL of borax solution to a screw-cap test tube. They are then left for 1h at 90 °C before adding 200 µL of m-HBP. Immediately, the tube is placed for another 2 min at 90 °C. The pink hue of the mixture is then measured at 520 nm.

Values are expressed as glucuronic acid eq. (g/L) for acid sugar content (AcS) and glucose eq. (g/L) for neutral sugar content (NeS). The values are computedusing equations (1) and (2) where α is the specific absorbance of glucose in the neutral sugars assay, β is the specific absorbance of glucuronic acid in the neutral sugars assay and β' is the specific absorbance of glucuronic acid in the acid sugars assay.

$$[AcS] = \frac{Abs_{mHBP}}{\beta'} \tag{1}$$

$$[NeS] = \frac{Abs_{res} - \beta \cdot [AcS]}{\alpha} \tag{2}$$

Dry matter

Dry matter content (DM) was determined by drying a known mass of sample in an aerated oven at 110 °C for 24h.

HPAEC-PAD analysis

Fucose and mannuronic acid content was determined by High Performance Anion Exchange Chromatography with Pulsed Amperometric Detection (HPAEC-PAD) after complete hydrolysis [20,25] of 10 mg of polysaccharide powder in 4.5 mL of 90% formic acid for 6 hours at 100 °C. The samples were then passed through the Dionex ICS-3000 system using an eluent containing 100 mM of NaOH and 100 mM of NaOAc inMilliQ water during 1h at a rate of 1 mL/min [20].

3. Results and Discussion

Mass balance

Table 1 presents the mass balance for dried matter (g), PGE (mg), NeS (g) and AcS (g). It also presents the yields obtained at the end. Thus, we obtain 3.9 g of purified alginate which represents 15.7 % from the initial mass of *C. barbata*

powder (<500 μm). Alginate extracted in the second basic treatment could not be recovered. This suggests that one basic extraction is enough to recover most of the alginate [22]. 0.4 % and 0.6 % of the initial mass is recovered as fucans powder in the first and in the second acidic steps. Phlorotannins are mostly recovered at the end when the insoluble algal mass is washed with water. The PGE, NeS and AcS content of the ethanol supernatants is also expressed. This are obtained as described in Fig. 2 regarding the purification of polysaccharides by ethanol precipitation (1 volume of extract + 3 volumes of ethanol 96 %).

Table 1

Mass balance for extraction of biomolecules (method 2)

Name	Dry weight (g)	Dry weight% /25g	PGE (mg)	NeS (g)	AcS (g)
EtOH 70% extract	1.63	6.5	0.77	0.102	0.037
Acid ethanolsupernatant 1	2.85	11.4	58.37	0.714	0.020
fucans 1 powder (0.1032 g)	***0.10***	***0.4***	3.85	0.043	0.030
Acid ethanolsupernatant 2	2.42	9.7	14.89	0.227	0.020
fucans 2 powder (0.143 g)	***0.14***	***0.6***	5.08	0.029	0.040
Basic ethanolsupernatant 1	2.00	8.0	22.94	0.049	0.009
alginate 1 powder (3.9249 g)	***3.92***	***15.7***	1.51	1.006	2.634
Basic ethanolsupernatant 2	0.96	3.8	14.41	0.029	0.003
alginate 2 powder	N.D.	N.D.	N.D.	N.D.	N.D.
Washing water	2.36	9.4	***415***	0.164	0.119
Dry fibers (5.1 g)	**-**	**20.4%**			
TOTAL	**21.5**		**537**	**2.365**	**2.912**
percentage of 25 g	**86%**		**2%**	**9%**	**12%**

Phlorotannins

Generally, an important contamination in alginate products arises from pigments and polyphenolic compounds (phlorotannins). Since method 1 (Fig. 1) is aimed at extracting alginate, polyphenols are removed in the first step by crosslinking them with 2% formaldehyde. This ensures that they remain insoluble during the subsequent steps, especially during the basic extraction of alginate.

In the case of method 2, phlorotannins are desirable. To extract the pigments (chlorophyll, fucoxanthin), ethanol 70 % (vol.)[26]. This concentration is also equivalent to the one in the precipitation phase where 1 volume of polysaccharide extract is mixed with 3 volumes of ethanol 96% in order to precipitate the polysaccharides[20]. During the depigmentation step in method 2, polysaccharides are not extracted.

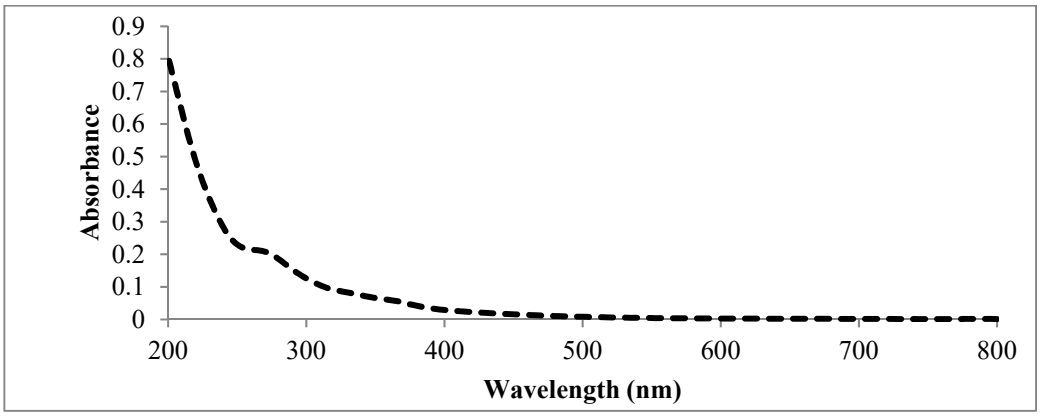

Fig. 4. UV spectra for the washing water rich in phlorotannins

We observe from Table 1 that 77% of the phlorotanninsextracted during method 2 are solubilized in the stream obtained by washing the wet pellets which left after the basic extraction of alginate (Fig. 3). They are identified by the polyphenols assay described in section 2 and by matching its UV spectra (Fig. 4)with one found in literature [3].

Polysaccharides

We identify and quantify the peaks corresponding to fucose (3.02 min - Fuc) and mannuronic acid (23.08 min - ManA) which can be seen in 5 and **Error! Reference source not found.** (totally hydrolyzed alginate obtained via method 1 and method 2). We estimate the concentration of guluronic acid from the ratio of its specific peak (22.7 min - GulA) to that of mannuronic acid assuming that its retention time is close to that of mannuronic acid [27].

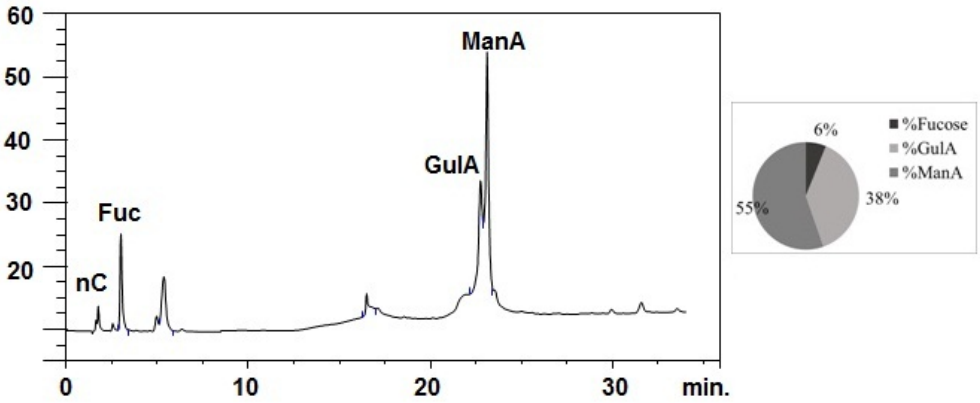

Fig. 5. HPAEC chromatogram for totally hydrolyzed alginate (Method 1)

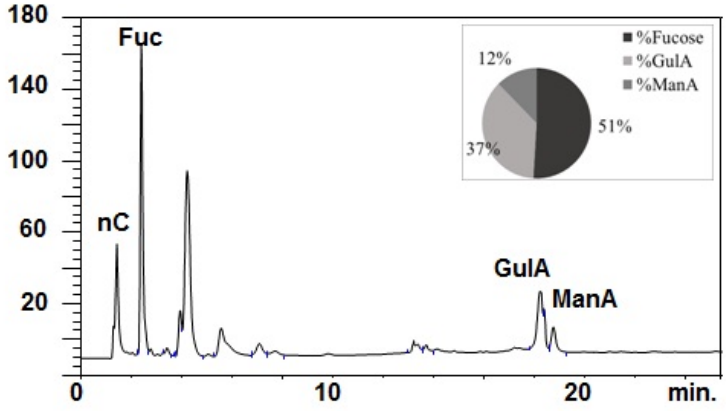

Fig. 6. HPAEC chromatogram for totally hydrolyzedfucans (Method 2)

We notice that in the alginate obtained by method 1 (Fig. 5)we have a low impurity of 6% fucose, related more likely to fucans which were not extracted in the acidic step. However, in the fucans powder purified from the first acidic extract, we observe that there is a large uronic acids impurity which could be due to the partial hydrolysis of alginate which could arise in the acidic medium.

An important characteristic of alginate is the ratio between mannuronate and guluronate (M/G). It is well known that this feature influences the thickening and gelling properties of the alginate [28,29]. By looking at the chromatogram in Fig. 5 we estimate that the M/G value for *C. barbata* recovered from the Romanian Black Sea shore is 1.44. This value needs to be confirmed by NMR [30].

4. Conclusions

Two extraction methods were adapted from literature in order to extract alginate, fucans and phlorotannins from *Cystoseirabarbata* seaweed recovered from the Black Sea.

The first extraction method yielded a purified alginate for which we determined an M/G ratio of 1.44. The hydrolyzed product fed to the HPAEC-PAD instrument contained a 6% fucose impurity associated to fucans.

The second extraction methodwasapplied for the sequential extraction of phlorotannins,fucansand alginate. Using this method, 1%of the initial mass of *C. barbata* is extracted as fucans, while 15.7% as alginate.Most phlorotannins (77% of PGE (mg) found in all streams) are recovered by washing the insoluble material following the basic extraction of alginate. In total, 537 mg of phlorotannins (measured in phloroglucinol equivalents) are extracted from 25 g of dried milled seaweed.

For future studies, our preoccupation will be to test various purification methods and propose new applications for the extracted alginate, fucans and phlorotannins.

Acknowledgements

Financial support from Romanian Society of Chemical Engineering for attending the 20th RICCCE Conference is gratefully acknowledged by Bogdan Trică.

REFERENCES

[1] Marin, A.O.; Timofte, F. Atlasul macrofitelor de la litoralul romanesc. Constanta, (2011).
[2] Sava, D.; Samargiu, M.D.; Paraschiv, G.M. Posibilities of valorification of main macrophytic algal biomass from the Romanian Black Sea shore. *Research Journal of Agricultural Science,*39, (2007), 469-472.
[3] Sathya, R.; Kanaga, N.; Sankar, P.; Jeeva, S. Antioxidant properties of phlorotannins from brown seaweed Cystoseira Trinodis (Forsskål) C. Agardh. *Arabian Journal of Chemistry,*10, (2017), S2608-S2614.
[4] Ragan, M.A.; Glombitza, K.W. Phlorotannins, brown algal polyphenols. *Program. Phycol. Res.,*4, (1986), 129-241.
[5] Vo, T.-S.; Kim, S.-K. Fucoidans as a natural bioactive ingredient for functional foods. *Journal of Functional Foods,*5, (2013), 16-27.
[6] Li, Y.-X.; Wijesekara, I.; Li, Y.; Kim, S.-K. Phlorotannins as bioactive agents from brown algae. *Process Biochemistry* 46, (2011), 2219-2224.
[7] Athukorala, Y.; Ahn, G.N.; Jee, Y.-H.; Kim, G.-Y.; Kim, S.-H.; Ha, J.-H.; Kang, J.-S.; Lee, K.-W.; Jeon, Y.-J. Antiproliferative activity of sulfated polysaccharide isolated from an enzymatic digest of Ecklonia cava on the u-937 cell line. *Journal of applied phycology,*21, (2009), 307-314.
[8] Milledge, J.J.; Nielsen, B.V.; Bailey, D. High-value products from macroalgae: The potential uses of the invasive brown seaweed, Sargassum muticum. *Reviews in Environmental Science and Bio/Technology,*15, (2016), 67-88.
[9] Rioux, L.E.; Turgeon, S.L.; Beaulieu, M. Characterization of polysaccharides extracted from brown seaweeds. *Carbohydrate Polymers,*69, (2007), 530-537.
[10] Rupérez, P.; Gómez-Ordóñez, E.; Jiménez-Escrig, A. Bioactive Compounds from Marine Foods: Plant and Animal Sources, Chapter 11. *Biological activity of algal sulfated and nonsulfated polysaccharides*, 219-247, John Wiley & Sons, Ltd., 2013.
[11] Gonçalves, A.G.; Ducatti, D.R.B.; Duarte, M.E.R.; Noseda, M.D. 5. Chemistry and biotechnology of phycocolloids. *Cellulose and Other Naturally Occurring Polymers* (2014), 41-47.
[12] Kadam, S.U.; Álvarez, C.; Tiwari, B.K.; O'Donnell, C.P. Extraction of biomolecules from seaweeds,(2015), 243-269.
[13] Pangestuti, R.; Kim, S.K. An overview of phycocolloids: The principal commercial seaweed extracts. *Marine Algae Extracts: Processes, Products, and Applications,*(2015), 319-330.
[14] Vivekanand, V.; Eijsink, V.G.H.; Horn, S.J. Biogas production from the brown seaweed Saccharina latissima: Thermal pretreatment and codigestion with wheat straw. *Journal of Applied Phycology,*24,(2012), 1295-1301.

[15] Kraan, S. Mass-cultivation of carbohydrate rich macroalgae, a possible solution for sustainable biofuel production. *Mitigation and Adaptation Strategies for Global Change,*18,(2013), 27-46.
[16] Wei, N.; Quarterman, J.; Jin, Y.-S. Marine macroalgae: An untapped resource for producing fuels and chemicals. *Trends in biotechnology* (2013), *31*, 70-77.
[17] Liew, S.Y.; Thielemans, W.; Freunberger, S.; Spirk, S. Polysaccharides in supercapacitors. In *Polysaccharide based supercapacitors*, Springer Verlag: 15-53, 2017.
[18] Yanagisawa, M.; Kawai, S.; Murata, K. Strategies for the production of high concentrations of bioethanol from seaweeds: Production of high concentrations of bioethanol from seaweeds. *Bioengineered,*4,(2013), 224-235.
[19] Balina, K.; Romagnoli, F.; Blumberga, D. Seaweed biorefinery concept for sustainable use of marine resources. *Energy Procedia,*128,(2017), 504-511.
[20] Fenoradosoa, T.A.; Ali, G.; Delattre, C.; Laroche, C.; Petit, E.; Wadouachi, A.; Michaud, P. Extraction and characterization of an alginate from the brown seaweed Sargassum turbinarioides grunow. *Journal of applied phycology,*22,(2010), 131-137.
[21] Calumpong, H.P.; Maypa, A.P.; Magbanua, M. Population and alginate yield and quality assessment of four Sargassum species in negros island, central philippines. *Hydrobiologia 398*,(1999), 211-215.
[22] Sellimi, S.; Kadri, N.; Barragan-Montero, V.; Laouer, H.; Hajji, M.; Nasri, M. Fucans from a tunisian brown seaweed Cystoseira barbata: Structural characteristics and antioxidant activity. *International Journal of Biological Macromolecules,*66, (2014), 281-288.
[23] Singleton, V.L.; Orthofer, R.; Lamuela-Raventós, R.M. Analysis of total phenols and other oxidation substrates and antioxidants by means of Folin-Ciocalteu reagent. *Methods in enzymology,*299, (1999), 152-178.
[24] Spick, G.; Montreuil, J. 2 causes of error in colorimetric determinations of total neutral sugar. *Bulletin de la Société de Chimie Biologique,*46, (1964), 739-749.
[25] Chandıa, N.P.; Matsuhiro, B.; Vásquez, A.E. Alginic acids in Lessonia trabeculata: Characterization by formic acid hydrolysis and FT-IR spectroscopy. *Carbohydrate Polymers,*46,(2001), 81-87.
[26] Lichtenthaler, H.K.; Wellburn, A.R. Determinations of total carotenoids and chlorophyllsaandbof leaf extracts in different solvents. *Biochemical Society Transactions* 11, (1983), 591-592.
[27] Boucelkha, A.; Petit, E.; Elboutachfaiti, R.; Molinié, R.; Amari, S.; Yahaoui, R.Z. Production of guluronate oligosaccharide of alginate from brown algae Stypocaulon scoparium using an alginate lyase. *Journal of Applied Phycology,*29, (2017), 509-519.
[28] Lee, K.Y.; Mooney, D.J. Alginate: Properties and biomedical applications. *Progress in Polymer Science,*37, (2012), 106-126.
[29] George, M.; Abraham, T.E. Polyionic hydrocolloids for the intestinal delivery of protein drugs: Alginate and chitosan - a review. *Journal of Controlled Release,*114, (2006), 1-14.
[30] Lu, J.; Yang, H.; Hao, J.; Wu, C.; Liu, L.; Xu, N.; Linhardt, R.J.; Zhang, Z. Impact of hydrolysis conditions on the detection of mannuronic to guluronic acid ratio in alginate and its derivatives. *Carbohydrate polymers* 122, (2015), 180-188.

MASS TRANSFER AT THE EXTRACTION FROM POROUS SLABS

Marcela POPA, Eugenia Teodora IACOB TUDOSE, Ioan MAMALIGA*

Department of Chemical Engineering, Faculty of Chemical Engineering and Environmental Protection, "Gheorghe Asachi" Technical University of Iasi, 73 Prof. dr. docent Dimitrie Mangeron Street, Iasi, 700050, Romania

Abstract

The paper presents a study on the mass transfer achieved in the extraction of a high solubility salt in water from a porous inert material in the form of a slab. The obtained experimental data allowed the calculation of the salt mass transfer coefficient when a slab is washed with demineralized water of known flowrate. The driving force of mass transfer is given by the difference between the concentration at the solid-liquid interface and the liquid phase calculated using conductivity measurements.

Key words: mass transfer coefficient, porous slabs, horizontal flow

1. Introduction

There are many applications involving the mass transfer from a solid porous material in the form of a slab to a flowing liquid phase. Thus, unwanted organic or inorganic products can be removed from contaminated soils or electronic materials [1, 3, 4, 11, 17, 18]. Another example is the extraction of residual oil from underground rocks [12, 14], or the extraction of compounds from plant or animal structures, in food or pharmaceutical industries [1, 15, 19, 23].

The diffusion process underlies the mass transfer of the main compound that can be compacted or dispersed in the porous structure. During extraction, the concentration of the dissolved substance varies. The nature of the interactions between the solute and the solid matrix as well as the solid-liquid extraction mechanism, depend on the composition and origin of the solid material, generally less known. In principle, solutes can be adsorbed on the specific surface of the sample particles, in which case the interaction can be overcome using a solvent with high solute affinity, or the molecules can be physically encapsulated in the sample matrix, in which case for extraction the physical destruction of the solid material texture is necessary.

* Corresponding author: E-mail address: imamalig@tuiasi.ro (Ioan Mamaliga).

If the solute is evenly distributed in the solid matrix, the one near the solid surface will be dissolved immediately, leaving behind the porous structure of the solid residue. In this way, the solvent penetration to another level in the solid matrix is facilitated and another amount of solute is dissolved. Progressively, the process becomes more and more difficult and the degree of extraction decreases.

The porous structure geometry of the solid determines its physical and chemical properties, influencing the fluid flow hydrodynamics and the transport of extracted solute.

The process is difficult to control, on one hand, due to the liquid phase flow and on the other hand due to difficulties in estimating the solid-liquid phase contact surface. It is necessary to study this process at the interface of the two phases involved.

There are studies [6, 7] for unidirectional fluid flows through porous solids obeying Darcy's law, where the mass transfer coefficient depends on the liquid solute concentration, the liquid saturation concentration, the solid porosity, the extraction time period, the dispersion coefficient and the Darcy velocity. However, considering the pore interface variability, one can use instead of the Darcy equation, the Brinkman equation [19], or the Darcy equation with a suitable discontinuity limit condition [16].

The experimental results presented in this study were processed to:

- determine the compound extraction rate from a solid matrix;
- determine the global mass transfer coefficient for the compound extraction from the solid matrix;
- study the influence of some types of porous supports on the process.

2. Experimental

The mass transfer study for solid-liquid extraction from slabs was performed using an experimental set-up shown in Figure 1.

In the device (1) the solid sample in the form of a slab was placed. The perspex device (1) is constructed to prevent the liquid phase from moving over the top surface of the slab. The flushing fluid from the constant level feeding tank (2) passes over a threshold placed just before the slab, causing it to be uniformly soaked. The fluid flow rate, measured with a flow meter, is laminar. The salt solution conductivity determined with the conductivity meter (4) is measured at the outlet of the device.

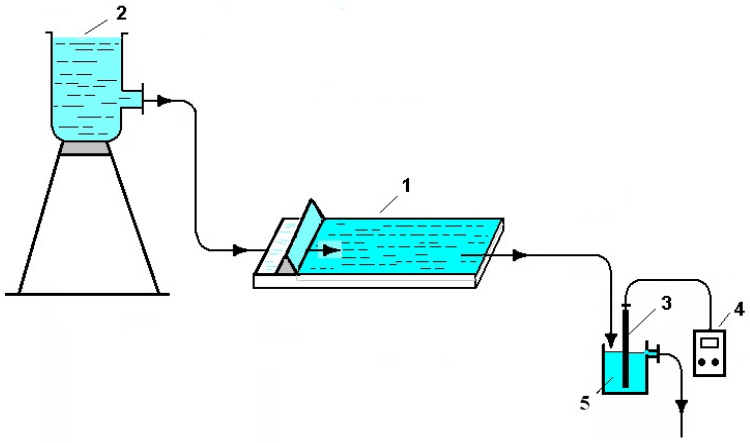

Fig. 1. The schematic diagram of the solid-liquid extraction experimental set-up with slabs; 1-extraction device, 2-vessel solvent, 3-conductivity probe, 4-conductometer, 5-sample cell

Materials and Operating Conditions

In this study, three types of materials with different porosities and therefore, different mass transfer behavior, were used, namely: sandstone, BCA and refractory brick.

In solid-liquid extraction, each porous slab used was solvent-free, polished, washed with water and oven-dried for 6 hours, at 80° C. Subsequently, impregnation was attained by immersion in 5% NaCl solution, for 48 hours. The salt extraction was carried out at 20 ± 1 ° C and atmospheric pressure, using fresh solvent. The washing fluid used was demineralized water at a flow rate of 20 L/h, with a film thickness of 1-2 mm. The extract salt concentration was measured every 60 seconds.

The porous materials used in the solid-liquid extraction were subjected to SEM-EDX analysis and the results are shown in Table 1.

Table 1.

Sample composition in chlorine and sodium, before and after impregnation

Sample/composition	Chlorine (%)	Sodium (%)
Nonimpregnated sandstone	-	0.8122
Impregnated sandstone	1.4107	1.3131
Nonimpregnated Brick	-	0.4522
Impregnated Brick	29.6754	29.4638
Nonimpregnated BCA	-	0.4926
Impregnated BCA	2.0140	3.4970

The salt solution samples obtained after extraction, from the device (1), were conductometrically measured and analyzed, based on a calibration curve experimentally determined, at the working temperature.

3. Results and discussions

The experimental data were processed based on the following hypotheses:
- the salt is evenly distributed in the porous solid material;
- the pore shape and size remain constant;
- the transfer is made over the entire porous slab surface which is completely wetted by the liquid phase;
- the flow is laminar (horizontal liquid film);
- the liquid phase salt concentration is the same, at any point.

The solute flux transferred in liquid phase is given by the equation:

$$N_A = k \cdot A(c_A^* - c_A) \tag{1}$$

The extraction rate is estimated using the following equation:

$$v_e = \frac{\Delta m}{A \cdot \Delta t_i} \tag{2}$$

The extracted component flux can be calculated with:

$$N_A = M_v \cdot \Delta c = M_v \cdot (c_{A_i} - c_{A_0}) \tag{3}$$

Notations

M_v - the liquid flowrate (demineralized water) at the sample layer entrance, m^3/s

Δt_i - time interval between two consecutive readings, s

$c_A^* - c_A$ - the driving force of the mass transfer, kg/m^3

v_e - the extraction rate, Kg/m^3s

k - the global mass transfer coefficient, $m\ s^{-1}$

A - the mass transfer area, m^2

c_A^* - the salt concentration extracted at equillibrium, Kg/m^3

c_{Ai} - the salt concentration extracted at the t_i moment, Kg/m^3

c_{A0} - the salt concentration extracted at the initial moment, Kg/m^3

t - the extraction time, s.

The obtained experimental results are shown in Figure 2 as the extract salt concentration variation with time. One can observe that the maximum concentration value is at the beginning of the process when salt elution takes place on the surface of the solid sample. This maximum value was obtained for all the studied samples. As the liquid phase penetrates the solid material pores and the salt extraction takes place, followed by the salt migration towards the slab and its transfer in the liquid film, the amount of extracted salt decreases. This results in an increase of the extraction time.

3.1. The extraction rate

The extraction rate was calculated as the mass of the extracted salt from the surface area unit, in the time unit, according to the equation (2).

3.1.1. Ceramic sandstone slabs

The studies were carried out on two types of ceramic sandstone slabs, marked sandstone 1 and sandstone 2, of similar dimensions. Figures 3 and 4 show the extraction rate profiles in time, for the two types of sandstone. One can observe an important decrease in the extraction rate in the first 300-400 s, after which the curve slope becomes very small.

The obtained values for the extracted salt flux are very similar for the same type of sample used in the study, either sandstone 1 or sandstone 2, however different values were recorded for the extraction rate values for the two different types of sandstone.

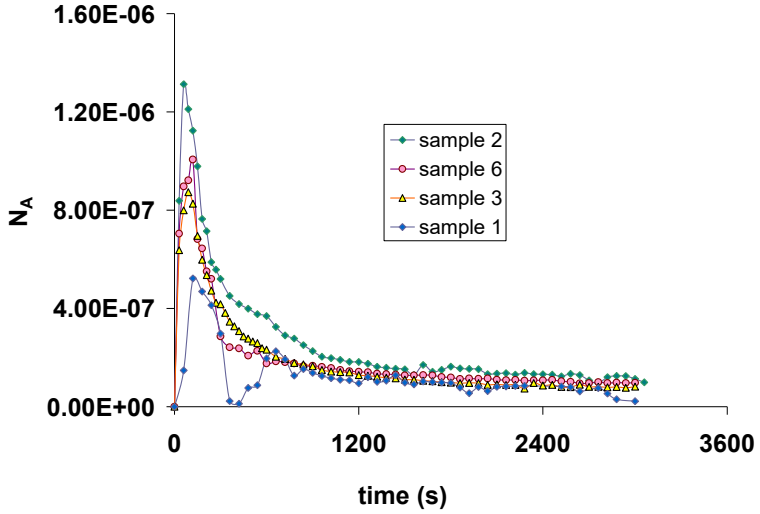

Fig. 2. Variation of the extracted salt flux in time for the sandstone slab 1

The extraction rate has values ranging from $1 \cdot 10^{-5} – 2.6 \cdot 10^{-4}$ Kg / m^2 s. Higher values were recorded for sandstone slabs 2. The analysis of the two graphs from Figures 3 and 4 indicates two stages of the process. In the first stage, the extraction rate records minimum values in the range of $4.01 \cdot 10^{-5}$ - $7.26 \cdot 10^{-5}$ Kg / m^2s, corresponding to the time of 300 s, for the six samples used, when a salt extraction takes place from the slab surface.

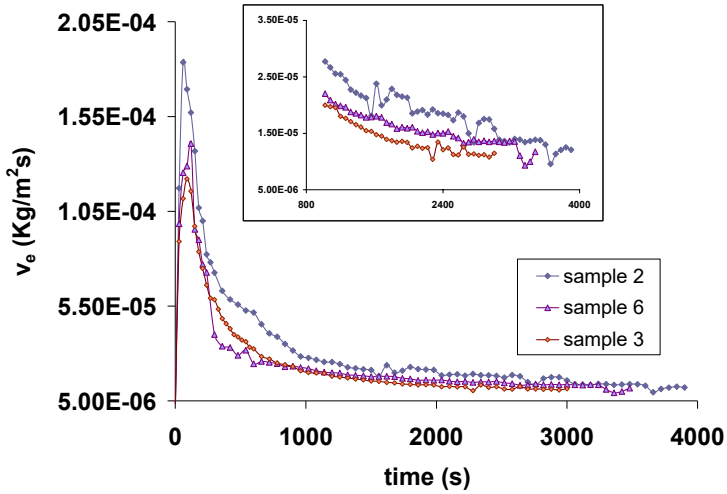

Fig. 3. The extraction rate for sandstone slabs 1

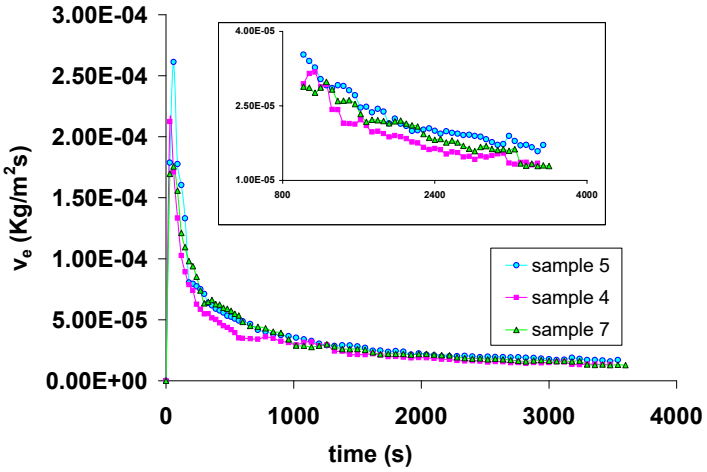

Fig. 4. The extraction rate for sandstone slabs 2

This is followed by a gradual penetration of the washing liquid into the pores both in the horizontal and in the depth directions, according to the model shown in figure 6. This is the decisive stage of the process. Salt extraction takes place slowly due to the slow liquid diffusion into the pores, followed by the salt dissolution and the liquid phase diffusion towards the exterior of the solid slab.

3.1.2. Ceramic brick slabs

The values of the NaCl extraction rate from brick slabs lie within the range of $8 \cdot 10^{-5}$- $2 \cdot 10^{-3}$ Kg / m^2 s, for an extraction time of 3000 s, as seen in Figure 5. For the brick samples, the slope change, corresponding to the passage to the second stage of the extraction, takes place at a time t = 210 s and the rate values obtained are $5.8 \cdot 10^{-4}$-$6.6 \cdot 10^{-4}$ Kg / m^{2}s.

For the second stage, the extraction rate profile has a much higher slope for brick than for the sandstone slabs. This, as well as the higher extraction rate values, can be explained by a better diffusion determined by the material characteristics.

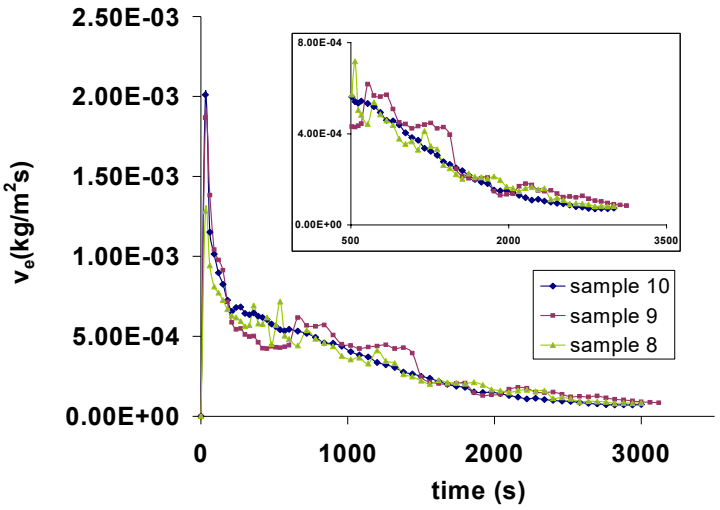

Fig. 5. The extraction rate for brick slabs

3.1.3. BCA ceramic slabs

BCA porosity is superior to brick and sandstone samples. Thus, the values recorded for the salt extraction rate are much higher than those obtained for the sandstone and the brick materials. The maximum obtained rate values are around $4 \cdot 10^{-3}$ Kg / m^2 s and the minimum rate values are approximately $7 \cdot 10^{-5}$ Kg / m^2

s, as shown in Figure 6. The salt extraction behavior reflected by the curve shape for the BCA samples resembles that of the brick samples.

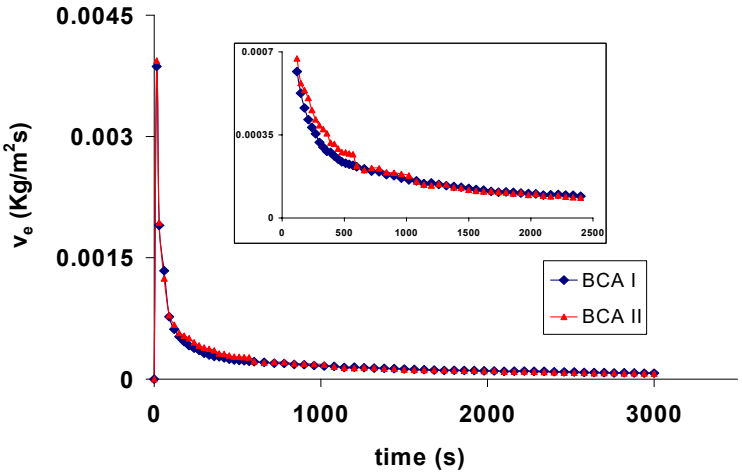

Fig. 6. The extraction rate for BCA slabs

Analyzing, however, the profile given by the extraction rate values, we find that it is close to the one obtained at the extraction from the sandstone samples. It is noted that for the BCA slabs, the slope for the second stage of the process, which begins around 210 s, is small, and the extraction rate values for the two material samples are very close.

3.2. Mass transfer coefficient

According to [21], a 2D model is efficient to study the mass transfer in a slab. According to the two films theory of Lewis, the global mass transfer coefficient is given by the mass transfer coefficient in the continuous liquid phase and the mass transfer coefficient in the solid phase. As a result, we consider that the process takes place according to the model shown in Figure 7, with a laminar liquid phase flow in thin film and the extraction taking place in two stages. In the first step, the salt is washed from the surface of the solid material sample. In the second step, according to the model shown in Figure 7 and the equation (1), the salt extraction from the material pores takes place, followed by the diffusion of the liquid phase towards the upper surface of the solid slab.

In the first stage of the process, the mass transfer coefficient is given by the mass transfer coefficient in the liquid:

for $\delta_p = 0$ $\quad k \cong k_L$, where $\mathrm{k_L} = \dfrac{\mathrm{D_{salt}}}{\delta}$ (4)

In the second stage, at large time values, the extraction coefficient is determined by the mass transfer coefficient in the liquid phase and by the salt effective diffusion coefficient from the solid material in the liquid phase:

for $\delta_p \geq 0$ $\quad k = f(k_L, k_s)$, where $k_s = \dfrac{D_{ef}}{\delta_p}$, thus : $k = f\left(k_L, \dfrac{D_{ef}}{\delta_p}\right)$

or $k = \dfrac{1}{\dfrac{1}{k_L} + \dfrac{\delta_p}{D_{ef}}}$ (5)

where: k is the overal mass transfer coefficient, m·s^{-1}

k_L - mass transfer coefficient in lichid phase, m·s^{-1}

D_{ef} - the effective diffusion coeficient in the solid pores

δ - the liquid film thickness, m

δ_p - the salt diffusion distance towards the surface of the porous solid material, m

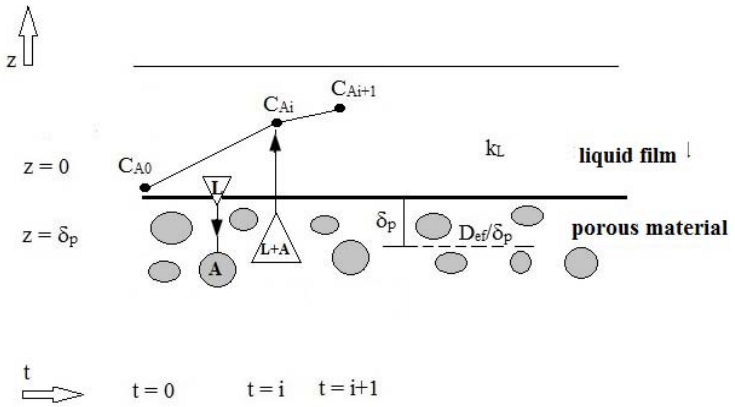

Fig. 7. Salt extraction model from a porous slab

The mean driving force of the mass transfer, Δc_{mean}, decreases with time, on one hand, due to the increase in the salt concentration of the liquid phase, and on the other hand, due to the decrease in the salt concentration of the liquid phase inside the porous matrix. Figure 8 shows the decreasing profile of the salt concentration in the solid matrix in time and the decreasing driving force of the process.

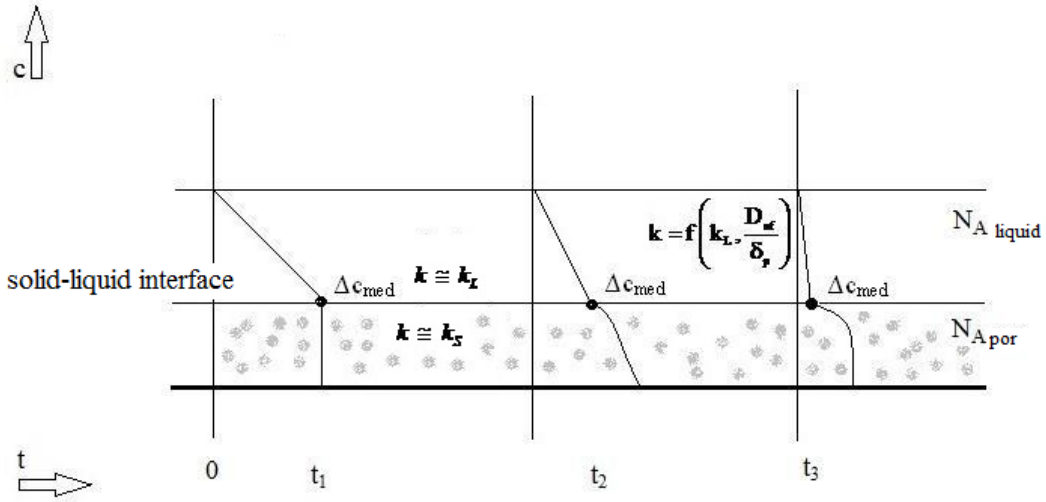

Fig. 8. Concentration profile near the solid-liquid interface

In Equation (5), the term that changes over time is δ_p, since the salt diffusion distance increases as the process unfolds, k_L and D_{ef} having constant values over time. It is the time that determines the process in the second step as the liquid phase diffusion distance into and out of the pores increases.

Based on the equations (1) and (3) and using the obtained experimental results the average mass transfer coefficient was calculated with the following equation:

$$k_L = \frac{N_A}{A \cdot \Delta c_{mean}}, \quad (m/s) \tag{6}$$

The obtained experimental values were compared with the values calculated using existing equations in the literature for laminar flow. Thus, according to [22], for the average mass transfer coefficient from a solid surface with a characteristic length L, under laminar flow conditions, the proposed correlation is:

$$Sh = 0.664 \cdot Re^{0.5} Sc^{0.33} \tag{7}$$

valid for $Re < 3 \times 10^5$ şi $0.6 < Sc < 2500$, where:

$$Sh = \frac{k_L \cdot L}{D_{ef}} \quad \text{is the Sherwood number} \tag{8}$$

$$\mathrm{Re} = \frac{4\Gamma}{\eta} \text{ is the Reynolds number, with } \Gamma = \frac{4M_m}{P} \text{ [9]} \quad (9)$$

$$\mathrm{Sc} = \frac{\eta}{\rho \cdot D_{ef}} \text{ is the Schmidt number} \quad (10)$$

with: M_m - the mass liquid flowrate (Kg/s);
P – the wetted perimeter (m);
η, ρ - the liquid dynamic viscosity and density, respectively;
L- the characteristic length, calculated as the equivalent diameter of the liquid film, $L = \frac{4A}{P}$ (m);
A - flow cross-sectional area of liquid.

3.2.1. Sandstone ceramic slabs

The graphs in Figures 9 and 10 present values obtained by applying the equation (6) to the experimental data regarding the salt extraction from sandstone slabs 1 and 2. Similar to the extraction rate, the graphical representation of mass transfer coefficient has a greater slope for the type 2 sandstone than the type 1, indicating a slower extraction in the latter case.

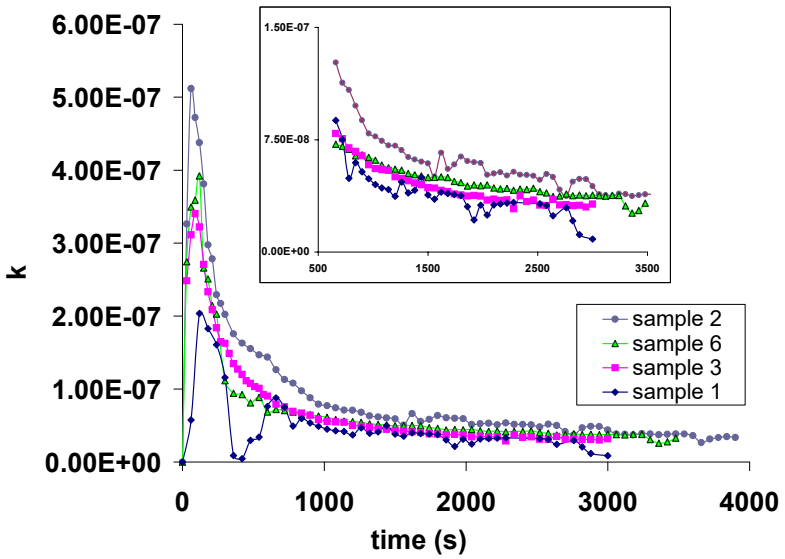

Fig. 9. Mass transfer coefficient for NaCl extraction from sandstone slabs 1

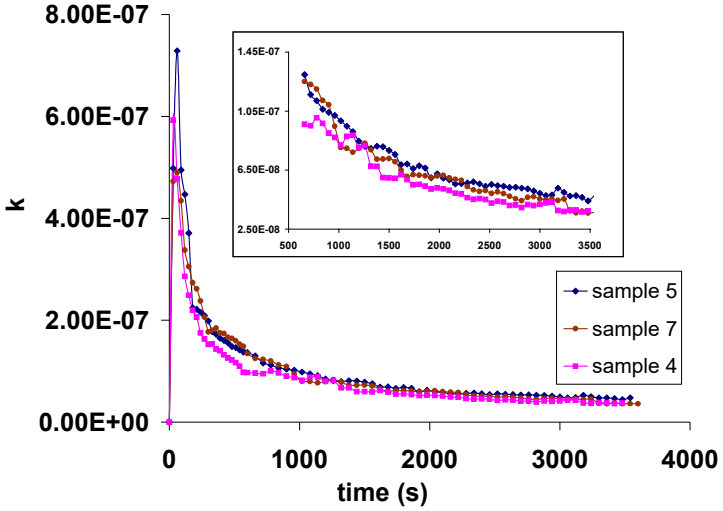

Fig. 10. Mass transfer coefficient for NaCl extraction from sandstone slabs 2

The mass transfer coefficient values for the sandstone slabs are between $7.19 \cdot 10^{-8}$ - $1.29 \cdot 10^{-7}$ Kg / m^2s at 660 s and $8.66 \cdot 10^{-9}$ - $4.93 \cdot 10^{-7}$ Kg / m^2s at 3000 s. The values are closer for the type 2 sandstone samples. It is noted that there is no predictable distribution of these points.

3.2.2. Brick slabs

Similar to the salt extraction from sandstone slabs, in brick samples, the mass transfer coefficient measured values do not fit a particular profile. The maximum values at t = 660 s are in the range of $1.23 \cdot 10^{-6}$ - $1.72 \cdot 10^{-6}$ Kg / m^2s and at t = 3000 s the interval is much narrower $2.04 \cdot 10^{-7}$ - $2.52 \cdot 10^{-7}$ Kg / m^2s, as shown in Figure 11.

3.2.3. BCA slabs

The mass transfer coefficient values obtained for the two brick samples are very close, especially over the time interval 600 s - 3000 s. The maximum values are between $6.02 \cdot 10^{-7}$ Kg / m^2s and $6.15 \cdot 10^{-7}$ Kg / m^2s and the minimum values in the range $1.94 \cdot 10^{-7}$ Kg / m^2s - $2.04 \cdot 10^{-7}$ Kg / m^2s.

Unlike the other types of samples used, for BCA slabs a uniform distribution of the mass transfer coefficient values is observed in Figure 12. The graph has a high slope at the beginning, specific to the first stage of the extraction process, while in the second stage, this becomes much smaller due to the slow extraction process from the solid material pores.

Figure 13 shows a comparison among the mass transfer coefficients variations with time for the three types of studied porous materials. There is a large difference between the values obtained for sandstone and brick slabs.

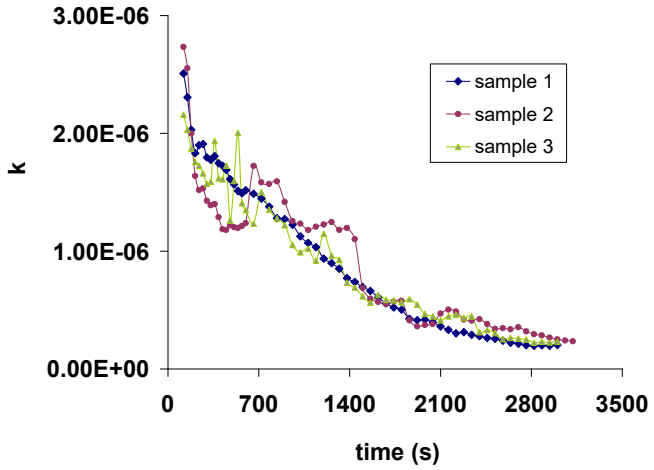

Fig. 11. Mass transfer coefficient for NaCl extraction from brick slabs

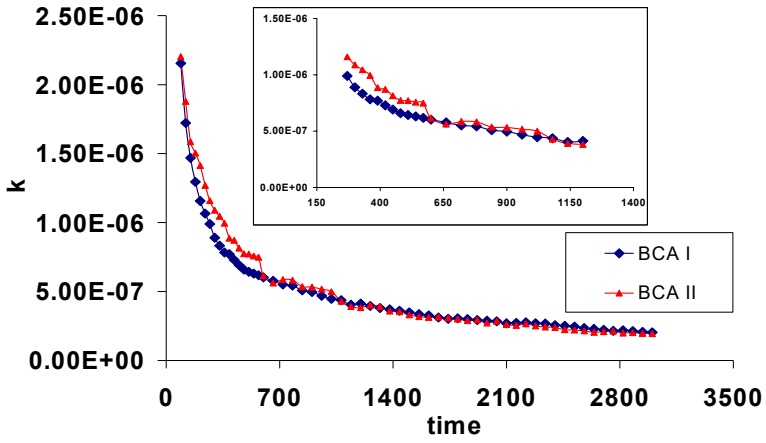

Fig. 12. Mass transfer coefficient for NaCl extraction from BCA slabs

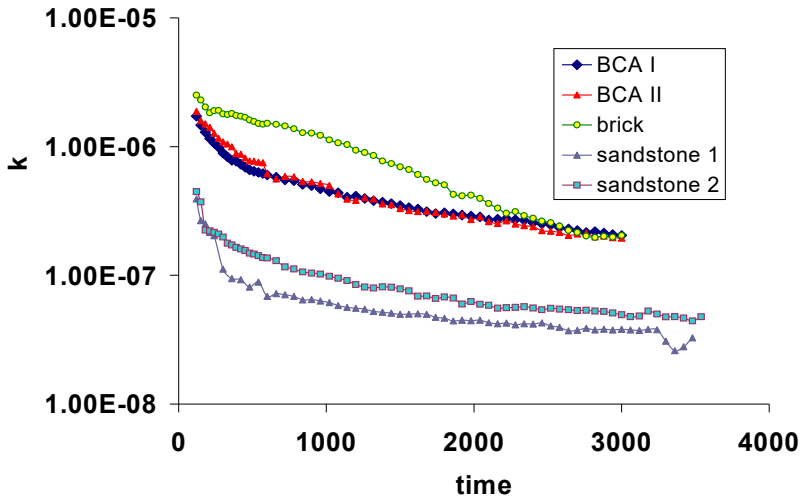

Fig. 13. Comparison of mass transfer coefficients for NaCl extraction from different types of slabs

For the BCA and the brick slabs, the mass transfer coefficient values are very close at times greater than 2000 s, but also, in the first stage of the process, at times shorter than 210 s. The highest slope is observed for the brick samples, which shows that in this case, the largest salt amount is removed up to t = 2000 s. On the other hand, the sandstone and the BCA slopes are smaller than for the brick samples, thus the amounts of extracted salt are smaller, but equal for the two types of BCA samples. The results obtained by applying the equation (7) for the volume flow at the inlet and the outlet of the porous solid slab, subjected to extraction, are shown in Table 2:

Table2:

Comparison between mass transfer coefficients for all types of samples

Slab type	k_L(eq. 7)	$k_{Lexperimental\ I\ (0 - 120\ s)}$	$k_{Lexperimental\ II\ (120 - 3000\ s)}$
sandstone	$1 \cdot 10^{-6}$	$2.04 \cdot 10^{-7} - 4.47 \cdot 10^{-7}$	$8.66 \cdot 10^{-9} - 4.93 \cdot 10^{-7}$
brick	$1.99 \cdot 10^{-6}$	$2.16 \cdot 10^{-6} – 2.73 \cdot 10^{-6}$	$2.04 \cdot 10^{-7} - 2.52 \cdot 10^{-7}$
BCA	$2.11 \cdot 10^{-6}$	$1.72 \cdot 10^{-6} - 1.88 \cdot 10^{-6}$	$1.94 \cdot 10^{-7} - 2.04 \cdot 10^{-7}$

4. Conclusions

The results from this study indicate the following:

- the extraction rate and mass transfer coefficient are influenced by the type of sample used (its structure);

- for both the extraction rate and the mass transfer coefficient, the highest values are obtained for the brick samples and the minimum for the slabs, proportional to the porosity and the amount of salt contained, but also depending on the pore structure network evenness;

- the mass transfer coefficient according to the equation (3) is proportional to the driving force of the process, which decreases over time as the difference between the salt concentration in the liquid and the salt concentration at the surface of the porous solid decreases;

- high values for the mass transfer coefficient are obtained according to the high salt sample concentration. The highest value is recorded for the brick samples, having the highest salt content (according to Table 1);

- the comparison between experimental data and those obtained by applying the equation (7) shows a good agreement for the low-time extraction (domain I), but for time values greater than 120 s, the equation (7) cannot be applied. For this domain (II), the influence of diffusion in the material pores is important.

- the mass transfer coefficient obtained experimentally is a global one and sums up the resistance to mass transfer from the interface to the liquid as well as the diffusion resistance inside the porous material. The coefficient obtained from the calculations is the only one describing the mass transfer in the liquid film.

REFERENCES

[1] Aissou, M., Chemat-Djenni, Z., Yara-Varon, E., Fabiano-Tixier, A-S., Farid, C., Limonene as an agro-chemical building block for the synthesis and extraction of bioactive compounds, *Comptes Rendus Chimie*, 20, (2017), 346-358.

[2] Augustijn, D.C. M., Jessup, R. E., Rao, P.S. C., Wood, A. L., Remediation of contaminated soils by solvent flushing, *Journal of environmental engineering-ASCE*, 120, (1994), 42.

[3] Cabidoche, Y.-M, Achard R., Cattan P., Clermont-Dauphin C., Massat F., Sansoulet J., Long-Long-term pollution by chlordecone of tropical volcanic soils in the French West Indies: A simple leaching model accounts for current residue, *Environmental Pollution*, 157(5), (2009), 1697–1705.

[4] Cuenot F., Meyer M., Bucaille A., Guilard R., A molecular approach to remove lead from drinking water, *Journal of Molecular Liquids*, 118, (2005), 89– 99.

[5] Dalgren K.E., Düker A, Arwidsson Z, von Kronhelm T, van Hees P.A., Re-cycling of remediated soil – Evaluation of leaching tests as tools for characterization, *Waste Management*, 31, (2011), 215–224.

[6] Halder, A., Datta, A. K., Surface heat and mass transfer coefficients for multiphase porous media transport models with rapid evaporation, *Food and Bioproducts Processing*, 90, Issue 3, (2012), 475–490.

[7] Krenn, J., Baesch, S., Schmidt-Hansberg, B., Baunach, M., Scharfer, P., Schabel, W.,Numerical investigation of the local mass transfer on flat plates in laminar flow, *Chemical Engineering and Processing,* 50, (2011), 503–508.

[8] Librán, C.M., Mayor, L, Garcia-Castello, E.M., Vidal-Brotons, D., Polyphenol extraction from grape wastes: Solvent and pH effect, *Agricultural Sciences*, 4, (2013), 56-62.

[9] Tudose, R.Z., Mămăligă. I., Coeficienţi individuali de transfer de masă la curgerea lichidelor în filme subţiri, *Revista de Chimie*, 45, (1994), 652-662.
[10] Nayak, C.A., Chethana, S., Rastogi, N.K., Raghavarao, K.S.M.S., Enhanced mass transfer during solid–liquid extraction of gamma-irradiated red beetroot, *Radiation Physics and Chemistry*, 75, (2006), 173–178.
[11] Park, Y.S., Moon, J.H., Kim, D.S., Ahn, K.H., Treatment of a polluted stream by a fixed-bed biofilm reactor with sludge discharger and backwashing system, *Chemical Engineering Journal,* 99, (2004), 265–271.
[12] Pathak, S., Singh, T., A mathematical modelling of imbibition phenomenon in inclined homogenous porous media during oil recovery process, *Perspectives in Science*, 8, (2016), 183-186.
[13] Pinho, G. P. de., Neves, A. A., Queiroz, M. E. L. R. de., Silvério, F. O., Pesticide determination in tomatoes by solid–liquid extraction with purification at low temperature and gas chromatography, *Food Chemistry*, 121, (2010), 251–256.
[14] Salehi, M.M., Omidvar, P., Naeimi, F., Salinity of injection water and its impact on oil recovery absolute permeability, residual oil saturation, interfacial tension and capillary pressure, *Egyptian Journal of Petroleum*, 26, (2017), 301-312.
[15] Seikova I., Simeonov E., Ivanova E., Protein leaching from tomato seed - experimental kinetics and prediction of effective diffusivity, *Journal of Food Engineering,* 61, (2004), 165-171.
[16] Tio, K. K., Sadhal, S.S., Boundary conditions for Stokes flows near a porous membrane, *Appl. Sci. Res*., 52, (1994), 1-20.
[17] Tiruta-Barna L., Fantozzi-Merle C., de Brauer C., Barna, R., Leaching behaviour of low level organic pollutants contained in cement-based materials, *Journal of Hazardous Materials B*, 138, (2006), 331–342.
[18] Tsang, C-F., Neretnieks, I, Tsang, Y., Hydrologic issues associated with nuclear waste repositories, *Water Resources Research*, 51, (2015), 6923–6972.
[19] Vafai, K., Thiyagaraja, R., Analysis of flow and heat transfer at the interface region of a porous medium, *International Journal of Heat and Mass Transfer*, 30(7), (1987), 1391-1405.
[20] Vázquez G., Fernández-Agulló A., Gómez-Castro C., Freire M.S., Antorrena G., González-Álvarez J., Response surface optimization of antioxidants extraction from chestnut (*Castanea sativa*), *Industrial Crops and Products,* 35, (2012), 126– 134.
[21] Zeng, Y., Lee, T.-S., Yu, P., Low, H.-T., Numerical study of mass transfer coefficient in a 3D flat-plate, rectangular microchannel bioreactor*, International Communications in Heat and Mass Transfer,* 34, (2007), 217–224.
[22] Welty, R.J., Wicks, C.E., Wilson, R.E., Rorrer, G.L., *Fundamentals of Momentum, Heat, and Mass Transfer*, 5th Edition, John Wiley & Sons, 2008.
[23] Simeonov, E., Koleva, V., Solid-liquid Extraction of Tannins from Geranium Sanguineum L. –Experimental Kinetics and Modelling, *Chemical and Biochemical Engineering Quarterly,* 26(3), (2012), 249–255.

OPTIMAL OPERATING POLICY OF A FLUIDIZED BED BIOREACTOR USED FOR MERCURY UPTAKE FROM WASTEWATERS BY USING IMMOBILIZED *P. PUTIDA* CELLS

Andreea Georgiana ŞCOBAN, Gheorghe MARIA*

Department of Chemical and Biochemical Engineering, Faculty of Applied Chemistry and Materials Science, University Politehnica of Bucharest, 1-7 Gh. Polizu Street, 011061, Bucharest, Romania

Abstract

A model-based analysis of a three-phase continuously operated fluidized-bed bioreactor (TPFB) is developed in order to determine the multi-objective optimal and sustainable operating policy of a TPFB used for removing mercury ions from wastewater. More specifically, the analysis is focus on finding the optimal feeding policy of alginate porous beads of known particle size containing immobilized biomass (P. putida bacteria) that minimize the biomass consumption, while keeping a quasi-constant high mercury removal conversion, under quasi-stable reactor performances. The extended bioreactor model is accounting for the biomass growth, biodegradation, and its partial leakage and washout. Bioreactor dynamics prediction has been generated by using a simple Michaelis-Menten kinetic model adopted from literature. The resulted optimal feeding policy of the bioreactor points out the importance of the adoption of an extended and adequate process/reactor model able to solve difficult engineering operation problems by quickly adjusting the feeding conditions according to the time-varying characteristics of the biomass culture, and to the limited possibilities to control the process during the wastewater residence time in the bioreactor.

Key words: mercury uptake by immobilized *P. putida* culture; fluidized-bed biological reactor; multi-objective optimization; biomass growth, biodegradation, washout dynamic simulation

1. Introduction

The bioreactor optimal operation is one of the most difficult and challenging engineering problem, due to well-known bioprocess complexity and variability, besides the large number of variables influencing the bioprocess difficult to be accounted in a quite reduced kinetic model.

* Corresponding author. Email address: gmaria99m@hotmail.com, (Gh. Maria)

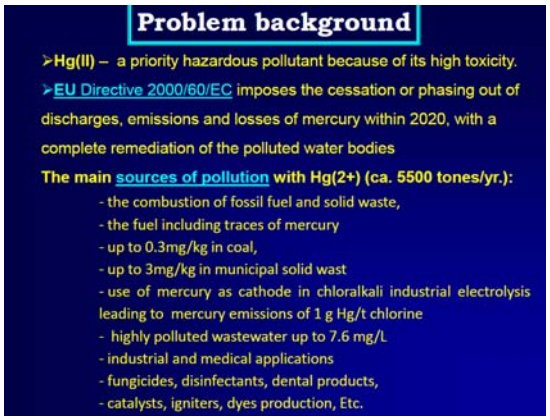

Fig. 1. The mercury removal problem from wastewaters [1, 2].

Fig. 2. Classical removal procedures of mercury from wastewaters [1, 2].

Mercury is considered a priority hazardous pollutant, due to its high toxicity. A maximum permissible concentration of 50 μg/L is imposed to discharged wastewaters [1]. Moreover, the European Union stated, under Directive 2000/60/EC, the cessation or phasing out of discharges, emissions and losses of mercury within 2020, with a complete remediation of the polluted water bodies [3]. ”Heavy metal pollution of the aquatic environment and particularly mercury pollution due to mining and industrial activities still represents a high worldwide concern. The main source of mercury is the combustion of fossil fuel and solid waste (Fig. 1), the fuel including traces of mercury up to 0.3 mg/kg in coal, and up to 3 mg/kg in municipal solid waste [3]. However, other significant sources of pollution can be also mentioned, such as the use of mercury as cathode in the chlor-alkali industrial electrolysis at large scale leading to significant mercury emissions (ca. 1 g Hg/t chlorine; [4]), and highly polluted wastewater (up to 7.6 mg/L [1]). Mercury is also used in numerous industrial and medical applications (fungicides, disinfectants, dental products, catalysts, igniters, dyes production, etc.)” [5-7].

The current treatment procedures (Fig. 2) to remove mercury from wastewater register in the following categories [1]: i) Precipitation with hydrogen sulfide, with the disadvantage of handling large amounts of toxic H_2S, and resulting large volumes of mercury contaminated sludge necessary to be deposited in special places, with no possibility of recycling the precipitated mercury; ii) Retention on the ion exchange columns, with the disadvantage of requiring costly adsorbents; it can be applied only for removing low loads of mercury from wastewater; besides, most of ion-exchange resins cannot be regenerated thus raising disposal problems, while the renewable resins are expensive; iii) Retention on various cheap sorbents, such as activated carbon, char from coal, volcanic tuff, modified cellulose or agro-based waste materials; iv) Renewable polymeric

membranes also display promising sorption and filtration capabilities; v) Bioaccumulation into genetically modified bacteria cells by sequestering mercury via binding to metallothionein molecules or cytosolic chelating agents; this method is limited by the cell metabolic resources, e.g. by using cyanobacteria, *Bacillus sp.*, or *E. coli*.

Microbial "detoxification" of wastewaters approached in this paper involves metabolic processes of certain cell cultures, that results in reducing the mercuric ions to elementary volatile mercury, which is less toxic for micro-organisms and more easily to be recovered from liquid / gas (air) phases. *Pseudomonas sp.*; *Aeromonas hydrophila*; *Escherichia coli* are to be mentioned among the resistant strains used [1]. The process takes place inside the living cells with a high efficiency; the *mer*-reductase / NADPH used being continuously synthetized and regenerated during the cell growth (see the simplified reactions in Fig. 3).

This paper is aiming at using a multi-objective criterion and an elaborated bioreactor model to derive sustainable optimal operating policies of a TPFB used for mercury uptake from wastewaters by immobilized cultures of *P. putida.* The target optimization criteria concern the sustainability of the TPFB operation, leading to the concomitant optimality of: I) an economic criterion (maximum of mercury removal conversion); ii) a safety-stability criterion (quasi-stationary removal conversion over a defined time-horizon); iii) an environmental criterion (minimum wasted biomass with mercury traces leaving the TPFB).

2. Bioreactor model and optimization problem formulation

To simulate the TPFB reactor performances and to derive the optimization problem solution, an extended dynamic ideal model of the bioreactor was adopted (Fig. 5 [1]), including a simple Michaelis-Menten kinetics of the bioprocess derived from a structured extended model (Fig. 4, [7-9]), thus allowing its use for bioprocess optimization. The model includes the main characteristics of the bioprocess on the solid support, and the solid-liquid-gas interfacial transport of the mercury, even if additional calculations are necessary to derive the particle effectiveness and to solve the mass flux equality at solid-liquid-gas interface during the transient regime. The extended bioreactor model is accounting for the biomass growth, biodegradation, and its partial leakage and washout (Fig. 4, [7-9]). The nominal operating conditions of the TPFB are presented in Fig. 3.

The TPFB model main hypotheses are presented by [1]. In short, due to the well-mixing conditions, the mercury ions diffuse from bulk phase through the external diffusional film surrounding the particles and then through the internal

pores until reaching the immobilized biomass where the mercury is crossing the cell membrane, and then it is reduced to metallic mercury (see the simplified reactions in Fig. 3). The resulted metallic mercury from the cell cytosol diffuses through the cell membrane and then it is transported as micro-drops (of ca. 5 μm diameter [3]), or dissolved (solubility of 26 μg/L at 26ºC) to the gas-liquid interface from where it passes as vapors into the homogeneous gas phase (air). Low amounts of mercury bio-accumulated into bacteria are neglected in the model. Mercury mass balance in the liquid and gas phases includes the inlet-outlet and transport terms (Fig. 5).

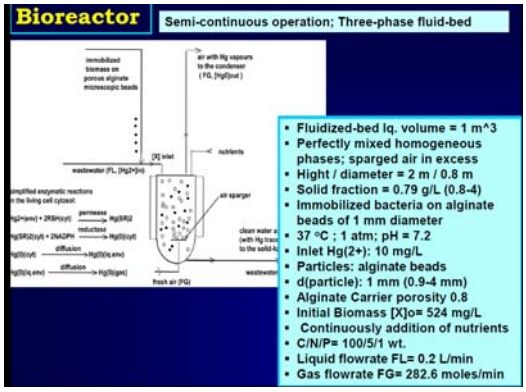

Fig. 3. The main characteristics and nominal operating conditions of the semi-continuous TPFB bioreactor used for mercury removal from wastewaters [1, 2].

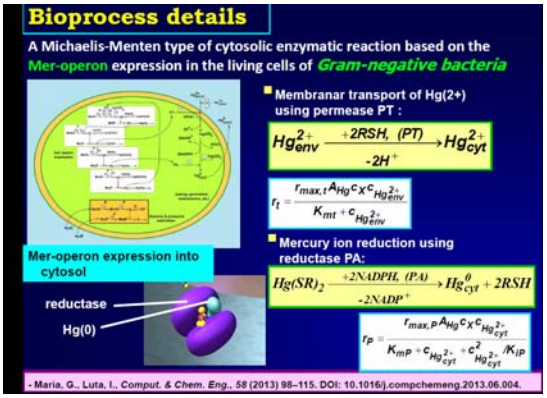

Fig. 4. The main mercury uptake kinetic model in on the immobilized cultures of *P. putida* in the approached TPFB [1, 2].

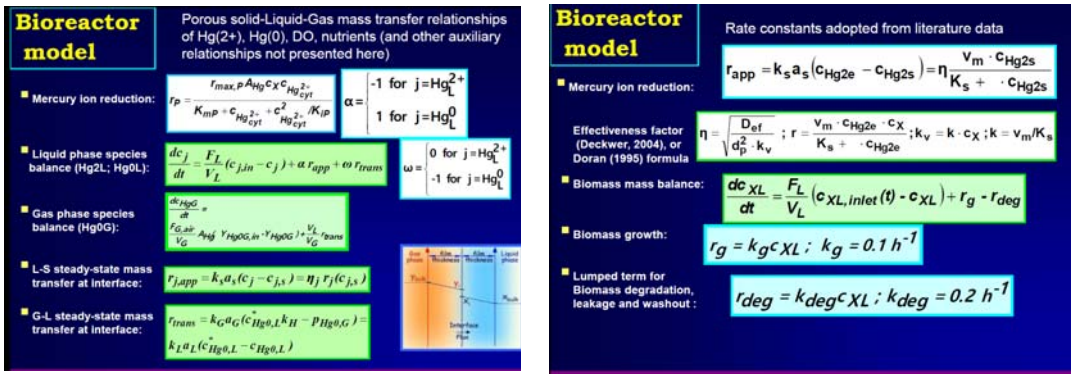

Fig. 5. TPFB bioreactor math model (left), and auxiliary relationships (right). See [1] for details.

3. Solving the optimization problem, and results

To solve this complex multi-objective optimization problem, the "weighting function method" has been used (joint function Φ in Fig. 6-right), by associating to each criterion (Φ_j, j=1-3) weighting factors (giving less weight to the biomass consumption: $w_{x_{Hg}}$, w_σ, and w_X in this case), chosen depending on the relative importance given to each objective. The formulated normalized three objective functions for the optimization problem, accounts for (Fig. 6):
i) an economic criterion, that is maximum of the average mercury ion reduction conversion (x_{Hg}), over the considered running-time interval t∈[0, 300] min.;
ii) a safety criterion, that is a minimum standard deviation (denoted by σ) of x_{Hg} from its average value over the considered running-time interval;
iii) an environmental minimum impact criterion, that is minimum biomass consumption over the considered running-time interval.

The optimization problem variables are the concentration of the feeding biomass [$c_{XL,\ inlet,100}$; $c_{XL,\ inlet,200}$; $c_{XL,\ inlet,300}$] over three considered running-time intervals [0-100], [100-200], and [200-300] min. during the batch time t∈[0, 300] min. (Fig.7-8) [1].

The best TPFB reactor operating policy B (Fig.8) was obtained for the relative weights: $w_{x_{Hg}} = w_\sigma = 1$; $w_X = 0.1$. by giving less weight to the biomass consumption, thus ensuring a maximum conversion, but also quite-uniform over the running time, with the expense of a higher consumption of biomass. This operating policy is preferred because the biomass is cheap and renewable, while the removal of mercury from wastewater is a very important ecological issue deserving lots of investments, and operational costs.

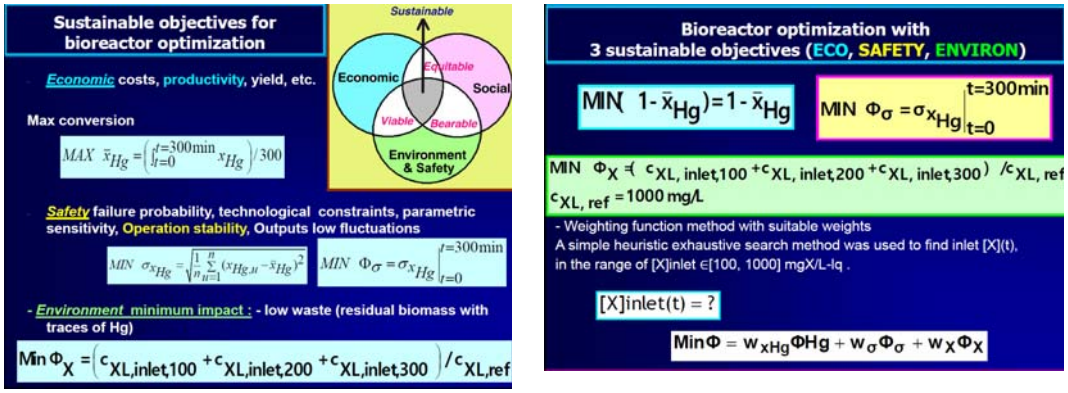

Fig. 6. The considered three optimization objectives of the semi-continuous TPFB bioreactor used for mercury removal from wastewaters (left), and the joint optimization criterion Φ (right)[1,2].

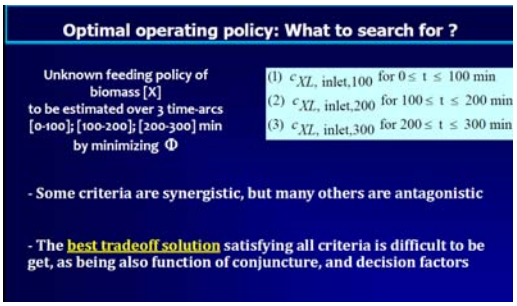

Fig. 7. The optimization problem variables $[X]_L$ over the considered three running-time intervals during the batch time $t \in [0, 300]$ min [1].

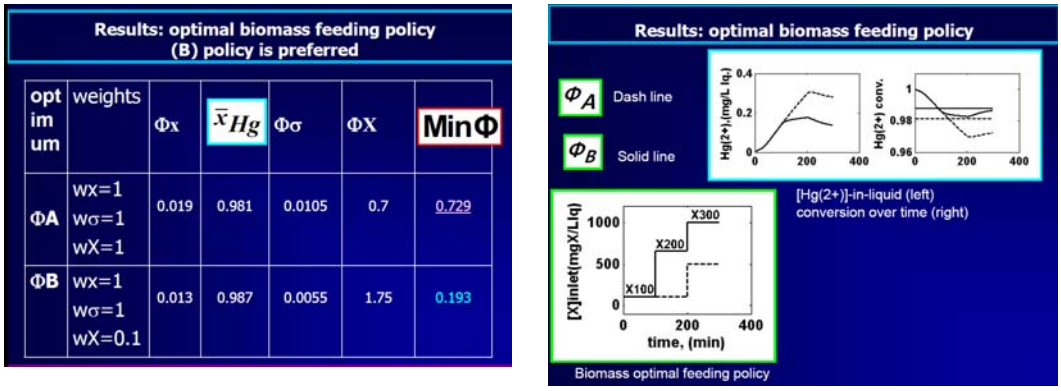

Fig. 8. The TPFB bioreactor performances for two optimal operating policies (A, and B). (left) realized optimization indices; (right) species dynamics [1].

4. Conclusions

Derivation of alternative optimal operation policies of a TPFB bioreactor used for testing mercury removal efficiency by using immobilized bacteria on a suitable porous support (alginate beads) is an essential engineering analysis to be used in further process scale-up and control.

In the simulated case study, the very effective bacteria metabolism allows an efficient reduction of the cytosolic mercury (92-99% conversion), excretion and transport of the volatile metal to the gas phase for a high pollutant load in the wastewater. By keeping a reasonable small size of alginate particles (1-2 mm), the most important control parameters appear to be the biomass load in the bioreactor and the wastewater/biomass feed flow rate.

The use of an accurate Michaelis-Menten kinetic model of the reduction bioprocess, and of a reasonable extended bioreactor model are essential steps for deriving satisfactory and interpretable results, that is prediction of various optimal operating alternatives. The study points- out the high importance of considering a

detailed biomass mass balance in the bioreactor model for ensuring a satisfactory precision of the results.

Finally, the use of immobilized (modified) resistant bacteria in fluidized-bed aerators is proved as being a viable, effective, and less costly alternative for mercury removal from wastewaters at a large-scale. The optimal choice of the operating parameters, and especially the optimal biomass continuous addition policy can be ranged to ensure a high and quasi-stationary process conversion (around 99%), eventually leading to mercury loads in the bioreactor effluent lower than the regulations' threshold, with the expense of a moderate biomass consumption. This disadvantage is compensated by the use of a cheap and renewable biomass, and by the tremendous ecological importance of removing the very toxic mercury from wastewaters, or from surface waters.

Acknowledgment. First author is grateful for the participation grant to the 20th Romanian International Conference on Chemistry and Chemical Engineering offered with generosity by the Romanian Chemical Engineering Society.

REFERENCES

[1] Scoban, A.G., Maria, G., Model-based optimization of the feeding policy of a fluidized bed bioreactor for mercury uptake by immobilized Pseudomonas putida cells, *Asia-Pacific Journal of Chem. Eng*., 11, (2016), 721-734.

[2] Scoban, A.G., Maria, *G.,* Optimal operating policy of a fluidized bed bioreactor used for mercury uptake from wastewaters by using immobilized *P. putida* cells, 20th Romanian International Conference on Chemistry and Chemical Engineering, Poiana Brasov (Romania), 6-9 Sept. 2017. http://riccce20.chimie.upb.ro/

[3] Di Natale, F., Lancia, A., Molino, A., Di Natale, M., Karatza, D., Musmarra, D., Capture of mercury ions by natural and industrial materials. *Journal of Hazardous Materials*, B132, (2006**)**, 220–225.

[4] Leonhäuser, J., Röhricht, M., Wagner-Döbler, I., Deckwer, W.D., Reaction engineering aspects of microbial mercury removal, *Engineering in Life Sciences,* 6, **(**2006*),* 139-148.

[5] Deckwer, W.D., Becker, F.U., Ledakowicz, S., Wagner-Döbler, I., Microbial removal of ionic mercury in a three-phase fluidized bed reactor, *Environmental Science and Technology,* 38, (2004), 1858-1865.

[6] Maria, G., Luta, I., Maria, C., Model-based sensitivity analysis of a fluidised-bed bioreactor for mercury uptake by immobilised *Pseudomonas putida* cells, *Chemical Papers,* 67, (2013), 1364–1375.

[7] Maria, G., Luta, I., Structured cell simulator coupled with a fluidized bed bioreactor model to predict the adaptive mercury uptake by *E. coli* cells, *Computers & Chemical Engineering*, 58, (2013), 98-115.

[8] Maria. G., A whole-cell model to simulate the mercuric ion reduction by E. coli under stationary and perturbed conditions, *Chemical and Biochemical Engineering Quarterly*, 23, (2009), 323-341.

[9] Maria, G., A dynamic model to simulate the genetic regulatory circuit controlling the mercury ion uptake by *E. coli* cells, *Revista de Chimie*, 61, (2010), 172-186.

ANALYSIS OF THE THERMAL BEHAVIOR OF CERTAIN BABY TEATS

Andreea MIHAILĂ, Ana-Maria ALISTAR, Roxana FLOREA, Gabriela LISA*

Department of Chemical Engineering, Faculty of Chemical Engineering and Environmental Protection "Cristofor Simionescu", "Gheorghe Asachi" Tehnical University, Iasi, 73 Prof.dr.doc. Dimitrie Mangeron street, 700050 Iasi, Romania

Abstract

The research was aimed at characterizing through thermal analysis, in dynamic conditions, in different work atmospheres, different types of teats used for baby feeding. For this purpose, dynamic thermal analysis (TG and DTG) and differential scanning calorimetry (DSC) were applied. The results reveal a degradation that occurs in two or more stages and follows a complex mechanism, with different mass losses, depending on their structure and the atmosphere in which thermal decomposition was achieved. It is able to conclude that, under isothermal conditions in air, the three baby teats under survey can be maintained at constant temperature (120°C) for 20 minutes without loss of mass after thermal treatment. Differential scanning calorimetry allowed gathering information about the composition of the materials which the tested baby teats were made of.

Key words: TG, DTG, DSC, Thermal stability, Baby teats

1. Introduction

The analysis of the thermal behavior of different types of materials is extremely important both theoretically and practically. From a practical point of view, tests analyzing the thermal behavior of materials may provide information about the conditions in which they may be processed or used without an alteration of their properties [1]. From a theoretical viewpoint, these studies may lead to obtaining information about thermal degradation mechanisms under different conditions. The main advantages of thermal analysis methods are: small sample size (3-10 mg), a wide range of temperature variation programs that can be used, the samples under analysis can be in solid, liquid or gel state and relatively short experimental time.

* Corresponding author: E-mail address: gapreot@ch.tuiasi.ro or gapreot@yahoo.com, (Gabriela Lisa)

The thermal analysis of materials which different utensils used for baby feeding are made of is extremely important because there may be cases where the inappropriate use of these tools may jeopardize their health [2-4].

Teats used to feed babies are subjected to the sterilization process by which all or part of the microorganisms on or inside them are removed or destroyed. There are several methods used, among which sterilization by boiling is the oldest and most used method of sterilization. However, boiling uses teats faster than other methods of sterilization. The boiling method is very cost effective, but teats, which are made of silicone or latex, get damaged and need to be replaced much more often, because thermal decomposition may result in a series of compounds that are left on the surface of the teats and that may have an impact on the baby's health. Chemical sterilization is another method used for this purpose. This sterilization method is based on sinking the teats into sterilizing liquid. The duration of sterilization is recommended by the manufacturer, and the ready-to-use sterilizing liquid is sold in pharmacies. The advantages of this method are the relatively low price of these solutions and the ease of sterilization. Furthermore, this solution may be used for up to 24 hours, so the parent has permanent access to the ready-to-use bottle to sterilize teats. The drawbacks of this method are the sterilization time (about 30 minutes), the taste and smell that may linger on the sterilized objects and the need to rinse bottles with boiled water after they are removed from the sterilizing solution. Another procedure that may be used is steam sterilization. This method involves the use of an electric sterilizer or of a microwave sterilizer, but the process is the same: the use of hot steam to destroy bacteria. The electric bottle sterilizer contains a bowl in which water and teats are inserted. The process is very simple and convenient for parents, and sterilization takes place in just a few minutes. The teats thus sterilized last up to 3-6 hours, but there are longer-lasting appliances or appliances that sterilize the bottles automatically when stored in the device, providing a sterile environment for up to 24 hours. The main advantage is ease of use, but also short sterilization time, long shelf life and high capacity. They also have a lot of useful accessories such as special trays to place the teats or an alarm at the end of the program. The disadvantages of these sterilizers are their high price and low portability. The microwave bottle sterilizer is inserted into the microwave to sterilize the objects inside. It also uses steam sterilization and keeps the bottles sterile for up to 3 hours. The advantages are their low price, simplicity, ease of use and the fact that they are easy to transport and hence useful for trips. The disadvantages of these sterilizers are the reduced capacity, the necessity of a microwave oven and the risk of burning (the teats are very hot when they are removed from the appliance) [5].

In this paper we aimed at analyzing the thermal stability of different types of teats, in order to determine at what temperature they begin to decompose and at what temperature the degradation products may become harmful to the health of

the baby. Thermogravimetric (TG) and derivative thermogravimetric (DTG) analysis of various types of teats used for infant feeding in this paper provides information on their thermal stability in both air and nitrogen, as some of the sterilization methods involve heating them. Differential calorimetry enabled us to obtain information on the composition of the materials which the tested teats were made of.

2. Experimental

Materials

The materials subjected to thermogravimetric analysis are 3 types of baby teats of different thicknesses, colors and materials, marked: B1, B2 and B3. The teat marked B3 is made of yellow-brown latex. B1 and B2 are teats made of transparent silicone.

Methods

Thermogravimetric (TG) and derivative thermogravimetric (DTG) analyses are the most popular methods applied by researchers to assess the thermal stability of different types of materials. The TG technique measures the variation of the weight of the sample depending on temperature when it is subjected to a temperature increase process at a controlled rate within a certain interval [6]. The graphical representation of sample mass variation with temperature increase is the thermogravimetric curve (TG). The curve obtained by graphical derivation of the TG curve is marked DTG. TG and DTG curves are used to determine the main thermogravimetric characteristics of each degradation stage: T_{onset} - initial temperature at which degradation begins at each stage; T_{peak} - the temperature corresponding to the maximum degradation rate; T_{endset}- final temperature in each stage and W - percentage loss of mass.

Differential scanning calorimetry is a thermal analysis technique that shows how the temperature changes material heat capacity. Also, differential scanning calorimetry (DSC) is a thermoanalytical method in which the difference in the amount of heat required to increase the temperature of a sample and reference is measured as a function of temperature. For this method both samples need to have same temperature. DSC is used to measure specific heat, heat capacity, melting temperature, reaction energy and temperature, heat of fusion, denaturization and oxidation temperature. DSC technique is defined by the measuring of the amount of energy absorbed or released by a sample when it is heated or cooled. The measurement provides qualitative and quantitative data on endothermic (heat absorption) and exothermic (heat evolution) processes. In this case the sample holder temperature increases linearly function of time. The reference sample should have a well-defined heat capacity over the range of the temperatures to be scanned. Results of DSC analyses are represented by DSC

curves, the result of a DSC experiment. These curves are the representation of heat flux versus time or versus temperature. Using the DSC curves, one may determine the following characteristics specific to the tested samples: T_m – melting temperature, T_c – crystallization temperature and T_g – glass transition temperature.

Instruments

The thermal analysis was carried out using a Mettler Toledo TGA-SDTA851^e derivatograph in nitrogen and air atmosphere, at 20ml/min flow rate, 10°C /min (25-700°C) heating rate and samples weight ranging between 4-6 mg. The DSC curves were recorded by a Mettler Toledo DSC1 device in inert atmosphere, at 10°C /min heating rate. We performed scans within the -80 - 200ºC temperature interval, two heating processes and one cooling process, the weight of the tested samples ranging between 4.4 and 5.1 mg.

3. Results and discussions

Thermogravimetric Analysis

The DTG curves recorded in air for the teats marked B1, B2 and B3 are shown in Figure 1, and those recorded in inert atmosphere are shown in Figure 2.

Table 1 includes the main thermogravimetric characteristics of the tested samples: T_{onset}– initial temperature at which degradation begins at each stage; T_{peak} - the temperature corresponding to the maximum degradation rate; T_{endset}– final temperature in each stage and W - percentage loss of mass. It also shows the residue at a temperature of 700°C.

The analysis of the main thermogravimetric characteristics shown in Table 1 reveals that the degradation of the baby teat marked B3 occurs in two stages in both air and nitrogen. The residual amounts obtained in this sample in the two working atmospheres are less than 3%. In the case of the teat marked B2, five stages of degradation in air and two stages in nitrogen are distinguished, and the amount of residue is 56% in air and 50% in nitrogen. The teat marked B1 also has a complex degradation mechanism, consisting of four decomposition stages when the working atmosphere is air, and three stages in nitrogen. In this case, in both working atmospheres, the highest residual amounts were obtained, thus proving a very good thermal resistance.

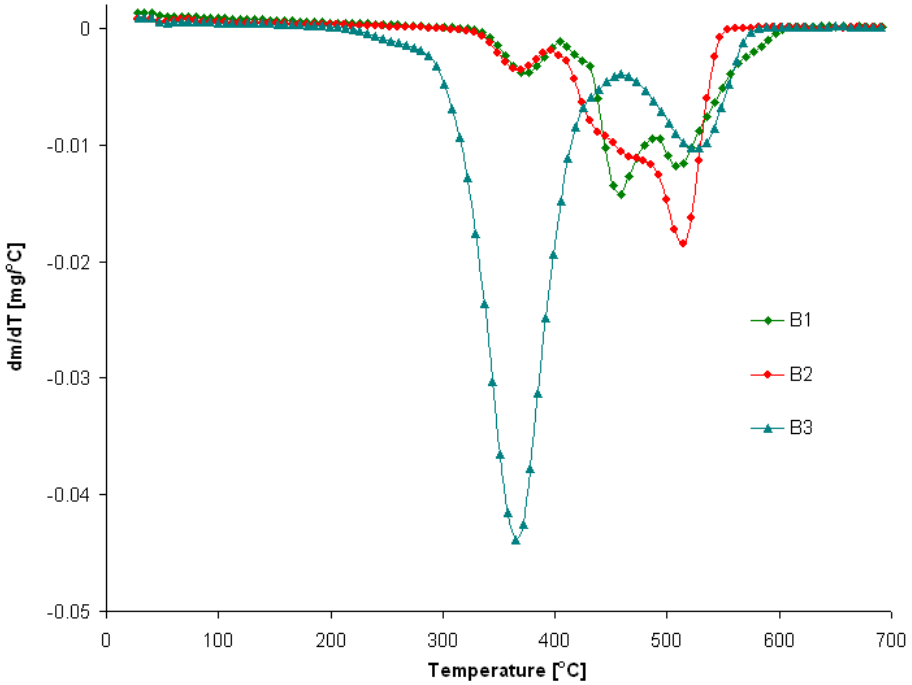

Fig. 1. DTG curves of the three baby teats recorded in air

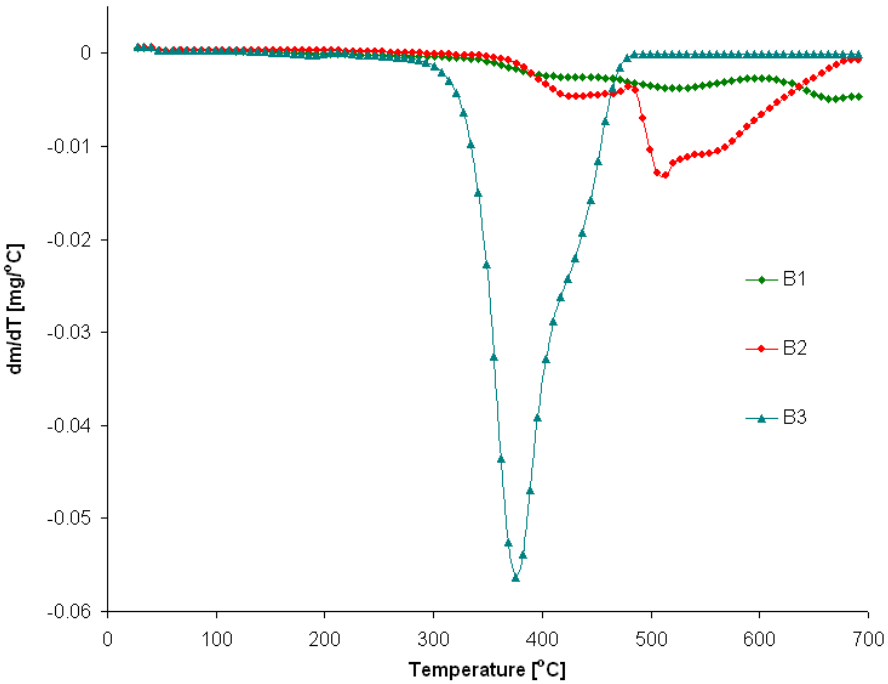

Fig. 2. DTG curves of the three baby teats recorded in nitrogen

Table 1

Thermogravimetric data

Sample	The working atmosphere	Stage of thermal degradation	T_{onset} (°C)	T_{peak} (°C)	T_{endset} (°C)	W (%)	Residue (%)
B1	air	I	354	373	401	4.11	64.08
		II	419	-	446	2.06	
		III	446	458	478	13.34	
		IV	497	509	588	16.41	
B2	air	I	349	367	393	4.78	56.20
		II	409	413	424	1.50	
		III	424	-	452	7.58	
		IV	452	465	493	12.35	
		V	493	514	535	17.59	
B3	air	I	309	366	408	78.01	2.72
		II	493	530	555	19.27	
B1	nitrogen	I	366	413	483	7.08	77.34
		II	483	522	563	7.85	
		III	644	666	-	7.73	
B2	nitrogen	I	387	429	486	1212	50.43
		II	498	506	659	37.45	
B3	nitrogen	I	339	376	394	62.39	2.33
		II	394	428	454	35.28	

When the degradation onset temperature in the first stage is considered to be a thermal stability criterion, the following thermal stability series are obtained:

-in air: **B3** < **B2** < **B1**

-in nitrogen: **B3** < **B1** < **B2**

The thermal resistance, under isothermal conditions, of the three baby teats was tested with a Mettler Toledo derivatograph, in air, by keeping them at constant temperature (120°C) for 20 minutes. There was no mass loss due to heat treatment in any of the samples.

Differential scanning calorimetry

Differential scanning calorimetry studies were performed to determine phase transitions. For the three types of baby teats, DSC curves (two heating and cooling cycles) were recorded in the temperature range -80 - 200°C. Taking into account the fact that the first heating cycle is influenced by the history of the sample, figure 3 comparatively shows the curves corresponding to the three teats for the second heating cycle. For the sample marked B3, Figure 3 also shows a

detail with the variation of the heat flow within the 10 - 70°C range, in order to highlight the existence of the glass transition temperature at 34°C.

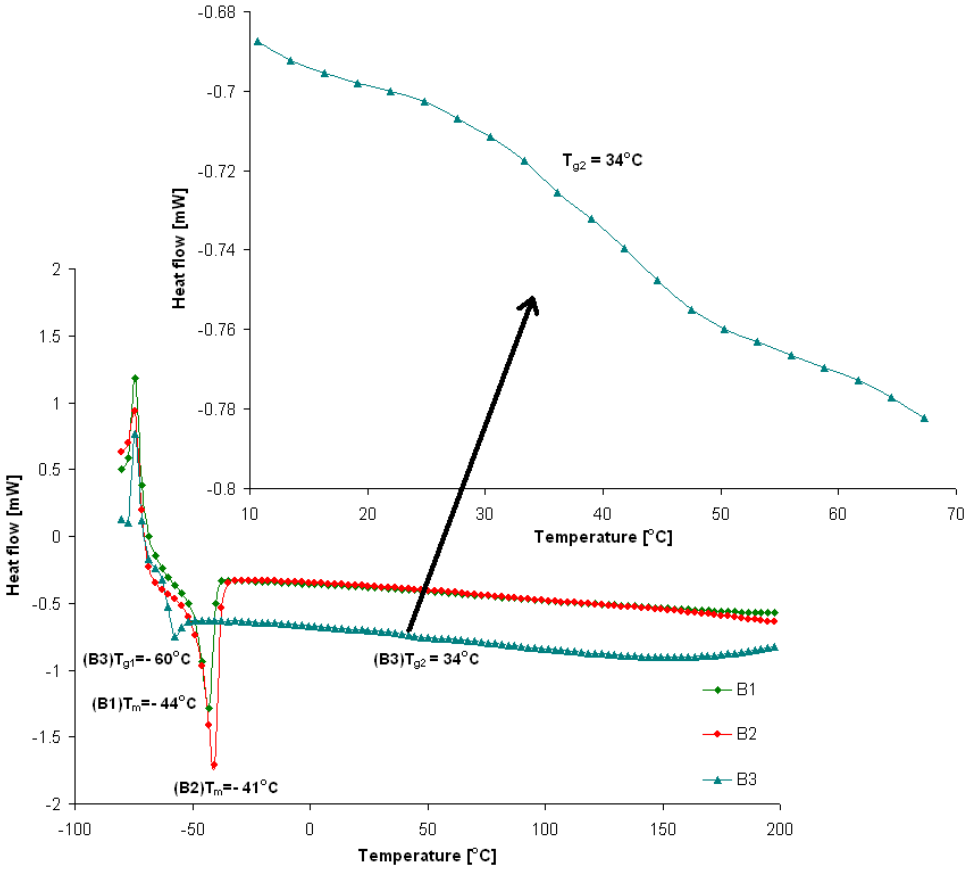

Fig. 3. DSC curves for B1, B2 and B3 for the second heating cycle

By analyzing the melting (T_m) and glass transition (T_g) temperatures, one may gather information about the components found in the structure of the materials which the baby teats are made of. For the teats B1 and B2, made of silicone rubber, according to the DSC curves shown in Figure 3, we identified T_m=-41°C for sample B2 and T_m=-44°C for sample B1. According to literature [7-12], these melting temperature values confirm the presence of polydimethylsiloxane in these samples. For sample B3 made of latex, we see in Figure 3 the existence of two glass transition temperatures T_{g1}=-60°C and T_{g2}=34°C. The analysis of literature [7] indicates the presence in this sample of butadiene-styrene rubber (T_g=-59.61°C) and possibly of 2-tert-butylaminoethyl methacrylate (T_g=33°C).

4. Conclusions

The research enabled us to collect information about the thermal stability of different types of baby teats in both air and inert atmosphere.

The thermal resistance, in isothermal conditions, of the three baby teats was tested using a Mettler Toledo derivatograph, in air, for 20 minutes. No mass losses were recorded in any of the samples, when they were kept at constant temperature (120°C).

Differential scanning calorimetry allowed the gathering of information about the composition of materials which the baby teats are made of.

REFERENCES

[1] Lisa G., Yoshitake Y., Michinobu T., Thermal degradation of some ferrocene-containing poly(aryleneethynylene)s, *Journal of Analytical and Applied Pyrolysis*, 120, (2016), 399–408.

[2] Lund K.H., Petersen J.H., Safety of food contact silicone rubber: Liberation of volatile compounds from soother and teats, *European food research and technology*, 214, (2002), 429-434.

[3] Bouma, K., Nab FM., Schothorst R.C., Migration of N-nitrosamines, N-nitrosatable substances and 2-mercaptobenzthiazol from baby bottle teats and soothers: a Dutch retail survey, *Food Additives and Contaminants*, 20(9), (2003), 853-858.

[4] Conn RE, Kolstad JJ, Borzelleca JF, Dixler DS, Filer LJ, LaDu BN, Pariza MW. Safety assessment of polylactide (PLA) for use as a food-contact polymer, *Food and Chemical Toxicology*, 33(4), (1994), 273-283.

[5] Renfrew M. J., McLoughlin M., McFadden A., Cleaning and sterilisation of infant feeding equipment: a systematic review, *Public Health Nutrition*, 11(11), (2008), 1188–1199.

[6] Mihailă A., Gherghel A., Pătrăuţanu O. A., Amariei M., Lisa G., Thermal Analysis of Human Hair in Non-Isothermal and Isothermal Conditions, *Annals of the Academy of Romanian Scientists Series on Physics and Chemistry Sciences*, 2(2), (2017), 33-42.

[7] De P.P., Choudhury N. R., Dutta N.K., *Thermal Analysis of Rubbers and Rubbery Materials*, Smithers Rapra Technology Ltd., United Kingdom 2010.

[8] Roland C. M., Aronson C. A., Crystallization of polydimethylsiloxane end-linked networks, *Polymer Bulletin*, 45(4-5), (2000), 439–445.

[9] Aranguren M. I., Crystallization of polydimethylsiloxane: effect of silica filler and curing, *Polymer*, 39(20), (1998), 4897-4903.

[10] De Jaeger R., Gleria M., *Inorganic Polymers, Chapter 2. Silicones in Industrial Applications*, Nova Science Publishers, 61-161, 2007.

[11] Choudhury N.R., De P.P., Dutta N.K., *Thermal Analysis of Rubbers and Rubbery Materials,* Smithers Rapra Technology, iSmithers 2010.

[12] Chavan S.N, Mandal D., Combined effect of ether and siloxane substituents on imidazolium ionic liquids, *RSC Advances*, 5(80), (2015), 64821-64831.